DOKUZ EYLÜL UNIVERSITY
GRADUATE SCHOOL OF NATURAL AND APPLIED SCIENCES

DESIGN AND CONTROL OF A VALVELESS MICROPUMP

by

Serkan DOĞANAY

August, 2020
İZMİR

DESIGN AND CONTROL OF A VALVELESS MICROPUMP

A Thesis Submitted to the
Graduate School of Natural and Applied Sciences of Dokuz Eylül University
In Partial Fulfillment of the Requirements for the Degree of Doctor of Philosophy in Mechatronics Engineering, Mechatronics Engineering Program

by
Serkan DOĞANAY

August, 2020
İZMİR

Ph. D. THESIS EXAMINATION RESULT FORM

We have read the thesis entitled "**DESIGN AND CONTROL OF A VALVELESS MICROPUMP**" completed by **SERKAN DOĞANAY** under supervision of **ASSOC. PROF. DR. ALPASLAN TURGUT** and we certify that in our opinion it is fully adequate, in scope and in quality, as a thesis for the degree of Doctor of Philosophy.

………………………………………….

Assoc. Prof. Dr. Alpaslan TURGUT

Supervisor

………………………………….

Assoc. Prof. Dr. Levent ÇETİN

Thesis Committee Member

…………………………………….

Assoc. Prof. Dr. Mehmet Akif EZAN

Thesis Committee Member

……………………………………

Assoc. Prof. Dr. Barbaros ÇETİN

Examining Committee Member

……………………………………

Assoc. Prof. Dr. Mehmet SARIKANAT

Examining Committee Member

Prof. Dr. Özgür ÖZÇELİK

Director

Graduate School of Natural and Applied Sciences

ACKNOWLEDGEMENTS

First and foremost, I would like to express my deepest appreciation to my supervisor Assoc. Prof. Dr. Alpaslan Turgut for his unconditional support, invaluable guidance and vigorous encouragement. His confidence in my abilities, and the freedom he gave me during my Ph.D. have formed me into the researcher I am today. I also have to thank him for the tremendous opportunities he provided me to expand my research network.

My sincere gratitude also goes for my doctoral thesis committee member Assoc. Prof. Dr. Levent Çetin for his endless support, perpetual contribution and stimulating discussions both during and beyond doctoral thesis committee meetings. His excellent guidance helped me considerably, especially for magnetic actuator design and magnetic nanofluid flow control.

I would like to express my deepest gratitude to my doctoral thesis committee member Assoc. Prof. Dr. Mehmet Akif Ezan for his precious contribution and fruitful discussions both during and beyond doctoral thesis committee meetings, especially for numerical and experimental magnetic nanofluid flow.

I would also like to express my gratitude and appreciation to examining committee members of Assoc. Prof. Dr. Barbaros Çetin and Assoc. Prof. Dr. Mehmet Sarıkanat for their contributions and inspiring discussions during the thesis defence.

This adventure would not have been possible without the continuous support of my friends and colleagues. My appreciation first goes to İsmet Ateş for his technical support and discussions in most stages of this thesis. I want to thank Rahime Alsanğur and Abdulkareem Alasli, who helped me during the determination of the magnetic nanofluid properties. I also want to deliver my thanks to Alim Zorluol for his technical support during the prototyping. Lastly, I am so thankful to Halil Doğacan Koca, Tuba Evgin, and Alper Mete Genç for their valuable mental support.

I would like to acknowledge the financial support provided by the Scientific and Technological Research Council of Turkey (TÜBİTAK) during my Ph.D. in the scope of TÜBİTAK BİDEB 2211-A program. Also, I am also thankful for the financial support for this thesis by the Research Foundation of Dokuz Eylül University (Project no: 2017.KB.FEN.022).

I also would like to acknowledge Cost Action Nanouptake CA15119 for the financial support in the scope of Short Term Scientific Mission (STSM) and Inclusiveness Target Countries (ITC) conference grant programs.

Last but not least, this thesis would not have been completed without support and encouragement of my family members. I must express my best gratitude to my wife Esra Özcan Doğanay, for her perpetual support, understanding and patience. I also have to express my profound gratitude to my mother Ayşe Doğanay, my father Gencay Doğanay, my brother Erkan Doğanay, and my nephew Ayaz Doğanay for their endless support.

Serkan DOĞANAY

DESIGN AND CONTROL OF A VALVELESS MICROPUMP

ABSTRACT

The advancement in recent miniaturized devices and systems has caused a rapid growth of the microscale fluidic systems in different fields. In such designs, one of the substantial problems is the requirement for a tiny amount of fluid transportation in microscale channels.

In this thesis, a valveless micropump working with magnetic nanofluid is designed and controlled. The design can be a potential solution for fluid transportation in both biomedical and electronics cooling devices. For this purpose, the properties of magnetic nanofluid, i.e., viscosity, magnetization capability, and thermal conductivity are investigated. A permanent magnetic actuator (PMA) is designed to ensure a valveless actuation for the micropump. Then, a microchannel unit is designed and manufactured. By integrating the PMA with the microchannel unit, a valveless micropump system is built. Following, the magnetic nanofluid flow inside the valveless micropump is investigated both numerically and experimentally while the PMA is stationary. To test the performance of the valveless micropump, the flow is also investigated by varying PMA speed. The results of performance tests indicated that the fluid velocity increases up to a specific PMA speed, then it becomes to decrease.

Finally, closed-loop control is implemented to control the fluid flow. A real-time image processing strategy is developed to determine the real-time magnetic nanofluid velocity. Then, a proportional-integral-derivative (PID) controller is implemented. The results revealed that it is possible to control magnetic nanofluid flow by the PID controller for a given reference velocity.

Keywords: Valveless micropump, permanent magnetic actuator, magnetic nanofluid, microchannel, real-time image processing, real-time velocity measurement, closed-loop control, PID control

VALFSİZ MİKROPOMPA TASARIMI VE KONTROLÜ

ÖZ

Mini boyutlu cihaz ve sistemlerdeki gelişmeler ile birlikte, çeşitli alanlarda kullanılabilecek mikro ölçekli akışkan sistemlerin gelişimi hızlanmıştır. Bu sistemlerdeki, en temel sorunlardan biri, düşük miktardaki sıvıların mikrokanallar içerisinde taşınmasıdır.

Bu tez kapsamında, manyetik nanoakışkan ile çalışan valfsiz bir mikropompa tasarlanmış ve kontrol edilmiştir. Tasarım, biyomedikal ve elektronik soğutma cihazlarında sıvı taşınması problemine çözüm olabilme potansiyeline sahiptir. Bu amaçla, manyetik nanoakışanın viskozite, mıknatıslanma kabiliyeti ve ısıl iletkenlik gibi özellikleri de incelenmiştir. Mikropompanın, valfsiz çalışabilmesi için bir kalıcı mıknatıslı eyleyici (KME) tasarlanmıştır. Daha sonra bir mikrokanal ünitesi tasarlanmış ve üretilmiştir. KME ile mikrokanal ünitesi entegre edilerek, valfsiz mikropompa sistemi oluşturulmuştur. Daha sonra, mıknatısların sabit pozisyonda olması durumunda, valsiz mikropompa içerisindeki manyetik nanoakışkan akışı sayısal ve deneysel olarak incelenmiştir. Valfsiz mikropompa performansının belirlenmesi için akış, farklı KME hızlarında sistem test edilmiştir. Performans testi sonuçları, manyetik nanoakışkan hızının, artan KME hızı ile birlikte belirli bir noktaya kadar arttığını, fakat bu noktanın ötesinde azalmaya başladığını ortaya koymuştur.

Son olarak, akış kontrolü için, kapalı döngü kontrol uygulanmıştır. Anlık manyetik nanoakışkan hızının belirlenmesi için, gerçek zamanlı bir görüntü işleme yöntemi geliştirilmiştir. Daha sonra, oransal-integral-türev (PID) kontrolcüsü uygulanmıştır. Sonuçlar, manyetik nanoakışkan akışının, bir referens değeri için, PID kontrolcü ile kontrol edilebileceğini göstermiştir.

Anahtar Kelimeler: Valfsiz mikropompa, kalıcı manyetik eyleyici, manyetik nanoakışkan, mikrokanal, gerçek zamanlı görüntü işleme, gerçek zamanlı hız ölçümü, kapalı döngü kontrol, PID kontrol

CONTENTS

LIST OF FIGURES

LIST OF TABLES

Page

CHAPTER ONE
INTRODUCTION

1.1 Motivation

The overwhelming demand on miniaturized devices and systems has ended up with the rapid growth of microscale engineering. The development and implementation of sub-millimeter engineering techniques have enabled the advancement of micro-electro-mechanical systems (MEMS). Among the various MEMS, microfluidics has appeared as a critical research area with the capability of providing fluid manipulation in micro-sized channels (Whitesides, 2006). The main problems with microfluidics are *(i) pumping the fluid in tiny quantities*, and *(ii) controlling the amount of the transported fluid*.

The initial motivation of this thesis is to bring a novel proposal to resolve the microscale pumping problem for microfluidics. For this purpose, a valveless micropump has been designed and implemented. Fe_3O_4-water magnetic nanofluid has been employed in the microchannel unit as the working fluid. The driving force for the pumping has been generated by a magnetic actuator.

The valve is the main part of a regular micropump system. In most cases, the valve is in contact with the micro-sized channel(s) or tube and pumped fluid. This means that the valve type or design directly influences the dimensions of the pumping region. The motivation behind the *"valveless"* term is removing the valve from the pumping region, and making the microchannel unit dimensions and design independent from the valve.

Magnetic nanofluids are multi-functional and smart materials. They can be manipulated as desired in the presence of a magnetic field. The motivation for employing a magnetic nanofluid and a magnetic actuator in this thesis can be divided into three main topics:

- A magnetic actuator can provide a contactless power to a magnetic nanofluid instead of using a valve.

- Manipulation capability of the magnetic nanofluids with a known form of an external magnetic field by a magnetic actuator. So, they can be used like a piston in order to drive a secondary fluid in many different medical and biological applications (Vekas, Bica, & Avdeev, 2007).

- Tunable thermophysical properties such as thermal conductivity and viscosity under the influence of the external magnetic field on them (Shima, Philip, & Raj, 2009). This makes it possible to use them for thermal management systems for electronics.

1.2 Thesis Structure

Figure 1.1 schematically summarizes the structure of the following chapters. The first chapter indicates a literature survey for the related studies within the scope of this thesis such as properties of magnetic nanofluids and available micropumping applications. Following, the objectives and contributions of this thesis are provided by addressing the research gaps obtained from the literature survey.

In the second chapter, the properties of Fe_3O_4 magnetic nanofluid, i.e., viscosity, magnetic properties and thermal conductivity are presented. Then, both the design and structure of the valveless micropump are provided in the third chapter. In the fourth chapter, magnetic nanofluid flow inside the valveless micropump is investigated both numerically and experimentally. According to the observations from this chapter, closed-loop control of the magnetic nanofluid inside valveless micropump is carried out in the fifth chapter. The thesis is finalized by concluding remarks and future recommendations within the sixth chapter.

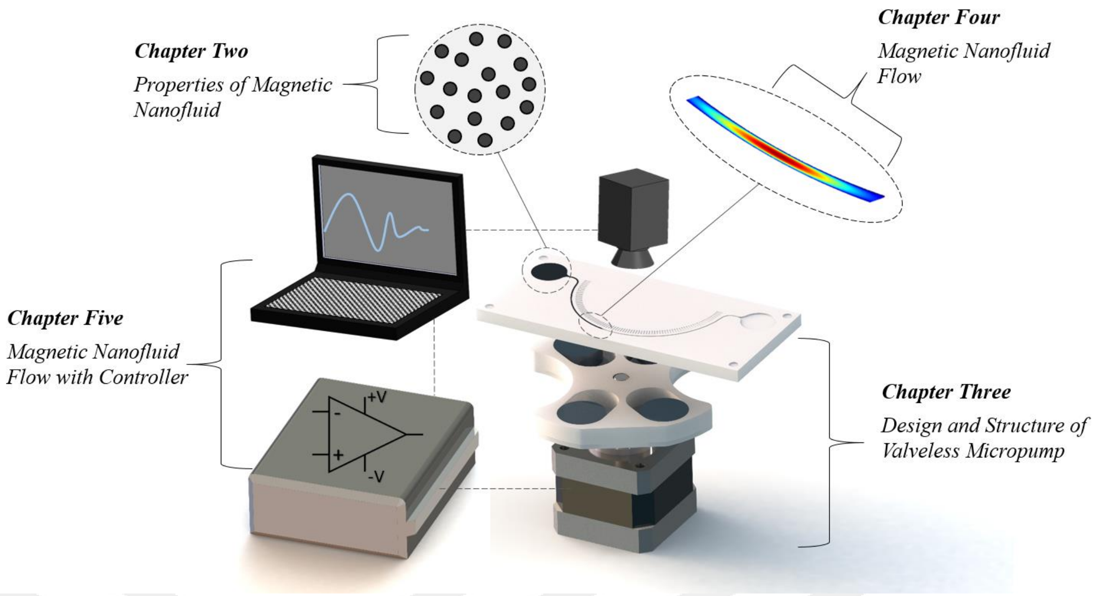

Figure 1.1 Schematic presentation of the thesis structure

1.3 Literature Survey

The literature survey is divided into two sections. In the first one, the properties of magnetic nanofluids such as viscosity, magnetic properties, and thermal conductivity are presented. In the second section, magnetic nanofluid based micropumping applications are presented.

1.3.1 Properties of Magnetic Nanofluids

1.3.1.1 Viscosity of Magnetic Nanofluids

The viscosity directly influences the fluid flow, it is an essential parameter, which needs to be considered before using magnetic nanofluids in the related application. Due to the higher density of the particles, the addition of the nano-sized metallic particles is expected to cause an increment in viscosity. Although this is a handicap for pumping power in micropumps, the possibility of the manipulation of magnetic nanofluids under the influence of the external magnetic field makes them attractive with the reasonable viscosity increments. Therefore, researchers are focusing on the viscosity of the different type of magnetic nanofluids.

One of the first attempts to measure the viscosity of the magnetic nanofluids was carried out by Dababneh, Ayoub, Odeh & Laham (1993). They used Fe_3O_4 nanoparticles dispersed in petroleum distillate. The results indicated that the viscosity of the magnetic nanofluid increases linearly with increasing particle concentration. Following, Bacri, Perzynski, Shliomis & Burde (1995) employed a magnetic nanofluid with $CoFe_2O_4$ particles dispersed in water at 20 vol. % concentration. They also applied an external magnetic field to investigate magnetic field dependent viscosity. The results indicated that viscosity increases in the presence of an external magnetic field in the range of 0–2500 Oe. Moreover, the maximum viscosity ratio which is the ratio between viscosity values in the presence and absence of the external magnetic field was obtained as 1.75 at 850 Oe.

Zeuner, Richter & Rehberg (1998) investigated the viscosity behavior of Fe_3O_4-water magnetic fluid flowing through a capillary pipe. Then, the viscosity of the magnetic nanofluid was determined by measuring the pressure differences over the capillary tubes. They also applied an alternating magnetic field generated by a solenoid. The magnetic field was applied at different strengths and different driving frequencies. The maximum viscosity ratio was achieved as 1.25 at 35 kA/m 1002 Hz.

Thurm & Odenbach (2002) carried out viscosity measurements with a commercial Fe_3O_4-synthetic ester magnetic nanofluid (APG513A) under the external magnetic field. The sample was exposed to magnetic field strength in the range of 0 to 35 kA/m. The measurements were held for different shear rates and the results revealed that the maximum increment in viscosity at 1.8, 4.2 and 6.8 s^{-1} shear rates are 1.98, 1.02 and 0.68%. They reported that the chain formation in suspensions is true and they can be destroyed by high shear rates. In the following research, Thurm & Odenbach (2003) investigated the viscosity of the synthetic ester-based Fe_3O_4 magnetic nanofluids under the influence of the external magnetic field. The magnetic field was generated with an electromagnet in the range of 0-25 kA/m. The viscosity of the samples with different volumetric concentrations between 6.63-7.35% was measured by a specially designed ferrofluid rheometer. The results showed that the viscosity ratio increases to almost 17, as the magnetic field strength increases.

Li, Xuan & Wang (2005) investigated the effect of the external magnetic field, on the viscosity of Fe-water and Fe_3O_4-water nanofluids. They prepared Fe_3O_4-water magnetic nanofluid sample with volumetric concentration of 2.8% and Fe-water samples with different volumetric concentrations of 1 to 5%. Viscosity was measured by using a capillary tube viscometer under the magnetic field generated by permanent magnets in both parallel (0-900 G) and perpendicular (0-140 G) directions to the flow for Fe-water magnetic nanofluid, perpendicular (0-240 G) to the flow for Fe_3O_4-water nanofluid. The results indicated that the viscosity of both magnetic nanofluids increases in the presence of the external magnetic field. The maximum viscosity ratio was observed as almost 26 and 1.55 for Fe-water magnetic nanofluid for perpendicular and parallel directions, respectively. Moreover, the maximum viscosity ratio of Fe_3O_4-water was found at almost 25.8. The same group (Li, Xuan, & Wang, 2006) have utilized a similar type of samples in order to investigate magnetic field dependent viscosity. The measurements were carried out at constant 20°C with a capillary tube viscometer. The magnetic field was applied parallel to the flow for Fe–water magnetic fluid in the range of 0 to 0.09 T and perpendicular to the flow for both fluids in the range of 0 to 0.025 T. The results indicated that the maximum viscosity ratio is 25 for 2.8 vol. % concentrated Fe_3O_4-water sample at 0.02 T and 26 for the 4 vol. % concentrated Fe-water magnetic nanofluid sample at 0.014 T. They realized that the viscosity increases with an increase in magnetic field strength and reaches a constant value because of the saturation of the samples' magnetization.

Andhariya, Chudasama, Patel, Upadhyay & Mehta (2008) focused on the effect of capillary size and magnetic field strength on the viscosity of Fe_3O_4-water and Fe_3O_4-kerosene magnetic nanofluids. They measured the viscosity of samples with 0.64 vol. % concentration using capillary tube viscometer under 0-0.6 T magnetic field. The maximum viscosity ratio of the Fe_3O_4-water and Fe_3O_4-kerosene samples were 1.71 and 1.74 at 0.6 T for 0.5 mm capillary diameter, respectively.

Ghasemi, Mirhabibi & Edrissi (2008) dispersed Fe_3O_4 magnetic nanoparticles into kerosene at 7 vol. % concentration and measured the viscosity of magnetic nanofluid under the effect of the magnetic field. They measured the viscosity by using a Physica

MCR 300 rheometer in the magnetic field strength range of 0-145 kA/m for different shear rates. The maximum viscosity ratio observed was 5.68 for 5.7 s^{-1} and the viscosity decreases with the increasing shear rate. In another study of a similar group Ghasemi, Mirhabibi, Edrissi, Aghababazadeh & Brydson (2009), Fe_2O_3 and Fe_3O_4 magnetic nanoparticles were dispersed in kerosene. They measured the viscosity of the sample with 7.2 vol. % concentration under external magnetic field in the range of 0 to 45 kA/m with a Physica MCR300 rheometer. They reported the maximum viscosity ratio was 5.6 for 5.7 s^{-1} shear rate at 43 kA/m and the increasing shear rate caused a decrement in viscosity ratio.

Hezaveh, Faziali & Noshadi (2012) studied on the viscosity of the Fe_2O_3-paraffin magnetic nanofluid. They prepared samples with different weight concentrations from 5 to 30%. The measurements were carried out with the Physica MCR301 rheometer under the influence of the magnetic field in the range of 0 to 0.5 kA/m. The results indicated that viscosity increases with increasing particle concentration and the viscosity ratio increases up to 13.

Hosseini, Ghasemi, Faziali & Henneke (2012) dispersed Co_3O_4 nanoparticles in paraffin and measured the viscosity of magnetic nanofluid samples with 15, 20, 25, 30 and 40 wt. % concentration. Measurements were carried out using Physica MCR300 rheometer under the applied magnetic field in the range of 0 to 90 kA/m at ambient temperature. Viscosity does not show an obvious increase for 15, 20, 25 and 30 wt. %, it increases from 3.4 Pa.s to 5.4 Pa.s for the sample with 40 wt. %. The maximum viscosity ratio was calculated as 1.58 at 90 kA/m. They pointed out that the aggregation and concentration of nanoparticles affect the viscosity of the fluid.

Khosroshahi & Ghazanfari (2012) used Fe_3O_4-water magnetic nanofluids at 7 vol. % concentration as their samples and investigated the rheological behaviour of the PVA-coated and uncoated fluids under the magnetic field. A Physica MCR300 rheometer employed for viscosity measurements under two different shear rates and the magnetic field was applied in the range of 0 to 0.5 T to the sample. The viscosity ratios of the PVA-coated sample under 20s^{-1} and 150s^{-1} were calculated as 8.66 and

3.57, respectively. The viscosity ratios of the uncoated sample under $20s^{-1}$ and $150s^{-1}$ were calculated as 10.8 and 3.4, respectively. These results revealed that the viscosity increases with the increasing magnetic field, but decreases with increasing shear rate.

Shah, Upadhyay & Aswal (2012) studied the effect of the magnetic field on viscosity with transformer oil-based Fe_3O_4 nanofluids with different particle sizes. They prepared three nanofluid samples using 10 nm particles, 30 nm particles, and the mixture of these two particles. The measurements were carried out by the Physica MCR301 rheometer with a Physica MDT180/1T magneto-rheological cell in order to generate a magnetic field. The magnetic field strength was applied up to 174.3 kA/m in the perpendicular direction to shear flow. The results showed that the maximum viscosity ratio reaches 8 with the application of the external magnetic field.

Wang, Yang & Bian (2012) investigated the effect of the external magnetic field on the viscosity of Fe_3O_4-silicon oil magnetic nanofluids. The experiments were held by Theta DV-III rotating viscometer under the magnetic field strength up to 1400 G generated by permanent magnets. The results showed that the maximum viscosity ratio reaches about 166.

Gu et al. (2013) measured the viscosity of water-based Fe_3O_4 magnetic nanofluid under the external magnetic field generated by an electromagnet in the range of 0 to 400 G. They prepared different samples with vol. concentrations of 0.5 to 2.5%. They also investigated the effect of temperature and surfactant. The measurements were carried out using an Ubbelohde viscometer. The results depicted that the maximum viscosity ratio is 1.6 under the influence of the magnetic field. They concluded that increasing temperature and surfactant concentration reduces the influence of the magnetic field on the viscosity.

Yang, Bian, Guo, Zhang & Liu (2014) investigated the viscosity of Fe_3O_4-water magnetic nanofluid with various volumetric concentrations of 2 to 8% were investigated. The measurements were made by a torsional oscillation cup viscometer under the external magnetic field in the range of 0-920 G, which was generated by permanent magnets. The results showed that the maximum viscosity ratio under the external magnetic field reaches up to 32.

Katiyar, Dhar, Das & Nandi (2015) studied the viscosity of Fe_3O_4-polyethylene glycol magnetic nanofluid under the influence of the magnetic field generated by an electromagnetic coil. Samples with different weight concentrations between 5-15% were measured with the Physica MCR301 rheometer. The magnetic field strength was altered between 0-1.2 T. They reported that the maximum viscosity ratio increases to 32.3 in the presence of the magnetic field.

Sundar, Ramana, Singh & Sousa (2015) measured the magnetic field dependent viscosity of Fe_3O_4-vacuum pump oil magnetic nanofluid. They prepared the samples with different volumetric concentrations of 0.05 to 1%. Measurements were carried out by vibro-viscometer (SV-10) and the magnetic field was produced by permanent magnets in the range of 0-2100 G. They observed that viscosity ratio increases to 2.1.

Malekzadeh, Pouranfard, Hatami, Banari & Rahimi (2016) studied the magnetic field dependent viscosity of water-based Fe_3O_4 magnetic nanofluids with different volumetric concentrations of 0.1 to 1%. They also focused on the influence of the temperature on the magnetic field dependent viscosity. The measurements were held by using a Brookfield rotational viscometer (LVDV-II+PRO) under 0-550 G external magnetic field strength. The results showed that the maximum viscosity ratio is almost 3 and this ratio decreases by the increasing temperature. Moreover, they concluded that the magnetic field has no significant effect on the temperature-dependent viscosity decrement rate.

Nurdin, Yaacob & Johan (2016) examined the effect of the external magnetic field on the viscosity of γ-Fe_2O_3-water magnetic nanofluid. The samples were prepared in the vol. concentration range of 0.1 to 0.6%. A capillary viscometer was used for viscosity measurements and the magnetic field was generated by using Helmholtz coils. The magnetic field strength was altered between 50-300 G for both parallel and perpendicular directions to the flow. The experimental results indicated that the maximum viscosity ratio is about 1.3 and 1.24 for parallel and perpendicular directions, respectively.

Paul, Das & Manna (2016) measured the viscosity of the Fe_3O_4-water magnetic nanofluids under the effect of the external magnetic field. They prepared various samples with volumetric concentrations of 1.135-4.54%. The measurements were held by using Physica MCR 301 rheometer under 0-0.5 T magnetic field strength. They observed that the maximum viscosity ratio value is about 11.5.

Vshivkov, Rusinova & Galyas (2016) measured the magnetic field dependent viscosity of glycerol-water solution based $Fe_{2.8}O_4$ magnetic nanofluids with different concentrations from 0 to 5 wt. %. The measurements were made by Rheotest RN 4.1 rheometer. The magnetic field was generated in the parallel and perpendicular directions to the rotation axis with a strength of 280 kA/m and 290 kA/m. The results indicated that the maximum viscosity ratio increases to 20 for parallel direction, where it is 70 for the perpendicular direction.

Wang, Wang, Yan, Wang & Feng (2016) investigated the effect of the magnetic field on the viscosity of water-based Fe_3O_4 magnetic nanofluids. They measured viscosity using a vibro-viscometer (SV-10) with the external magnetic field generated by permanent magnets between 0-30 mT. The nanofluid samples were prepared at different vol. concentrations of 0.5 to 5%. The results indicated that the maximum viscosity ratio is calculated as almost 1.4. A similar type of magnetic nanofluid was also used by Wu, Pei, Xuan, Yan & Gong (2016) for the investigation of the magnetic field dependent viscosity. Physica MCR 301 rheometer was employed for the viscosity measurements. The magnetic field strength was altered between 0-160 mT by the special magnetic module of the rheometer. According to the measurement results, the maximum viscosity ratio observed as 5.

Amani et al. (2017) dispersed $MnFe_2O_4$ particles into the water with different volumetric concentrations of 0.25 to 3% and measured the magnetic field dependent viscosity with Brookfield viscometer (DV-I PRIME). The external magnetic field was produced by an electromagnet between 0-400 G. The results revealed that the maximum viscosity ratio is 1.45.

Li, Yao & Li (2017) investigated the rheological properties of perfluoropolyether (PFPE) based Fe_3O_4 magnetic nanofluid with 7.2 vol. % concentration. They measured the viscosity under the applied magnetic field in the range of 0 to 500 kA/m at (-7)-50°C temperature range. They carried out their measurements with a Physica MCR302 rheometer and applied the magnetic field with a Magneto-Rheological Device (MRD) cell. The measurements under various shear rates showed that the maximum viscosity ratio is approximately 3.7 at 500 kA/m, 50°C and 20 s-1 shear rate. The results depicted that the viscosity increases with the increasing magnetic field and reaches a constant value, where it decreases by temperature increment.

Vinod & Philip (2017) investigated the external magnetic field effect on the Fe_3O_4-kerosene magnetic nanofluid with two different volumetric fractions of 0.037 and 0.067. The magnetic field was generated by Helmholtz coils between 0-250 G. The viscosity measurements were carried out by Physica MCR 301 rheometer. The results depicted that the maximum viscosity ratio increases to 1.45.

Basheed, Jain, Pathak & Pant (2018) studied the effect of dipolar interactions on rheological properties of kerosene-based Fe_3O_4 magnetic nanofluid. They prepared samples with volumetric concentrations of 3, 3.5, 4, 4.5 and 5% and measured their viscosity with a Physica MCR301 rheometer under the magnetic field influence between 0-1.2 T. The viscosity ratio was calculated approximately as 4.25 at 1.1 T for 4.5 vol. % sample at 50 s^{-1} shear rate. They pointed out that the chain-like aggregation forms as a result of the induction of a dipolar moment which causes a viscosity increment with the application of the external magnetic field.

Dong, Piao & Choi (2018) dispersed the Fe_3O_4 particles into the mineral oil at 10% volumetric concentration and measured the viscosity under the influence of the external magnetic field. They utilized Physica MCR 300 rheometer for the viscosity measurements under the 0-171 kA/m magnetic field strength. The measurement findings showed that the viscosity ratio increases up to 9 in the presence of the external magnetic field.

Paulovičová et al. (2018) focused on the rheological properties of transformer oil-based Fe_3O_4 magnetic nanofluids under the influence of the external magnetic field produced by an electromagnet. The viscosity of the sample with a 3% weight concentration was measured by using Physica MCR 502 rheometer. Also, the magnetic field strength was altered between 0-1000 mT. According to the measurement results, they found that the maximum viscosity ratio is 1.3.

Priyananda, Sabouri, Jain & Hawkett (2018) measured the viscosity of hydrophobic ionic liquid-based γ-Fe_2O_3 magnetic nanofluids under the influence of the external magnetic field generated by permanent magnets. The samples were prepared with a weight fraction of 20-40%. The viscosity measurements were conducted using the Kinexus Pro rheometer. The external magnetic field strength was varied between 0-3500 G. The results indicated that the maximum viscosity ratio is 5.

Vinod & Philip (2018) studied the magnetic field dependent viscosity of the kerosene-based Fe_3O_4 magnetic nanofluid with 0.037 vol. fraction with three different particle sizes of 8.3, 9.6 and 10.5 nm. The viscosity measurements were held by using a Physica MCR 301 rheometer and the magnetic field was generated by a solenoid in the range of 0-200 G. They observed that maximum viscosity ratio reaches 9 in the presence of the magnetic field for the sample with 10.5 nm.

Wang et al. (2018) measured the viscosity of 0.17 vol. % concentrated Fe_3O_4-pump oil and Fe_3O_4–silicon oil magnetic nanofluids under applied magnetic field. The measurements were held using Theta DV-III rotating viscometer. The magnetic field is applied as 500 G parallel to the temperature gradient. The results presented that for pump oil-based magnetic nanofluid, the viscosity ratio is 1.56; for silicon oil-based magnetic fluid, the viscosity ratio is 1.81.

Wang, Zuo, Zhao, Hou & Li (2019) mixed Fe_3O_4 magnetic nanoparticles with a lubricant (S-220) and measured the viscosity by using a digital rotary viscometer (NDJ-5S) under the external magnetic field applied produced by a solenoid with a ranging strength from 0 to 30 mT. The results of the measurements showed that viscosity decreases as the temperature increases. The maximum viscosity was measured as 1.58 Pa.s under 25 mT applied magnetic field.

Table 1.1 Comparison of key studies on viscosity of magnetic nanofluids

Authors	**Particle**	**Base type**	**φ (vol.)**	**Viscosity (mPa·s)**	**MF Source**	**Increment under MF**
Ghasemi et al. (2008)	Fe_3O_4	Kerosene	7%	~1.4	N/A	~650%
Gu et al. (2013)	Fe_3O_4	Water	1%	~4.2	Electromagnet	~33%
Yang et al. (2014)	Fe_3O_4	Water	4%	~0.92	Permanent magnet	~410%
Malekzadeh et al. (2014)	Fe_3O_4	Water	1%	~0.9	N/A	~12%
Yang et al. (2014)	Fe_3O_4	Synthetic oil	6%	~2.5	Permanent magnet	~20%
Wang et al. (2016)	Fe_3O_4	Water	1%	~1	Permanent magnet	~40%
Wang et al. (2016)	Fe_3O_4	Water	5%	~1.3	Permanent magnet	~46%
Wang et al. (2018)	Fe_3O_4	Silicon oil	0.17%	~64	N/A	~134%

Table 1.1 summarizes the key studies on the viscosity of magnetic nanofluids. It is observed that there are three main contradictions:

- Similar concentrations, but different viscosity values.

- Similar concentrations, similar magnetic field strength, but different viscosity increments in the presence of the magnetic field.

- Lower magnetic particle content, but higher viscosity increment in the presence of the magnetic field.

These contradictions expose that it is necessary to determine the viscosity of the magnetic nanofluid sample, before using it in a micropumping system.

1.3.1.2 Magnetic Properties of Magnetic Nanofluids

It is important to investigate the magnetic properties of magnetic nanofluid in order to observe their behavior under the influence of the external magnetic field. One of the most significant magnetic properties is the magnetization of magnetic materials. After the determination of the magnetization of a magnetic nanofluid, other properties, such as susceptibility and permeability can also be evaluated. The magnetization of a magnetic nanofluid may be influenced by different parameters, i.e., particle concentration, particle size, surfactant (Resiga & Vekas, 2018).

Yu, Zheng & Yang (2000) dispersed Fe_3O_4 nanoparticles into both water and oil. The particle concentration was altered between 3-12 wt. %. They used vibrating sample magnetometer (VSM) to measure the magnetization. The results showed that all samples depict superparamagnetic behavior. Also, the maximum saturation magnetizations were observed as 9.5 and 10.3 emu/g for water and oil-based samples, respectively.

Raşa, Bica, Philipse & Vekas (2002) measured the magnetization of the samples using both VSM and alternating gradient magnetometer (AGM). They dispersed the Fe_3O_4 nanoparticles into transformer oil and pentanol with different vol. concentrations of 0.024-15.1% and 0.02-17.6%, respectively. Their results pointed out that the saturation magnetization increases as the volume concentration increases up to 53 kA/m and 49 kA/m for transformer oil and pentanol, respectively.

Socoliuc, Bica & Vekas (2003) investigated a surfactant influence on the magnetization of magnetic nanofluids. They employed Fe_3O_4 nanoparticles inside the transformer as a base fluid with two different surfactants of pure oleic acid and technical grade oleic acid. Particle content by vol. was altered between 0.078-15% and 0.086-12.4% for the samples with pure and technical grade oleic acid, respectively.

They observed that the saturation magnetization of the samples increases with increasing particle concentration up to 49 and 39 kA/m for pure and technical grade oleic acid, respectively.

Arulmurugan, Vaidyanathan, Sendhilnathan & Jeyadevan (2005) used $Co_{1-x}Zn_xFe_2O_4$-heptane magnetic nanofluid for VSM measurements. The x value was changed between 0.1-0.5. The highest saturation magnetization value was observed at x=1 as 180 G.

Zhang, Dou, Zhang & Gu (2007) et al. investigated the magnetic properties of Fe_3O_4-hexane magnetic nanofluid by a commercial SQUID PPMS magnetometer. They used different particle sizes between 8-18 nm. The magnetic particle content was adjusted as 0.019 g/mL. The results indicated that magnetization of the magnetic nanofluid increases with particle size. Moreover, maximum and minimum saturation magnetization values were obtained as 62 and 92 emu/g for 8 and 18 nm, respectively.

Lin et al. (2010) investigated the saturation magnetization of the HNO_3 based $MnFe_2O_4$ nanofluids for different vol. concentrations (0.25, 0.75, 1 and 1.25%). The magnetization measurements were held by using a VSM. Their measurements showed that the saturation magnetization of the nanofluid increased as the volume concentration increased up to 0.862 emu/g. Moreover, they indicated that the magnetic nanofluid samples indicate superparamagnetic behavior.

Ho (2011) investigated particle concentration influence on magnetic properties of magnetic nanofluids. The particle concentration was altered between 0.4-4 vol. % concentrations. The measurements were carried out by VSM and the saturation magnetizations of the samples found in the range of 0.6-7.2 kA/m.

Gao et al. (2012) employed γ-Fe_2O_3 magnetic nanoparticles and an ionic liquid to prepare magnetic nanofluid samples within the particle concentration range of 0.4-1.6 vol. %. They used VSM to measure the magnetization capability of the samples. Their findings indicated that the saturation magnetization is highest for the most concentrated sample as 3 kA/m.

Lin et al. (2014) investigated the magnetization behavior of binary magnetic nanofluids. They have first used γ-Fe_2O_3/Ni_2O_3 nanoparticles at a constant concentration of 0.2%. Then, they mixed the primary fluid with ferrihydrite ($Fe_5O_7(OH) \cdot 4H_2O$) within the concentration range of 0-1 vol. % to achieve a binary magnetic nanofluid. Their results depicted that the saturation magnetization is the highest when ferrihydrite concentration is 0.6%.

Desai, Upadhyay & Mehta (2014) studied the chain formation in Fe_3O_4-water magnetic nanofluid by adding halloysite nanotubes and measured the magnetization of the hybrid fluid. They used dodecanoic acid as a surfactant and dissolved the halloysite nanotubes with three different vol. concentrations (0.5, 1 and 2%) in magnetic nanofluid with constant 0.7 vol. % concentration. They measured the magnetization of the samples using VSM at 25^{o}C. The results showed that the samples with 0.5 and 1 vol. % concentrations halloysite has higher saturation magnetization than the Fe_3O_4-water nanofluid itself where the saturation magnetization of with 2% is lower.

Wang, Zhuang, Zhang & Shen (2015) utilized Fe_3O_4 magnetic nanoparticles and dispersed them into polydiethylsiloxane. They have measured the magnetization of the magnetic nanofluid sample by VSM. They reported that their sample has a superparamagnetic behavior with a saturation magnetization value of 1.74 emu/g.

Zhang, Huang, Shao, Li & Zheng (2016) used three different magnetic nanofluid samples. The samples were prepared as Fe_3O_4, γ-Fe_2O_3, and Fe_3O_4/γ-Fe_2O_3 magnetic nanoparticles and silicone oil as the carrier liquid. They ensured that the three samples have the same viscosity value. Then, they carried out magnetic measurements with VSM. The results revealed that the saturation magnetization of the hybrid sample is the highest. Moreover, the saturation magnetization values were obtained for Fe_3O_4,

γ-Fe_2O_3, and Fe_3O_4/γ-Fe_2O_3 based samples as 12.45, 14.25, and 25.08 emu/g, respectively.

Taufiq et al. (2016) measured the magnetization values of olive oil-based Fe_3O_4 magnetic nanofluids samples with different particle mass content and particle sizes. They used oleic acid as a surfactant. The samples were prepared using nanoparticles with 7.3 mm, 8 mm, and 8.4 mm particle diameters. Mass content was 0.32 g, 0.38 g, and 0.41 g for the samples with 8 mm, 7.3 mm, and 8.4 mm particle diameters, respectively. The results showed that the highest saturation magnetization value was belonged to the sample with the highest particle content and size of about 14.81 emu/g.

Wang, Bian, Yang, Zhao & Yu (2017) investigated the magnetic properties of four different magnetic nanofluids. The samples were prepared with CoFeSiB and $CoFe_2O_4$ nanoparticles. The nanoparticles were dispersed in two different carriers of silicone oil and kerosene. The measurements were carried out by VSM at a constant vol. concentration of 4% for all samples. The results showed that the saturation magnetization is higher when the base fluid is silicone oil. Besides, the maximum value of saturation magnetization was observed as 1.79 emu/g for the sample with CoFeSiB alloy.

Abadeh, Fard, Maghrebi & Mohammadi (2019) employed Fe_3O_4-water magnetic nanofluid with 1 wt. % concentration. They measured the magnetic properties by VSM and investigated the influences of different parameters as surfactant material and mass, heater stirring speed and time, pH, initial sonication time, and final sonication by Taguchi analysis. The highest magnetization was found as 81 emu/g, and the parameters were listed according to their importance for magnetization as the surfactant material, surfactant mass, pH, final sonication time, heater stirring time, initial sonication time and heater stirring speed.

Taufiq et al. (2019) utilized VSM in order to measure the magnetization of the Fe_3O_4-water magnetic nanofluid. They observed that their sample demonstrates a superparamagnetic behavior with 3.2 emu/g saturation magnetization.

Ryapolov, Polunin & Shel'deshova (2020) investigated the magnetic properties of Fe_3O_4-water magnetic nanofluid samples with different particle concentrations between 2.7-9.08 vol. % concentrations. They utilized a lab-made setup for the measurements. The results indicated that the magnetization of the samples increases with increasing particle concentration. Also, the highest saturation magnetization value was observed as 43.3 kA/m.

Table 1.2 Comparison of key studies on magnetic properties of magnetic nanofluids

Authors	Particle	Base type	φ (%)	Size	Max. Magnetic Saturation
Yu et al. (2000)	Fe_3O_4	Water	3-12 wt.	8-10 nm	9.5 emu/g
Raşa et al. (2002)	Fe_3O_4	Transformer oil	0.024-15.1 vol.	10 nm	53 kA/m
Socoliuc et al. (2003)	Fe_3O_4	Transformer oil	~0.078-15 vol.	N/A	49 kA/m
Gao et al. (2012)	ϒ-Fe_2O_3	Ionic liquid	0.4-1.6 vol.	~9 nm	3 kA/m
Desai et al. (2014)	Halloysite Nanotube/ Fe_3O_4	Water	HNT/0.5-2 Fe_3O_4 1.4 vol.	8.9 nm	1.75 kA/m
Taufig et al. (2017)	Fe_3O_4	Olive oil	0.32-0.41 g/mL	8.4 nm	14.81 emu/g
Ryapolov et al. (2020)	Fe_3O_4	Kerosene	2.7-9.08 vol.	N/A	43.3 kA/m

Table 1.2 summarizes the key studies on the magnetic properties of magnetic nanofluids. In contrast to viscosity, the results are consistent. Magnetization capability increases with increasing particle concentration. Generally, nano-sized particles result in a superparamagnetic behaviour for magnetic nanofluids.

1.3.1.3 Thermal Conductivity of Magnetic Nanofluids

One of the earliest studies on the thermal conductivity of magnetic nanofluids with magnetite dispersed in kerosene was performed by Kronkalns (1977). He found the magnetic field has no effect on thermal conductivity. Following, Popplewell, Alqenaie, Charles, Moskowitz & Raj (1982) colloidally dispersed the Fe_3O_4 particles in different base fluids of diester, hydrocarbon, water and fluorocarbon. They measured thermal conductivity with the hot-wire method at 38˚C and applied a magnetic field of 1000 G. Their results also indicated that the magnetic field had no noticeable influence on the thermal conductivity.

Li, Xuan & Wang (2005) considered Fe-water magnetic nanofluid with vol. concentrations of 1 to 5%. They used the transient hot-wire method for thermal conductivity measurements. The magnetic field was applied in two different orientations, parallel (0-900 G) and perpendicular (0-240 G) to the temperature gradient. They observed that the parallel magnetic field increased the thermal conductivity up to 25%; however there was almost no change with the perpendicular magnetic field.

Djurek, Znidarsic, Kosal & Djurek (2007) prepared four different magnetic nanofluid samples by dispersing $CoFe_2O_4$ and γ-Fe_2O_3 in water and n-decane. The radial heat flux method was used for thermal conductivity measurements under the influence of a magnetic field up to 2-3x10^2 G at 25˚C. They observed up to 50% decrement in the thermal conductivity with the magnetic field.

Philip, Shima & Raj (2008) measured the thermal conductivity of Fe_3O_4-kerosene magnetic nanofluids with 0-7.8 vol. % concentration by using a thermal property analyzer. The magnetic field was generated with a solenoid like an electromagnet up to 500 G and applied in parallel and perpendicular to the temperature gradient. They observed no enhancement for low concentrations, however, for the higher concentrations, the thermal conductivity enhanced up to 300% and then it decreased. The same group (Shima et al., 2009) again used magnetite-kerosene magnetic nanofluid with different vol. concentrations of 0.11%, 0.4%, 0.57%, 0.82% and 1.71%. The thermal conductivity of the samples was measured by using a transient hot-wire method under the influence of the magnetic field parallel to the temperature gradient. The uniform magnetic field was applied by keeping the sample inside a solenoid. The results showed that the thermal conductivity has increased up to 367%. Similar group Shima & Philip (2011) measured the thermal conductivity of kerosene-based Fe_3O_4 magnetic nanofluids with vol. concentrations of 0.031%, 0.401%, 0.819% and 1.71%

to investigate magnetic field direction influence by using a transient hot wire (KD2 Pro). The magnetic field was applied in both directions of parallel and perpendicular to the temperature gradient. Maximum enhancement was observed with a volumetric concentration of 1.71% about 125% at a magnetic field strength of 378 G with parallel direction. When they changed the magnetic field direction to the perpendicular, there was no significant change in thermal conductivity.

Parekh & Lee (2010) used Fe_3O_4-kerosene magnetic nanofluid in order to investigate the effect of the magnetic field. They prepared samples with five different vol. concentrations of 1.115, 1.7, 2.23, 3.465 and 4.7%. The magnetic field was generated by a solenoid in the range of 0 to 1200 Oe and measurements were made using the Lambda system. The results showed that the maximum thermal conductivity enhancement could be reached 30% at 885 G for 4.7% vol. concentration. They indicated that the zipper-like structure is responsible for the enhancement in thermal conductivity.

Altan, Elkatmis, Yuksel, Aslan & Bucak (2011) dispersed Fe_3O_4 magnetic nanoparticles in both water and heptane with different concentrations. The magnetic field was generated by a DC magnet (max. 2000 G) in perpendicular to the hot-wire equipment. Their results indicated that the thermal conductivity enhanced 5.2% and 2.8% at 2000 G for concentrations below 2 wt. % for the base fluids of water and heptane, respectively.

Gavili, Zabihi, Isfahani & Sabbaghzadeh (2012) conducted time-dependent thermal conductivity measurements with 5 vol. % concentrated Fe_3O_4-water magnetic nanofluid by KD2 Pro. The magnetic field was created by Helmholtz coils while its intensity was controlled by the electric current between 0-1000 G. They observed that the thermal conductivity enhanced up to 200%; however, the enhancement decreased to 20% after 400 s.

Krichler & Odenbach (2013a) used a commercial Fe_3O_4 based magnetic nanofluid (APG513A) sample with a volumetric concentration of 8.56%. They applied the magnetic field through a cylindrical coil in both parallel and perpendicular to temperature gradient at 5, 10, 15, 20, 25, 30, 35, and 40 kA/m. The measurements were conducted using a hot plate technique. The results revealed that the enhancement of the thermal conductivity in for parallel direction of the magnetic field is 140%, whereas the thermal conductivity decreases 125% for perpendicular direction. The same group (Krichler & Odenbach, 2013b) carried out magnetic field dependent thermal conductivity measurements with commercial synthetic hydrocarbon-based Fe_3O_4 magnetic nanofluids at volumetric concentrations of 3.51 and 1.69%. They used a planar measurement cell to measure the thermal conductivity and used a cylindrical coil to obtain an external magnetic field in parallel and perpendicular to the heat flux between 0-40 kA/m. They observed that the thermal conductivity increases up to 420% for parallel direction and decreases up to 185% for the perpendicular direction.

Nkurikiyimfura, Wang & Pan (2013) prepared magnetic nanofluid samples with different volumetric concentrations up to 5% by dispersing oleic acid-coated magnetite particles in engine oil. The measurements were conducted by Hot Disc TPS2500 thermal constants analyzer. In order to a generate magnetic field up to 200 G, NdFeB permanent magnet was used. The results revealed an enhancement in the thermal conductivity up to 250% for the parallel orientation and up to 105% for perpendicular orientation.

Cheng et al. (2014) prepared Fe-silicon oil magnetic nanofluids at five different volumetric concentrations of 0.1, 0.3, 0.5, 0.7 and 0.9% and measured their thermal conductivity with a thermal property analyzer under a narrow magnetic field range between 2 to 10 mT. The maximum enhancement was observed as 34% at 10 mT magnetic field.

Karimi, Afghahi, Shariatmadar & Ashjaee (2014) prepared two different water-based magnetic nanofluids with $CoFe_2O_4$ and Fe_3O_4 nanoparticles with 0-4.8 vol. % concentration and measured the thermal conductivity under external magnetic field by using the transient hot-wire method (KD2 Pro). An electromagnet was utilized in order to generate the magnetic field up to 500 G. The results showed that the thermal conductivity increases for both samples, and the maximum thermal conductivity enhancements are 196% and 148% for Fe_3O_4-water and $CoFe_2O_4$-water, respectively. They also reported that Fe_3O_4-water magnetic nanofluids have higher thermal conductivity values than $CoFe_2O_4$-water.

Parekh (2014) studied the thermo-magnetic properties of $Mn_{0.5}Zn_{0.5}Fe_2O_4$–light hydrocarbon oil magnetic nanofluid. The thermal conductivity of magnetic nanofluid samples with volumetric concentrations of 1-10% was measured with the Lambda system under the magnetic field generated by a solenoid. Under varying magnetic field strength from 0 to 800 Oe, the results showed the maximum thermal conductivity enhancement was 45% for the sample with 10 vol. % concentration.

Karimi, Goharkhah, Ashjaee & Shafii (2015) investigated the thermal conductivity of magnetite-water and hematite-water magnetic nanofluids under a uniform magnetic field. They have carried out the experiments in the volumetric concentration range of 0-4.8% and the temperature range of 20-60˚C with transient hot-wire method. An electromagnet was used to generate a uniform magnetic field. Their results showed that thermal conductivity enhanced 175% for magnetite nanofluid and 38.5% for hematite nanofluid at 2 vol. % concentration.

Cherief et al. (2015) measured the thermal conductivity of kerosene and mineral oil-based Fe_3O_4 magnetic nanofluids under the magnetic field which was generated by an electromagnet. The magnetic field was applied in the parallel direction to the probe axis. They prepared the magnetic nanofluid samples at 5 vol. % concentration for kerosene and 7.3% for mineral oil. The measurements were held by using transient hot wire (KD2 Pro) under 0-750 mT external magnetic field strength. The results indicated that the maximum thermal conductivity enhancement is 20%.

Patel, Parekh & Upadhyay (2015) dispersed oleic acid-coated $Mn_{0.6}Zn_{0.4}Fe_2O_4$ ferrite nanoparticles in transformer oil with four different vol. concentrations of 1.6%, 3.2%, 6.8% and 10.3%. The thermal conductivity was measured with the transient hot-wire technique (Decagon KD2 Pro). They utilized permanent rare earth magnets to create external magnetic field up to 2260 G. They observed an enhancement in the thermal conductivity about 100% with the maximum field.

Suh & Cho (2015) studied on Fe_3O_4-kerosene magnetic nanofluid with 0.5-7.2 vol. % concentration. The thermal conductivity was measured with the transient hot-wire method by varying the magnetic field intensity in parallel and perpendicular alignments using both Helmholtz coil (0-600 G) and permanent magnets (0-1600 G). The results indicated that there is no change in thermal conductivity for both parallel and perpendicular cases with Helmholtz coil. However, they observed a maximum 25% enhancement with permanent magnets over 1000 G field strength.

Sundar, Ramana, Singh & Sousa (2015) measured the thermal conductivity of Fe_3O_4-vacuum pump oil magnetic nanofluid with volumetric concentrations of 0.05 to 1% by KD2 Pro. They used permanent magnets to generate a magnetic field between 0-2100 G. They concluded that the thermal conductivity increased up to 69% until the magnetic field strength of 1300 G, then it decreased.

Azizian, Doroodchi & Moghtaderi (2016) et al. considered 0.86 vol. % concentrated Fe_3O_4-water magnetic nanofluid for the thermal conductivity measurements by KD2 Pro. They employed electromagnets to apply a magnetic field parallel to the temperature gradient between 0-30 mT. They also used solenoid for generating a perpendicular magnetic field. Measurements showed that the thermal conductivity increases by up to 167%. They concluded that the magnetic field causes a controlled aggregation of magnetic nanoparticles.

Katiyar, Dhar, Nandi & Das (2016) dispersed Fe, Ni and Co particles into ethylene glycol and HTO with different volumetric concentrations from 1 to 7% for each one of the particles. They measured the thermal conductivity of the samples using a commercial thermal conductivity meter (KD2 Pro) under the applied magnetic field which was generated by a custom made electromagnet. Thermal conductivity enhances up to 260% for Fe/EG and 280% for Fe/HTO, 200% for Ni/EG and 240% for Ni/HTO, 175% for Co/EG and 225% for Co/HTO. Although; Ni and Co have higher thermal conductivity when compared to Fe, they observed that Ni and Co-based magnetic nanofluids have less capability to conduct the heat compared to Fe-based magnetic nanofluids at the same magnetic field and concentration due to small magnitude of saturation moment of Ni and Co nanoparticles.

Arana, Bercoff & Jacobo (2017) studied the influence of the magnetic field on the thermal conductivity of kerosene-based $NiFe_2O_4$ magnetic nanofluids. They measured the thermal conductivity of the samples with 5 and 10 vol. % concentrations by the transient hot-wire method. Permanent magnets were used as the magnetic field source. Under the applied magnetic field in value of 0-0.14 T, they observed a thermal conductivity enhancement of about 170% for 10% vol. concentration.

Ebrahimi & Saghrayani (2017) investigated the influence of the magnetic field on thermal conductivity for water-based Fe_3O_4 magnetic nanofluids with a weight concentration of 3, 5, and 7% which was also mixed with different concentrations of CuO nanoparticles. They used a DC magnet for generating a magnetic field in order to measure magnetic field dependent thermal conductivity with the transient hot-wire method. The thermal conductivity enhanced about 4.7% under a 0.2 T parallel magnetic field.

Lenin & Joy (2017) used four different types of surfactants (stearic, oleic, linoleic, and linolenic acid) to coat Fe_3O_4 nanoparticles. The nanoparticles were dispersed in toluene at 2.2 vol. % concentration. The measurements were held using the transient hot-wire method under the applied magnetic field between 0 and 0.16 T generated by an electromagnet. The maximum enhancement observed was 57% for the linoleic acid-coated sample at 0.08 T. The enhancement differences between the samples with other surfactants were explained as the interparticle magnetic interaction is larger for saturated fatty acid-coated magnetic nanofluids than the unsaturated ones.

Vinod & Philip (2017) prepared kerosene-based Fe_3O_4 magnetic nanofluid samples with vol. fractions of 0.037 and 0.063 to analyze the thermal conductivity variations under the influence of the magnetic field. The magnetic field was applied with

Helmholtz coil in the parallel and perpendicular directions for magnetic field strength of 0-250 G and 0-150 G, respectively. The measurements were carried out by using a hot disc thermal constants analyzer TPS 2500. The results presented that the thermal conductivity enhances up to 130% at 150 G for parallel, where it enhances 10% for perpendicular direction.

Dadwal & Joy (2018) used toluene-based Fe_3O_4 magnetic nanofluids and coated the particles with three different surfactants; myristic acid, palmitic acid and stearic acid. They prepared samples with different vol. concentrations of 0.5-4% for all surfactant. Thermal conductivity measurements were carried out under an external magnetic field applied parallel to the temperature gradient in the range of 0 to 1600 Oe at room temperature. The results indicated that the solution with myristic acid as a surfactant shows the maximum enhancement in thermal conductivity (14.69%). These results showed that different surfactant molecules interdigitate with each other differently; thus the clustering of the magnetic nanoparticles varies for every surfactant.

Lenin, Dadwal & Joy (2018) studied the thermal conductivity of short-chain and long-chain fatty acid surfactant coated magnetic nanofluids under the magnetic field using the transient hot-wire method. Capric acid and stearic acid coated Fe_3O_4 magnetic nanoparticles were dispersed in toluene separately at 2.2 vol. % concentration. The measurements were carried out under an external magnetic field applied by an electromagnet in the range of 0 to 1 T parallel to the temperature gradient. Maximum thermal conductivity enhancement for a capric acid-coated sample was 145% at 0.71 T, and for the stearic acid-coated sample was 129% at 0.95 T. They pointed out that the enhancement amount varies between the samples due to the thickness differences between the surfactant layers.

Nagvenkar et al. (2018) investigated the surfactant effect on thermal conductivity using poly (vinylpyrrolidone) (PVP) coated and uncoated α-Fe_2O_3-decanol magnetic nanofluid samples at 0.01–0.05 vol. % concentrations. They measured the thermal conductivity under the magnetic field and the results showed that at 1120 G for 0.05

vol. %, the PVP coated magnetic nanofluid's thermal conductivity enhanced about 28%, where the uncoated magnetic fluid's thermal conductivity enhanced about 35%.

Devi, Rao & Kumar (2018) investigated the thermal conductivity of the Fe_3O_4-water magnetic nanofluid under the effect of a magnetic field for water-based Fe_3O_4 nanofluid. They measured the thermal conductivity for nanofluid samples with volumetric concentrations 1, 2, 3, 4 and 5% by using the KD2 probe. The results indicated that thermal conductivity increases up to 30% for 500 G magnetic field strength.

Gui, Stanley, Nguyen & Rosengarten (2018) used five different commercial water-based Fe_3O_4 magnetic nanofluids, EMG308, EMG408, EMG707, EMG708, and EMG807 with different volumetric concentrations of 0.4-1.1, 1-4, and 1-8%. Other differences between the commercial magnetic nanofluids were surfactant quantity, density, and saturation magnetization. They prepared samples for the measurements by using 5 and 10% from commercial magnetic nanofluid and water for the rest of the mixture. The thermal conductivity measurements were carried out by KD2 Pro thermal property analyzer under the external magnetic field generated by permanent magnets. The magnetic field strength was altered as 10, 20, 30, 40, and 50 mT. Maximum thermal conductivity enhancement was observed 100% for the sample which has 10% of EMG708 content.

Salazar, May, Pinzon, Esquivel & Gil (2018) studied the effect of loading the Fe_3O_4-light hydrocarbon oil with carbon nanofibers on thermal conductivity of the fluid. They used micro-sized carbon nanofibers and prepared samples with vol. concentrations of 0.25, 0.5, 1, 2, and 5%. The samples were measured using the thermal wave resonator cavity technique under a magnetic field applied by a Helmholtz coil at 750 G parallel and perpendicular to the temperature gradient. The maximum thermal conductivity enhancement was observed at 5 vol. %, 110% for perpendicular and 160% for the parallel direction of the magnetic field.

Vinod & Philip (2018) studied with kerosene-based Fe_3O_4 magnetic nanofluid with different particle sizes. They measured the thermal conductivity of these samples at 0.037 volumetric fraction with three different particle sizes of 8.3, 9.6, and 10.5 nm. Measurements were made with the transient hot-wire method under the influence of the external magnetic field generated by a solenoid. The measuring process was carried out when the magnetic field applied is in parallel and perpendicular directions in the range of 0-250 G and 0-150 G, respectively. The results of the measurements showed that the highest enhancement on thermal conductivity was 127% at 160 G magnetic field strength for the sample with 9.6 nm. They also pointed out that the thermal conductivity enhances less than 10% under the perpendicular magnetic field.

Wang et al. (2018) measured the thermal conductivity of Fe_3O_4-pump oil and Fe_3O_4-silicon oil magnetic nanofluids with 0.17% vol. concentration under the applied magnetic field. The measurements were held by hot disc thermal constants analyzer TPS 2500. The magnetic field was applied in the range of 0-700 G parallel to the temperature gradient. The results presented that there is no obvious thermal conductivity enhancement under the magnetic field.

Hajiyan, Ebadi, Mahmud, Biglarbegian & Abdullah (2019) employe Fe_3O_4-glycerol magnetic nanofluid with different vol. concentrations between 0.5-3%. They used KD2 Pro to measure the thermal conductivity under the influence of the magnetic field. The magnetic field was generated with electromagnets between 0-543 G. The results depicted that the thermal conductivity increased up to 16.9% for maximum particle concentration and magnetic field strength.

Goharkhah, Gharhkhani, Fallah & Ashjaee (2019) have investigated the dynamic thermal conductivity of Fe_3O_4-water magnetic nanofluid in a pipe for 1 and 2% vol. concentration. They utilized electromagnets to create a magnetic field up to 800 G. They have first determined the radial temperature distribution in the pipe. Then, they assumed that there is no heat loss in the pipe. Therefore, the amount of the transferred heat is considered as equal to the given power. Finally, they have calculated the thermal conductivity by Fourier's Law. The results indicated that the dynamic thermal conductivity of the thermal conductivity increases by up to 32.3% for 2 vol. % concentration at 800 G.

Table 1.3 Comparison of key studies on thermal conductivity of magnetic nanofluids

Authors	**Particle**	**Base type**	**φ (vol.)**	**MF Strength (G)**	**Max. Enhancement**
Shima et al. (2009)	Fe_3O_4	Kerosene	0.11-1.71	0-500 G for //	300%
Parekh et al. (2011)	Fe_3O_4	Kerosene	0-10	~800 Oe	~40%
Gavili et al. (2011)	Fe_3O_4	Water	500%	0-1000 G for //	200%
Nkurikiyimfura et al. (2013)	Fe_3O_4	Engine oil	0.-0.5	0-0.02 T for // and ⊥	250% for // 105% /⊥
Karimi et al. (2014)	Fe_3O_4	Water	0-4.8	0-500 G for ⊥	196%
Sundar et al. (2015)	Fe_3O_4	Pump oil	0.05-1	0-2100 G for //	~570%
Azizian et al. (2016)	Fe_3O_4	Water	0.86	0-32 mT for // and ⊥	167%
Ebrahimi et al. (2017)	Fe_3O_4	Water	3-7 wt. %	0.1 and 0.2 T for //	~4.7%
Vinod et. (2017)	Fe_3O_4	Kerosene	3.7, 6.3	0-250 G for // 0-150 G for ⊥	130% for // ~10% for ⊥
Praveena et al. (2018)	Fe_3O_4	Water	0-5	0-500 G	30%
Wang et al. (2018)	Fe_3O_4	Pump oil	0.17	0 - 700 G //	-

Table 1.3 summarizes the key studies on the thermal conductivity of magnetic nanofluids. Similar to the viscosity, it is observed that there are three main contradictions:

- Lower magnetic field strength, but higher thermal conductivity enhancements in the presence of the magnetic field.

- Similar concentrations, similar magnetic field strength, but different thermal conductivity enhancements in the presence of the magnetic field.

- Anomalous increments in thermal conductivity with relatively low particle content.

1.3.2 Micropumping Applications of Magnetic Nanofluids

Micropumps are devices that are able to transport fluids with tiny quantities in microliters or millilitres level from a reservoir to a target in micro-sized channels or tubes (Mohith, Karanth, & Kulkarni, 2019).

One of the earliest attempts for the micropump design was performed in 1978 by Spencer, Corbett, Dominguez & Shafer (1978). In this pioneering design, a piezoelectric material was used. Van Lintel, Van Depol & Bouwstra (1988), on the other hand, used a piezoelectric disk for the actuation of a micropump which is made by micromachining of a silicon wafer. Similarly, Esashi, Shoji & Nakano (1989) utilized a piezo-actuator in order to move a diaphragm for micropumping, and they observed a flow rate of 20 μL/min.

In addition to the earliest piezoelectric actuation concepts, various micro-pumping actuation types have been implemented such as electrostatic (Ng, Jiang, Li, Lam, & Reddy, 2004), pneumatic (Huang, Huang, & Li, 2006), magnetic fluid displacement (Yamahata, Lotto, Al-Assaf, & Gijs, 2005), peristaltic (Wang & Lee, 2006), magnetohydrodynamic (Eijkel, Dalton, Hayden, Burt, & Manz, 2003), electrohydrodynamic (Darabi, Rada, Ohadi, & Lawler, 2002), electroosmosis (Zeng, Chen, Mikkelsen, & Santigo, 2001), and electrowetting (Hsieh et al., 2003).

The categorization can be further improved, as mentioned by Iverson & Garimella (2008) as it is in Figure 1.2.

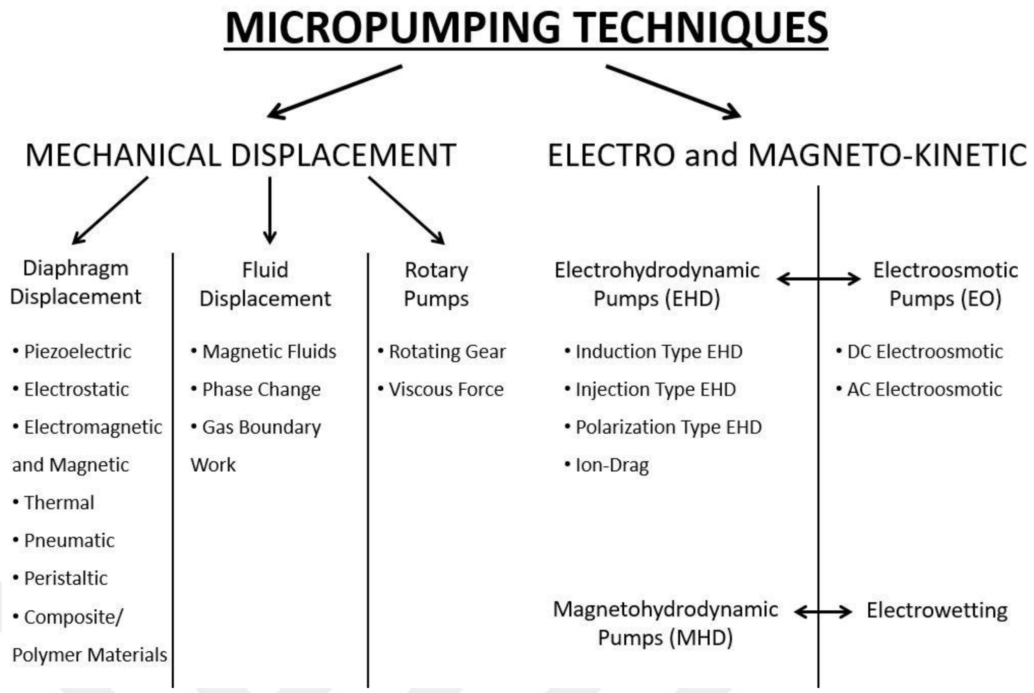

Figure 1.2 Schematic for categorization of micropumping techniques adopted from Iverson & Garimella (2012)

Due to the contactless operation, micropumps with magnetically actuated fluids have attracted the interest of the researchers' (Ando, Baglio, & Beninato, 2011). Hatch, Kamholz, Holman, Yager & Bohringer (2001) considered magnetically actuated magnetic nanofluid (APG E18) plugs in order to manipulate water inside a circular microchannel by neodymium magnet (Figure 1.3a). The magnet was placed on a rotor and driven by a DC motor. The rotor was rotated in the trajectory of the microchannel, and the magnetic nanofluid was actuated. They concluded that by varying the geometry of the device and adjusting the motor speed, a precise flow control could be achieved.

Ahn, Oh & Choi (2004) studied a novel type of magnetic nanofluid based microfluidic system. The purpose of this system was to be used in micro-sized delivery systems for medicine and biology. They prepared three different channels with the dimensions of 1000×100 μm, 500×100 μm and 100×100 μm. They used a permanent magnet attached in a rotor similarly for magnetic actuation (Figure 1.3b). A synthetic iso-paraffinic magnetite ferrofluid plug was used in the system to pump the water. The maximum flow rate with the proposed design is observed as 37 μL/min.

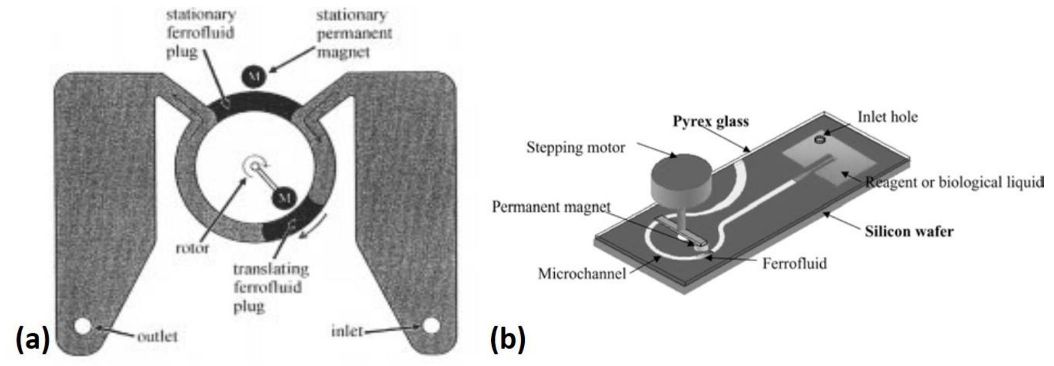

Figure 1.3 Schematics of the setup by (a) Hatch et al. (2001), and (b) Ahn et al. (2004)

Hartshorne, Backhouse & Lee (2004) employed a microfluidic pump fabricated from etched glass substrates. The proposed device contains a magnetic nanofluid plug composed of ferromagnetic particles in a hydrophobic fluorocarbon carrier in a 10 mm length (Figure 1.4). They successfully pumped water with the employed magnetic nanofluid in a linear channel with the dimensions of 50×20 μm.

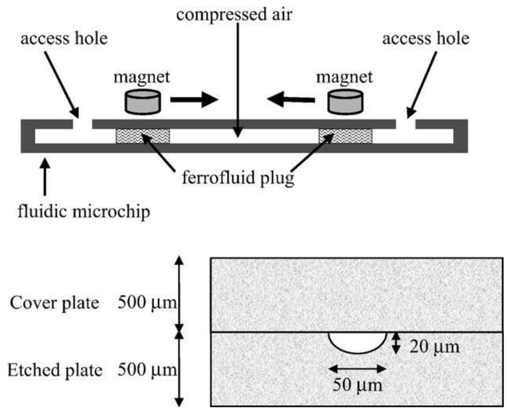

Figure 1.4 Schematic of the setup by Hartshorne et al. (2004)

Yamahata et al. (2005) proposed a fluid displacement micropump by using a magnetic nanofluid plug as an actuator (Figure 1.5). They prepared iron oxide-based magnetic nanofluids and utilized it as a piston based on its oscillatory motion. The magnetic nanofluid was supplied to the channel by a syringe, and its position was controlled by an external rare earth magnet with 1200 mT magnetic remanence. In order to convert the motion of magnetic nanofluid plug into an intermittent fluid flow between input and output tanks, two check valves were used. They successfully pumped the water with flow rates up to 30 μL/min.

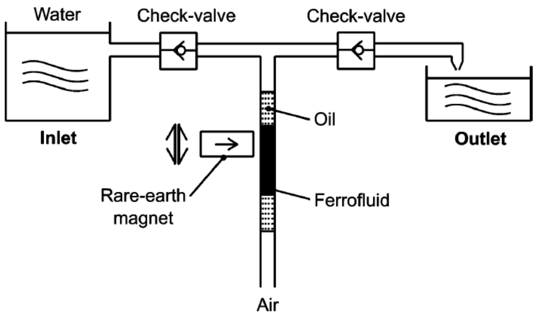

Figure 1.5 Schematic of the setup by Yamahata et al. (2005)

Sim, Oh & Choi (2006) utilized kerosene-based magnetite magnetic nanofluid sample in order to actuate a Parylene diaphragm for micropump applications. They have measured the deflection of the diaphragm which will influence the pumping capability for different magnetic field intensity values. An electromagnet was used for magnetic field generation. The results confirm that it is possible to actuate the diaphragm with magnetic nanofluid, and the deflection increases with increasing magnetic field intensity.

Kim, Oh & Choi (2006) used two permanent magnets attached at either end of a link that is mounted on a step motor to achieve a continuous peristaltic pumping (Figure 1.6). The system includes two pumping microchannels, which were separated with a membrane. The rotation of the motor shaft actuates the magnetic nanofluid plug (10.7 vol. %) inside the primary channel, and the movement of the magnetic nanofluid plug causes a deflection on the membrane, which drives a secondary fluid inside the adjacent channel. A similar concept was also studied by Lee, Kuan & Sung (2011) to drive the fuel in direct methanol fuel cells. Studies that are summarized above reveal that magnetic actuation occurs by changing the position of the magnets during the operation. That is, it is crucial to investigate how fast the magnets vary in their positions.

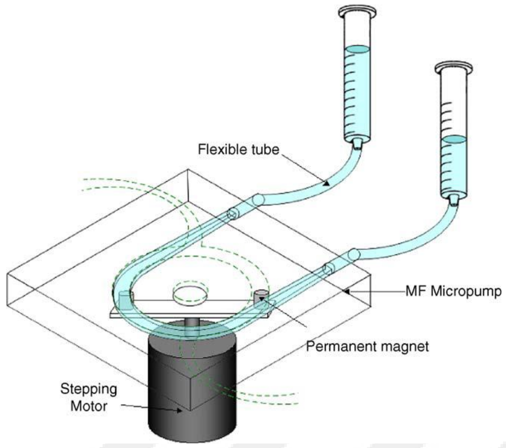

Figure 1.6 Schematic of the setup by Kim et al. (2006)

Lee, Leong, Wang, Fu & Chen (2012) proposed a novel micropump, which includes two magnetic nanofluid plugs (EMG 901). They used PMMA-based circular microchannels with a constant depth of 460 μm and varying width of 250-1000 μm (Figure 1.7). A step motor was used to rotate a permanent magnet that is attached to a motor link with various angular velocities, which vary from 2 rpm to 8 rpm. The results indicated that the flow rate increases with increasing the channel width and motor velocity.

In a similar study, Fu, Fang, Hong & Lee (2014) investigated the influence of the motor velocity and channel geometry as an orthogonal and tangent type with a similar magnetic nanofluid sample of EMG 901. Similarly, the results showed that the flow rate increases with increasing the motor velocity, and no significant changes are observed for orthogonal and tangent type channel geometries.

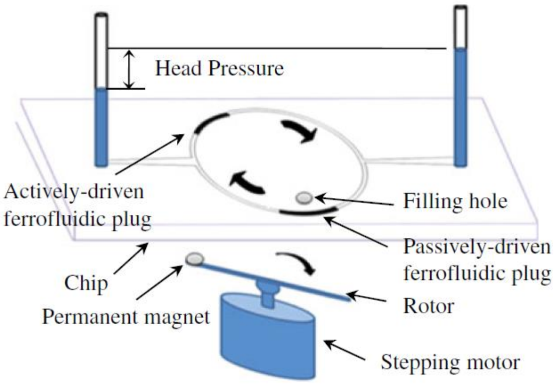

Figure 1.7 Schematic of the setup by Lee et al. (2012)

Kurtoglu et al. (2012) investigated the continuous and discontinuous actuation of the Fe_3O_4-water magnetic nanofluid in a microtube with a diameter of 254 μm (Figure 1.8). Permanent magnets were held on each surface of rotors with two different shapes of prisms, i.e., rectangular and hexagonal prisms, for discontinuous actuation and a conveyor belt for continuous actuation. They have also altered the motor speed for both methods. The results depicted that the magnetic nanofluid flow rate increases with increasing motor speed. Moreover, the max flow rates observed are very close to each other for all cases.

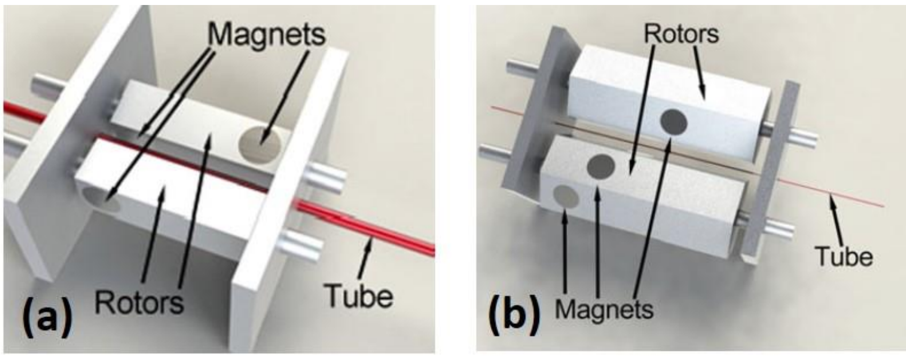

Figure 1.8 Schematics of the setup by Kurtoglu et al. (2012) for (a) rectangular, and (b) hexagonal rotor structures

Assadsangabi, Ali & Takahata (2012) proposed a magnetic nanofluid control method provides both attractions and repelling with the aid of micropatterned planar coils and permanent magnets. They utilized an oil-based commercial magnetic nanofluid sample (EFH1). The permanent magnets were employed to keep magnetic nanofluid on the micropatterned planar coils. Then, it is moved with the magnetic field created by the coils. The results confirmed that the magnetic nanofluid sample could be bidirectionally moved in a linear path for micropumping purposes.

Chang, Hu & Lin (2013) magnetically actuated a magnetic nanofluid plug in order to enhance the biochemical reaction. The magnetic nanofluid consists of Fe_3O_4 nanoparticles and silicone oil and hexane mixture. Similar to the concept of Hatch et al. (2001), a magnetic nanofluid plug was kept stationary with a fixed permanent magnet, and another one is kept moving with a translating permanent magnet. The magnetic actuation was made in a PDMS circular microchannel with a 2 mm width and 500 μm depth. They concluded that the biochemical reaction by nitrocellulose slide could enhance the proposed micropumping concept.

Banerjee, Sbareesh & Sen (2017) manipulated a commercial water-based magnetic nanofluid sample (EMG 408) in a linear microchannel (Figure 1.9). The experiments were carried out for two cases of stationary and moving permanent magnets. According to observations, the magnetic nanofluid in the microchannel can be manipulated a velocity value of up to 5 mm/s. Also, the magnetic nanofluid sample can be bidirectionally manipulated and the velocity can be controlled by altering the speed of moving magnet.

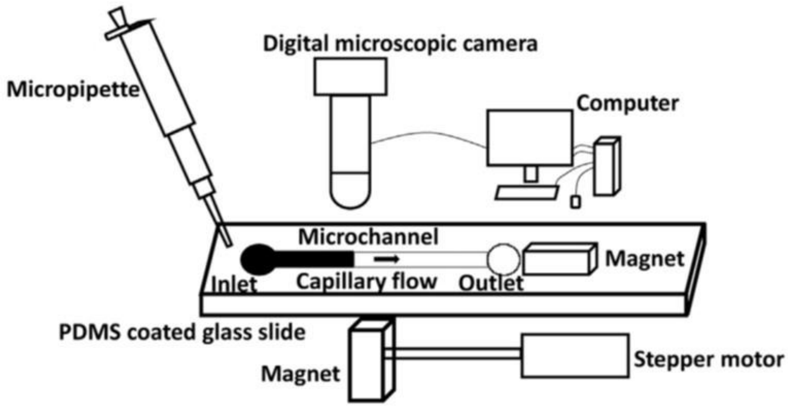

Figure 1.9 Schematics of the setup by Banerjee et al. (2017)

Ashouri, Shafii & Moosavi (2017) presented the design, fabrication and performance of a valveless micropump with magnetic actuation. They have placed a cylindrical permanent magnet in a pumping cylinder which behaves like a piston (Figure 1.10). The permanent magnet was covered by an oil-based magnetic nanofluid (EFH1) with 10 nm particle size and 7.9 vol. %. It was moved by a rectangular-shaped permanent magnet which was moved by a motor. The pumping chamber has a 1 mm width and 560 μm. The results indicated that the proposed design could successfully pump the water which is immiscible with magnetic nanofluid samples with flow rate values up to 700 μL/min.

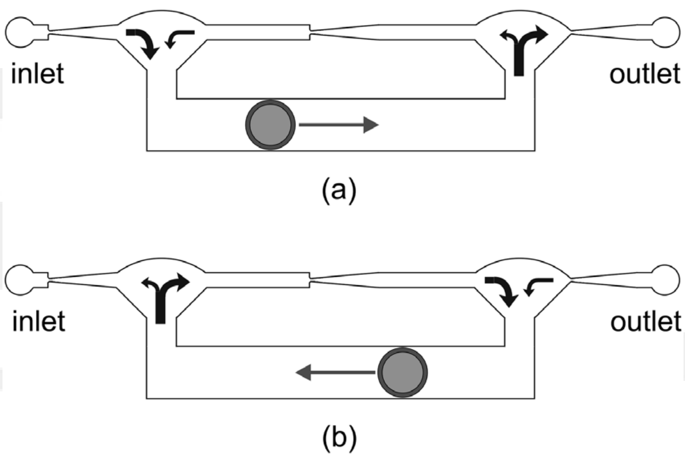

Figure 1.10 Schematics of the setup by Ashouri et al. (2017) for (a) pumping, and (b) return strokes

Liu, Zhang, Yang, Yang & Li (2018) proposed a novel C-shaped baffle-based ferrofluidic micropump in order to manipulate an immiscible secondary fluid (Figure 1.11). They used a commercial magnetic nanofluid in a square microchannel with a width of 600 μm; and varied the actuation speed from 10 rpm to 20 rpm. The experimental results showed that the flow rate increases up to a specific actuation speed, then it starts to decrease.

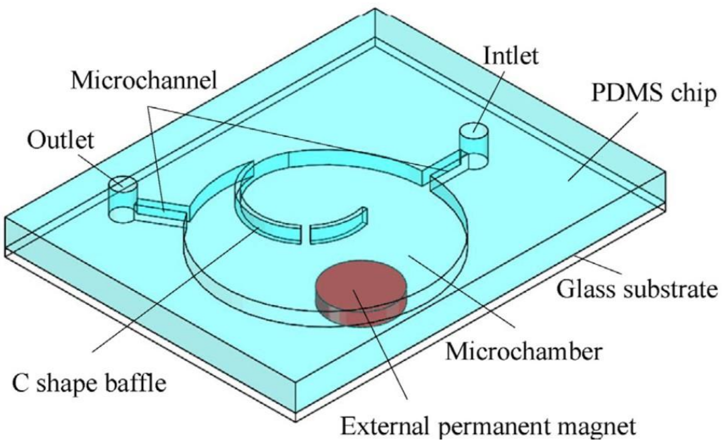

Figure 1.11 Schematics of the setup by Liu et al. (2018)

1.4 Research Gaps

According to the extended literature survey, the research gaps arise as follows:

- It is observed that viscosity and magnetic properties of nanofluids were not experimentally determined and presented in most of the available micropump studies although they directly affect magnetic fluid and microchannel interaction and are therefore critical for micropump operation limits and efficiency, i.e. actuator speed, and flow rate. The determination of these properties of the magnetic nanofluid will assist in understanding the characteristics of the valveless micropump. Also, utilizing these values in the numerical simulations will increase the reliability of the numerical results,

- There are many studies that deal with the thermal conductivity of magnetic nanofluids under the influence of the external magnetic field to investigate their usage for thermal management systems. Since the available studies do not provide a detailed magnetic field behavior in the measurement region, the results of them indicate that there is a contradiction in terms of enhancement amount of thermal conductivity. In this thesis, the thermal conductivity of the magnetic nanofluid will be investigated in the presence of the magnetic by considering and quantifying the non-uniform behavior of the applied magnetic field,

• The available actuator installations are mostly based on intuitive approaches and limited to the basic observations on the magnetic field around magnets. In other words, the magnetic field strength on the microchannel was not discussed sufficiently. That is, proposed systems were far from being generalized rather their implementation is possible for a specific scenario. Addressing this gap by an analytical actuator design methodology referring to quantitative evaluation criteria will make it possible to redesign and implement it in various scenarios,

• It is not easy to determine real-time fluid velocity inside micro-sized channels with conventional methods. By developing a digital image processing strategy, the real-time velocity of the magnetic nanofluid inside the valveless micropump will be measured. To the best of the author's knowledge, it will be proposed for the first time in the available literature,

• There is no precise control process applied for controlling the magnetic nanofluid flow for present magnetically actuated micropumps in the available literature. In this thesis, a closed-loop control process will be applied in order to control the magnetic nanofluid velocity.

1.5 Objectives and Contributions of the Thesis

The main goal of this thesis is to design a magnetically actuated valveless micropump and control of the magnetic nanofluid flow inside it. To contribute to the research gaps that arise from the extended literature survey, followings are the objectives:

• Investigation of the magnetic properties, viscosity and thermal conductivity of the magnetic nanofluid to design a micropump with various purposes,

• Design a novel magnetic actuator for the valveless actuation of the magnetic nanofluid,

- Design and production of a microchannel for magnetic nanofluid flow,
- Investigation of the magnetic field behavior within the microchannel region,
- Investigation of the magnetic nanofluid flow inside the valveless micropump both numerically and experimentally,
- Development of a digital image processing algorithm to measure the real-time velocity of the magnetic nanofluid,
- Development of a controller unit and strategy to control the magnetic nanofluid flow inside the valveless micropump,
- Investigation of the magnetic nanofluid flow inside the valveless micropump with a controller.

CHAPTER TWO
PROPERTIES OF MAGNETIC NANOFLUID

2.1 Introduction

Before using the magnetic nanofluid inside the micropump, it is important to investigate its properties to have an insight into the behavior of the magnetic particles in the base fluid. As mentioned in the motivation section, it is aimed to design a valveless micropump which can be used for two main purposes, i.e., *(i)* generating a magnetic nanofluid flow to manipulate a secondary fluid, and *(ii)* generating a magnetic nanofluid flow for thermal management of electronics. For the former purpose, viscosity and magnetic properties are going to have a significant influence on the magnetic nanofluid flow. For the latter purpose, also an investigation of the thermal conductivity will be remarkable to discuss the potential of the valveless micropump. In this chapter, firstly, the viscosity and magnetic properties of the magnetic nanofluids are investigated. Following, the thermal conductivity is measured in both the absence and presence of the external magnetic field.

2.2 Magnetic Nanofluid Preparation

Fe_3O_4-water magnetic nanofluid was supplied from US Research Nanomaterials Company as a dispersion with 4.8 vol. %. The properties of the Fe_3O_4 nanoparticles inside the dispersion provided by the supplier are shown in Table 2.1.

Table 2.1 Properties of Fe_3O_4 magnetic nanoparticles (Fe_3O_4 iron oxide nanoparticles, n.d.)

Parameter	**Value**
Particle size	15-20 nm
Density	4.8-5.1 g/cm^3
Purity	99.5+%
Shape	Spherical
Magnetic Saturation	60.45 emu/g

In order to test the influence of the magnetic nanoparticle concentration on properties, it was diluted to different vol. concentrations of 1, 2, 3 and 4% with distilled water. To ensure the stability of the magnetic nanofluid samples, the diluted samples were ultrasonicated by probe type Misonix Sonicator 3000 model ultrasonicator (Figure 2.1).

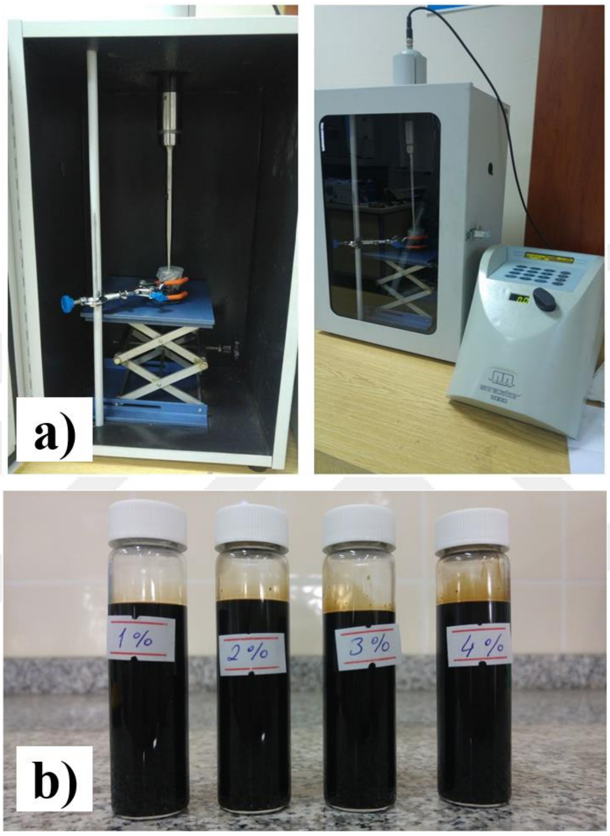

Figure 2.1 (a) Probe type Misonix Sonicator 3000 model ultrasonicator, (b) Images of the diluted and ultrasonicated Fe_3O_4 samples (Personal archive, 2018)

2.3 Viscosity

2.3.1 Measurement Method

The viscosity of Fe_3O_4-water magnetic nanofluid samples with different particle concentrations of 1, 2, 3, 4 and 4.8 vol. % was measured with a vibrational type viscometer (SV-10, A&D Japan). The device is able to conduct viscosity measurements between 0.3 mPa·s and 10000 mPa·s with 1% accuracy. The schematic representation of the vibrational viscometer is presented in Figure 2.2. The viscometer has two electromagnetically driven sensor plates. Both plates are sinusoidally vibrated via the electromagnetic drive unit at the same frequency. The drive unit also provides sensor plates to keep vibrating at the constant amplitude. The electric current required for vibrating the sensor plates is detected as the measure of viscidity which occurs between the sensor plates and fluid samples. Then, the correlation between the viscidity and the driving electric current determines the viscosity of the sample (Turgut et al., 2009).

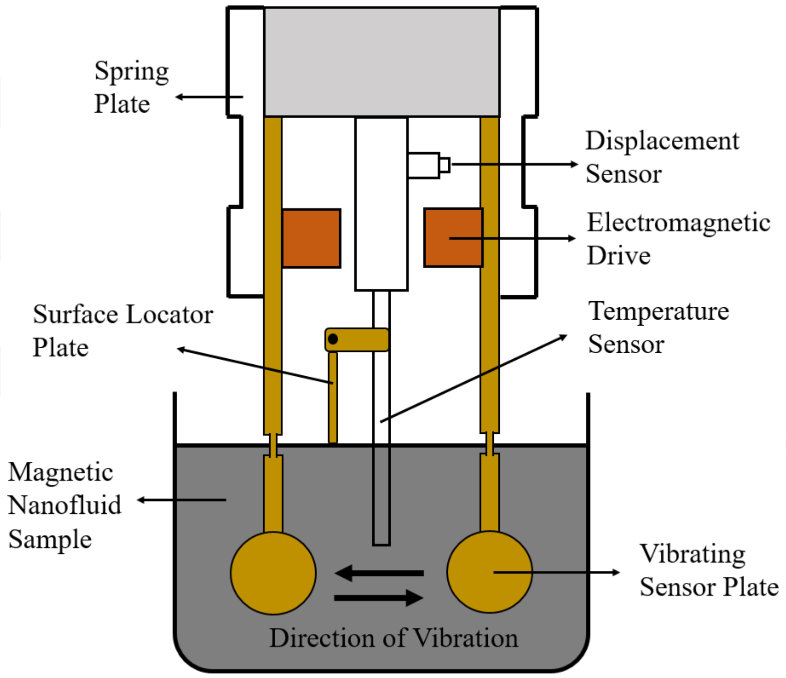

Figure 2.2 Schematic representation of the SV-10 vibrational viscometer modified from Turgut et al. (2009)

2.3.2 Results and Discussions on Viscosity

The results of viscosity measurements are presented as relative viscosity between the magnetic nanofluid and the base fluid. It is the ratio between the viscosity of the magnetic nanofluid sample and the base fluid (Equation 2.1).

$$\mu_r = \frac{\mu_{mnf}}{\mu_{bf}} \tag{2.1}$$

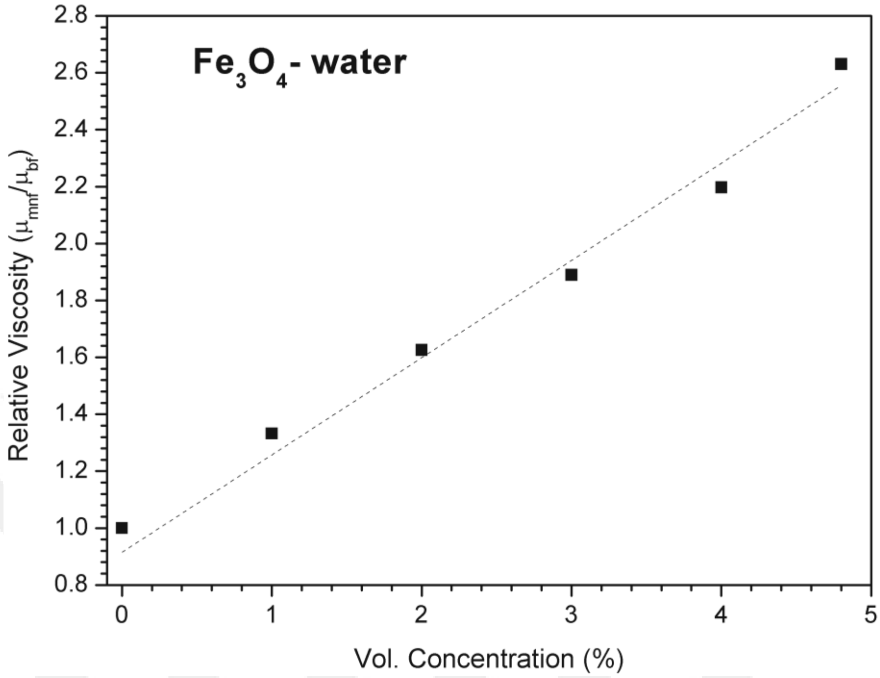

Figure 2.3 Relative viscosity variation of magnetic nanofluid samples

Figure 2.3 demonstrates that the relative viscosity variation of Fe_3O_4-water magnetic nanofluid samples with respect to the volumetric particle concentration. It is clearly seen from the figure that the relative viscosity increases with increasing magnetic nanoparticle concentration. The maximum relative viscosity value is obtained about 2.6 for Fe_3O_4-water magnetic nanofluid sample with 4.8 vol. %.

The reason for increasing viscosity with the addition of magnetic nanoparticles can be explained by increasing flow resistance, since, the solid magnetic particles behave as obstacles in the liquid. Moreover, if the suspension becomes denser, the resistance to the flow by particles increases. This explains the relative viscosity increment by increasing magnetic nanoparticle concentration. Additionally, it can be said that the relative viscosity increases very close to a linear behavior.

2.4 Magnetic Properties

2.4.1 Measurement Method

Magnetic properties of the Fe_3O_4-water magnetic nanofluid samples with different particle concentrations of 1, 2, 3, 4 and 4.8 vol. % were measured by the vibrating sample magnetometer (VSM) method. The schematic of the VSM method is provided in Figure 2.4. The method was first proposed by Simon Foner in 1955. Since then, it is very common for determining of magnetic properties of magnetic materials (Foner, 1959).

In this method, a magnetic sample is placed on the tip of a rod, which is placed in a uniform magnetic field. The magnetic field is generated by two conjugate electromagnets. Then, the rod is sinusoidally vibrated in the vertical direction by a piezoelectric material. Due to the oscillating magnetic field of the vibrating sample, a voltage is induced in the stationary pick-up coils which are placed parallel to the uniform magnetic field—resulting voltage in the pick-up coils directly proportional to the magnetic moment of the magnetic material. Hence, the magnetization of the sample can be determined. In this study, a VSM by "Dexing Magnet VSM 550" was employed for the measurements. The device is able to generate a magnetic field up to 3.5 T. The accuracy and repeatability of the device are better than ±1% in the range of 0-30 emu/g (Vibrating sample magnetometer, n.d.).

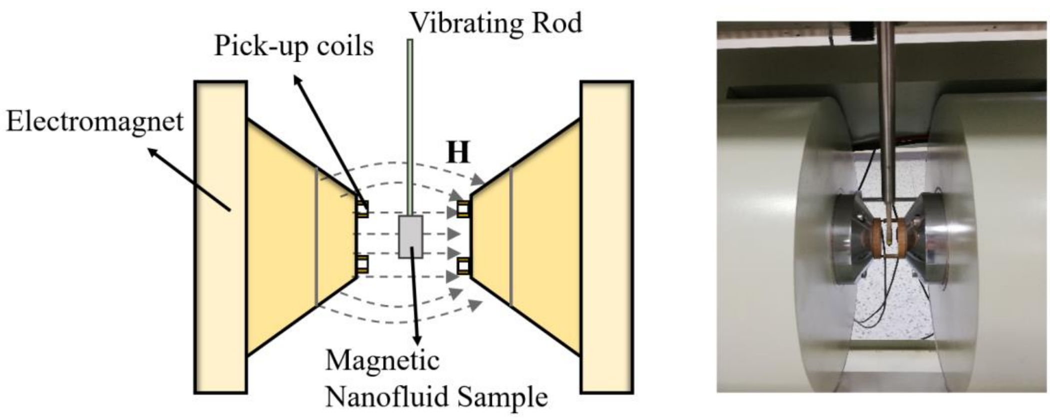

Figure 2.4 Schematic representation of vibrating sample magnetometer (VSM) (Personal archive, 2018)

2.4.2 Results and Discussions on Magnetic Properties

Magnetization curves (H-M) of the Fe_3O_4-water samples are obtained as it is seen in Figure 2.5 by measurements with the VSM method.

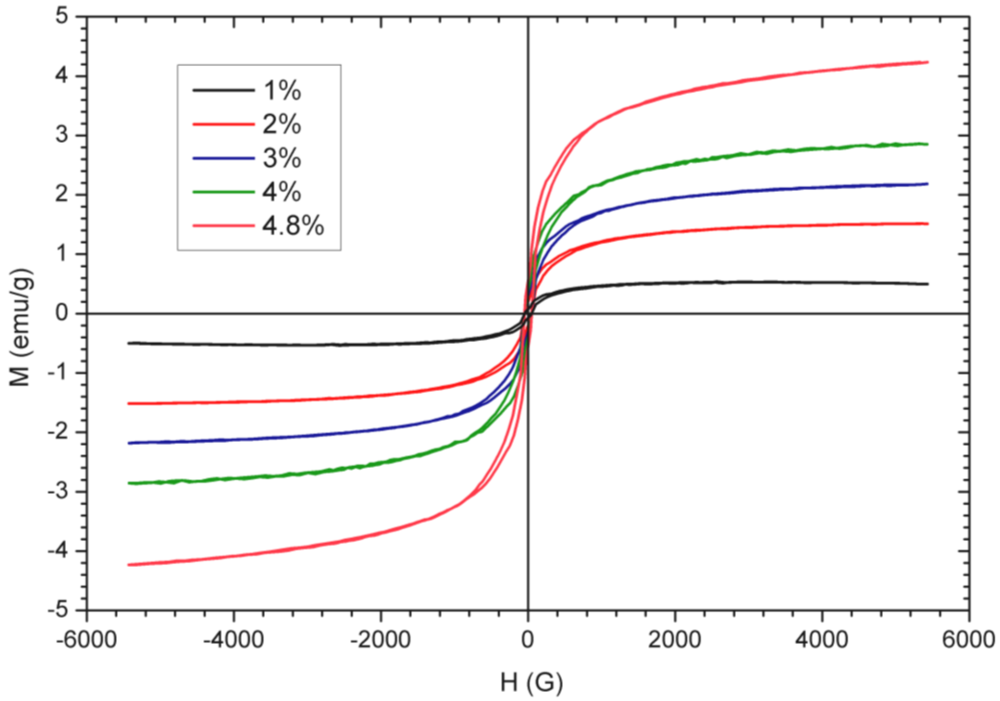

Figure 2.5 Magnetization curves of the Fe_3O_4-water magnetic nanofluid with respect to volumetric particle concentrations

The figure demonstrates that all of the Fe_3O_4-water samples reveals a superparamagnetic behavior. Theoretically, ferromagnetic materials with very small particle sizes in the nano-size level can behave as a superparamagnetic particle (Nguyen, 2012). As mentioned previously in Table 2.1, the Fe_3O_4 particles in the utilized samples have a particle size between 15-20 nm. It means that the size of our particles is under a critical value for the superparamagnetism limit. The superparamagnetic behavior of the magnetic nanofluid samples ensures that all particles are getting magnetized in the presence of the magnetic field. When the external magnetic field is removed, all particles are demagnetized, and there will be no remanence on them. This is a significant advantage for the magnetic nanofluid samples when they are used in various applications under the influence of the external magnetic field.

Figure 2.5 also indicates that the magnetization capability of the magnetic nanofluid samples increases with increasing nanoparticle concentration. This is an obvious result that the fluid becomes denser for higher particle concentration in terms of magnetic material content. After, 5000 G, it is obtained that the magnetization of the samples reaches a saturation limit which determines the saturation magnetization values of them. Figure 2.6 depicts that the saturation magnetization of the samples increases considerably with increasing magnetic nanoparticle concentration.

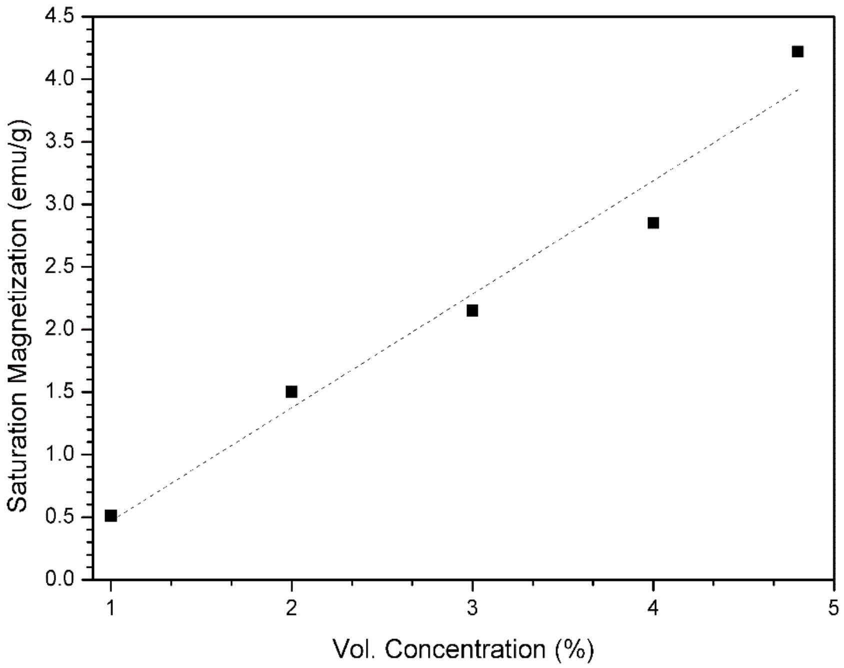

Figure 2.6 Saturation magnetization of the Fe_3O_4-water magnetic nanofluid with respect to volumetric particle concentrations

Magnetic susceptibility is a dimensionless parameter that specifies the relationship between the external magnetic field and the magnetization of the material. This relationship can be expressed as in Equation 2.2.

$$\mathbf{M} = \chi \mathbf{H} \tag{2.2}$$

As seen in Equation 2.2, the magnetic susceptibility value is actually equal to the slope of the linear part of the H-M curve. The determination of the magnetic susceptibility is important in the determination of the magnetic force acting on the magnetic nanofluid under the applied magnetic field, which is going to influence the magnetic nanofluid inside the valveless micropump. Therefore, magnetic susceptibility was calculated for all samples using H-M curves in Figure 2.5.

The output of the VSM device which was used in the measurement of magnetic properties is taken as magnetic field strength (G) on the x-axis and magnetization (emu/g) on the y-axis. In order to calculate the magnetic susceptibility, the unit must be the same on two axes. Hence, the density of the samples is needed for unit conversion. The density of the magnetic nanofluid samples can be calculated by the mixing formula given in Equation 2.3.

$$\rho_{\mathrm{mnf}} = (1-\varphi)\rho_{\mathrm{bf}} + \varphi\rho_{\mathrm{p}} \tag{2.3}$$

Here, φ is the volumetric concentration, ρ_{bf} and ρ_{p} are the density of the base fluid and the nanoparticles, respectively. The change in density of Fe_3O_4-water magnetic nanofluids, depending on the volume concentration is given in Figure 2.7. As expected, the density of the samples increases with the increase of the particle concentration added to the base fluid.

Figure 2.8 shows the linear region in the magnetization curve after the unit conversion of Fe_3O_4-water magnetic nanofluid samples has been completed. Magnetic susceptibility can be obtained by linear fitting in this region. The fitted lines are shown with dashed lines. The R^2 value, which indicates the regression reliability during line fitting, is ensured to be above 0.95 under all conditions. Then, the magnetic susceptibility values obtained as a result of the linear fitting are given in Figure 2.9. It was observed that the magnetic susceptibility of Fe_3O_4-water magnetic nanofluid samples increased with increasing volume concentration in a non-linear behavior.

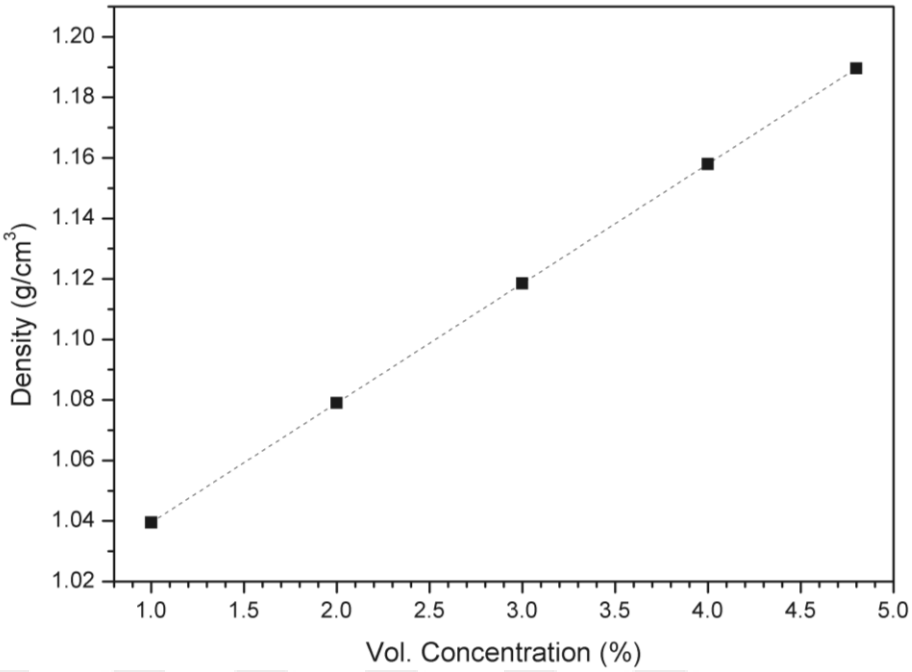

Figure 2.7 Density of the Fe_3O_4-water magnetic nanofluid with respect to volumetric particle concentrations

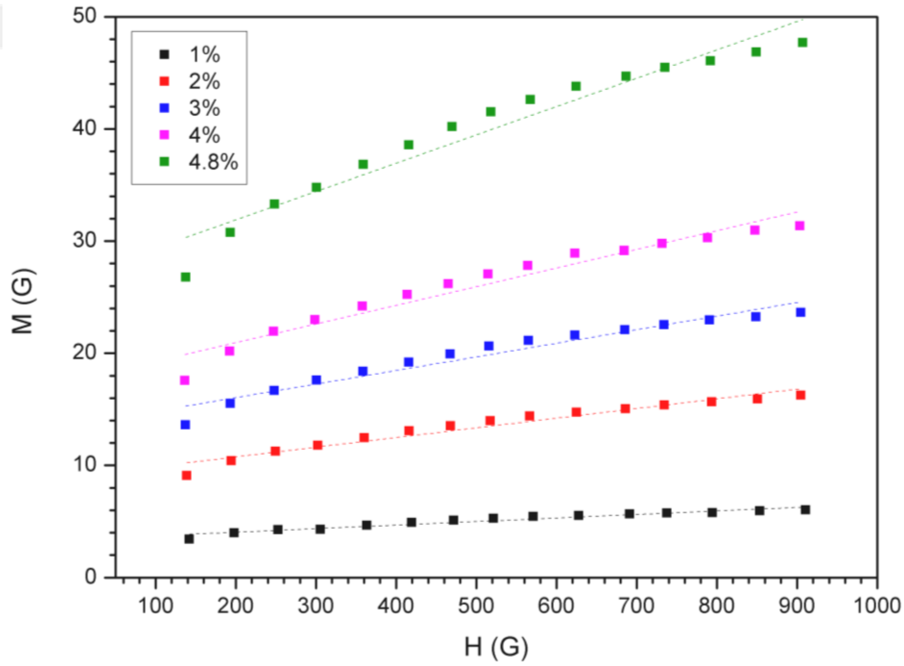

Figure 2.8 The linear region of H-M curves for Fe_3O_4-water magnetic nanofluid with respect to volumetric particle concentrations

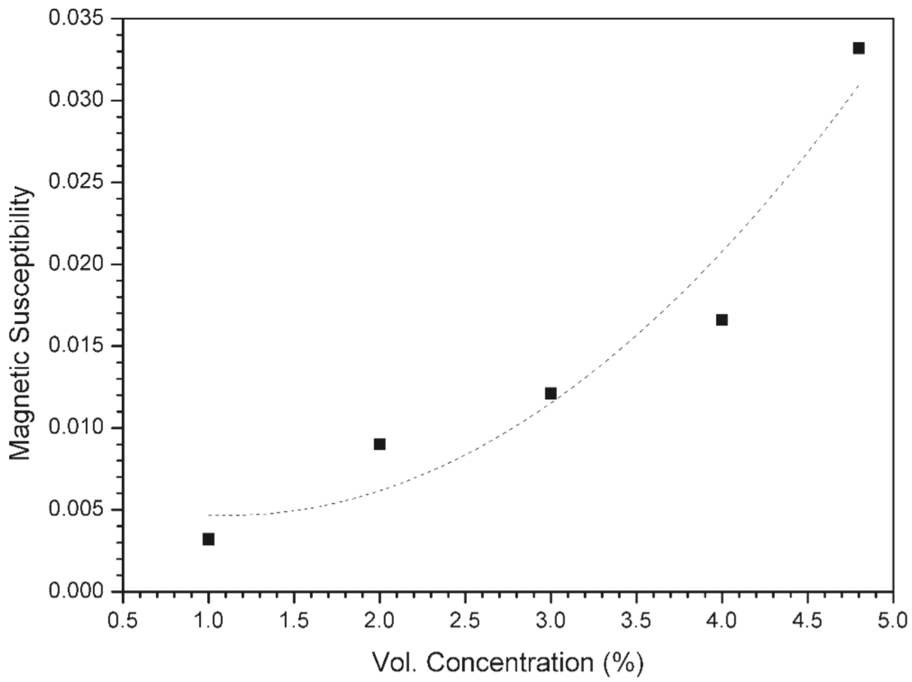

Figure 2.9 Magnetic susceptibility of the Fe_3O_4-water magnetic nanofluid with respect to volumetric particle concentrations

2.5 Thermal Conductivity

2.5.1 Measurement Method

The thermal conductivity of the Fe_3O_4-water magnetic nanofluid samples was measured with the 3ω method. The thermal conductivity measurements of the 3ω method are conducted by a stationary probe. It means that during the measurement there is not any external force acting on magnetic nanoparticles. This feature of the 3ω method can be taken into advantage while studying with magnetic nanofluids. If an external magnetic field is applied to the magnetic nanofluid during the measurements, there can be a magnetic force acting on magnetic nanoparticles. In that case, we can assume that the magnetic force is the only force on nanoparticles. Therefore, by evaluating the thermal conductivity measurement results while external magnetic field acts on the sample, the behavior of the magnetic nanoparticles in the suspension can be interpreted. For this purpose, the thermal conductivity was measured for different concentrations of 1, 2, 3, 4 and 4.8 vol. % in the absence and presence of the magnetic field. Also, measuring the thermal conductivity both in the absence and presence of the external magnetic field provides insight about whether the valveless micropump working with magnetic nanofluid can be a good candidate for thermal management systems with tunable thermal conductivity or not.

A schematic of the 3ω setup with permanent magnets is shown in Figure 2.10. The 3ω method was first presented by Cahill (1990). Constitutively, a sinusoidal current is applied on a linear wire heater at an angular frequency ω, generating an oscillating heat source at 2ω, which depends on the thermal properties of the heater and its surroundings. This oscillation in the corresponding temperature triggers the heater resistance at 3ω, which leads to a voltage signal at 3ω. In other words, the term depending on 3ω is generated by nonlinear mixing of the applied AC current at ω with the electrical resistance change at 3ω. By varying the configuration of the wire and its surrounding, the method has been used to measure the thermal conductivity of samples, including nanofluids (Koca, Doganay & Turgut, 2017; Turgut et al., 2008).

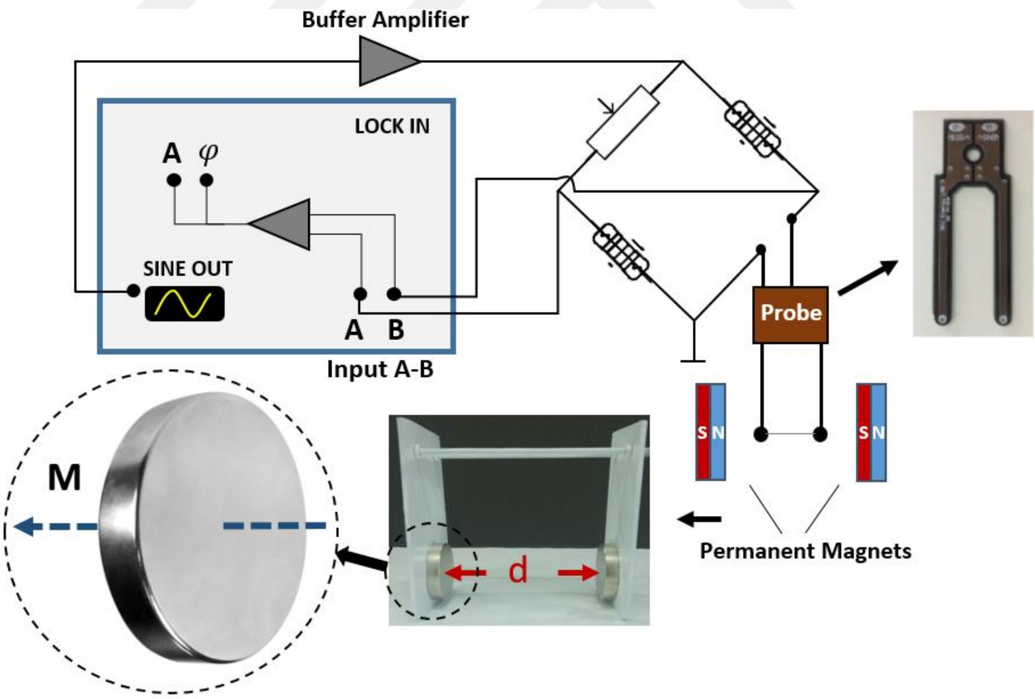

Figure 2.10 Schematic of 3ω setup with permanent magnets

In order to generate a magnetic field, permanent magnets were used. Permanent magnets may provide almost uniform or non-uniform magnetic flux density without requiring any continuous expenditure of energy (Coey, 2002). They are also able to produce high magnitude magnetic fields in small volumes. Neodymium-Iron-Boron (NdFeB) magnets are selected as permanent magnets since they are one of the strongest permanent magnets commercially available (Rollat, Guyonnet, Planchon & Tuduri, 2016). A simple magnet holder design was used for applying the magnetic field to the magnetic nanofluid sample between 0-400 G (the magnetic field strength value at the center of measurement vessel) in parallel and perpendicular directions to the temperature gradient generated by the thermal conductivity measurement probe. The magnetic field strength was controlled by changing the distance between magnets. A non-magnetic distance holder was used in order to keep the distance constant. The generated magnetic field was measured by PCE-MFM 3000 Gaussmeter. The accuracy of the gaussmeter is ±5% in the range of 0-3000 G.

2.5.2 Results and Discussions on Thermal Conductivity

As mentioned previously, the magnetic field generated by permanent magnets can be almost uniform or non-uniform. In order to understand the influence of the magnetic field on the thermal conductivity, the uniformity of the external magnetic field was investigated. Figure 2.11 depicts the front view of the thermal conductivity measurement region.

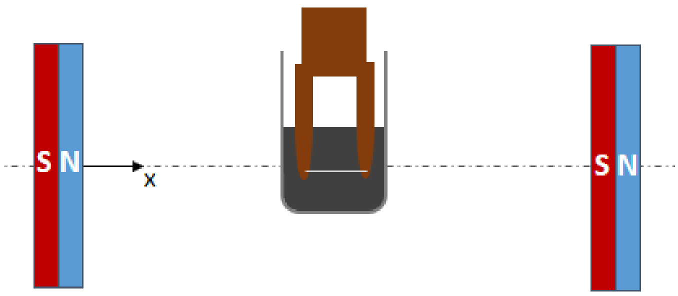

Figure 2.11 Schematic of the front view of the measurement region

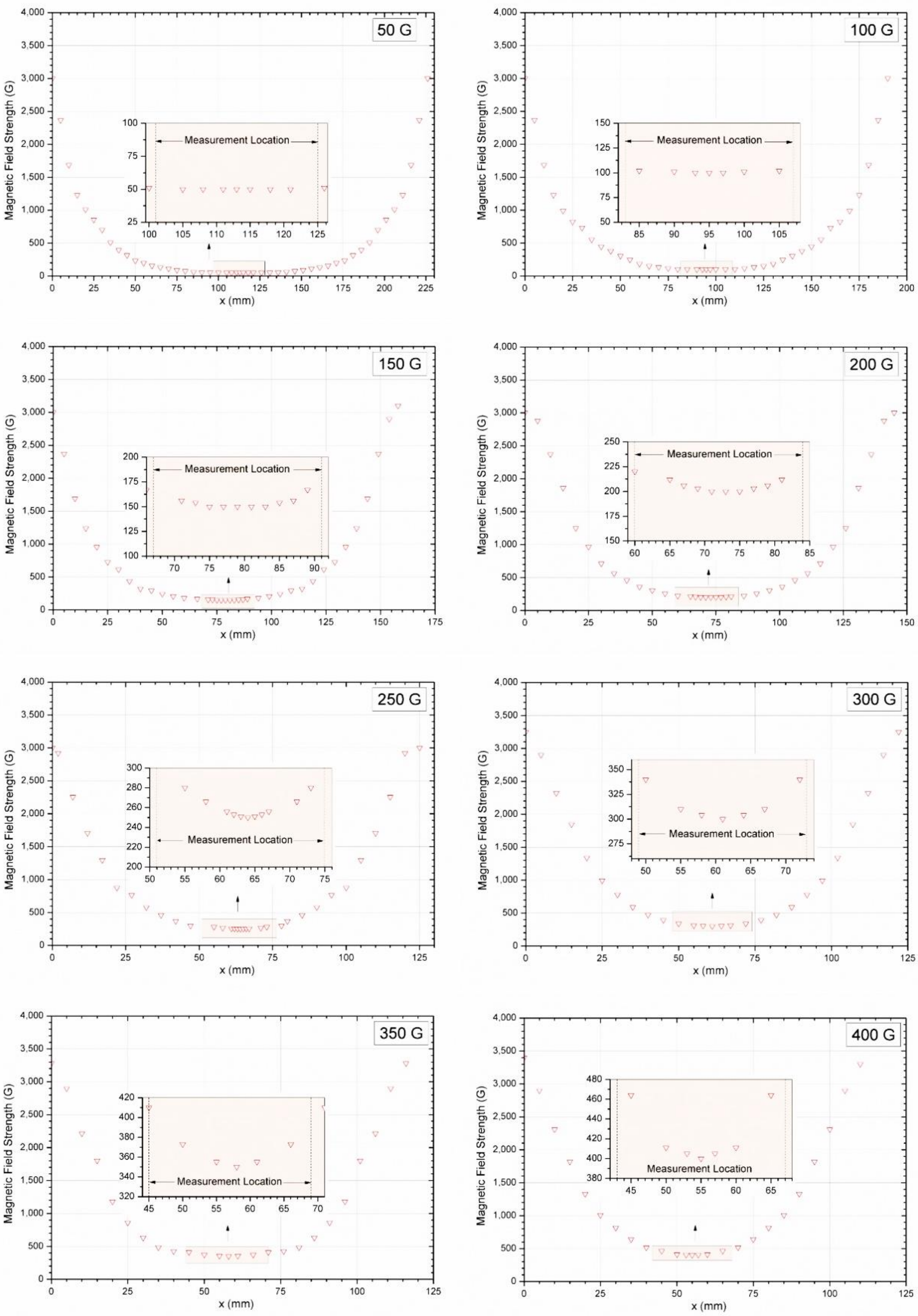

Figure 2.12 Magnetic field strength variation in the air gap between permanent magnets

In the experimental analysis, the magnetic field strength was measured between permanent magnets in the x-direction. The thermal conductivity measurements were conducted for eight different magnetic field strength values (50-400 G) in the middle point of the center axis of the permanent magnets. Figure 2.12 demonstrates the magnetic field strength values in the air gap between permanent magnets for eight cases. As seen from the figure, the magnetic field strength in the air gap increases while the magnets are getting closer to each other. During the thermal conductivity measurements, the samples were kept in a vessel with a 24 mm diameter. The vessel was located in the middle of the air gap between permanent magnets. The detailed views in each graph in Figure 2.12 focuses on the distribution in the measurement location. The dashed lines in the detailed views specify the vessel borders. It is clearly understood from Figure 2.12 that the magnetic field strength in the vessel location is getting more non-uniform for higher magnetic field strength values.

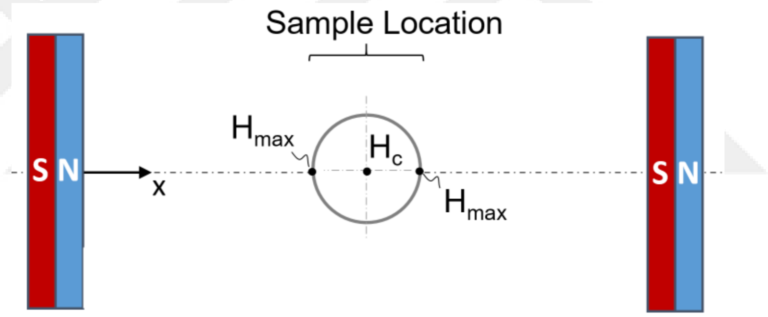

Figure 2.13 Schematic of the top view of the measurement location

Figure 2.13 depicts the top view of the vessel in the air gap between permanent magnets. H_c is the center magnetic strength value on the vessel and it was altered between in the specified range above with 50 G intervals. H_{max} is the maximum magnetic field strength in the measurement region. In respect to the H_c values for eight cases, H_{max} values varied which correspond to the magnetic field strength values on the borders of the vessel in the x-direction.

In order to investigate the influence of non-uniformity of the applied magnetic field on the thermal conductivity of the Fe_3O_4-water magnetic nanofluid samples a non-uniformity factor was defined as:

$$\eta = \frac{H_{\max} - H_c}{H_c} \tag{2.4}$$

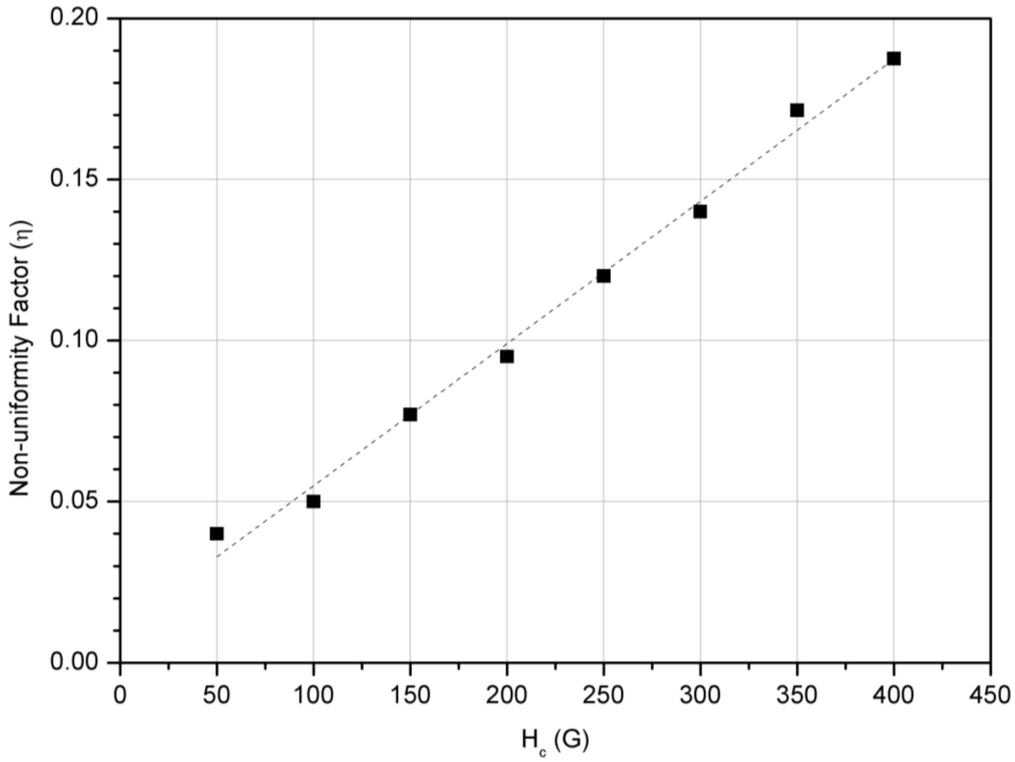

Figure 2.14 Non-uniformity factor for different H_c values

The non-uniformity factor represents the ratio of the difference between maximum magnetic field strength and the targeted magnetic field strength in the vessel center and the targeted magnetic field strength in the vessel center. In other words, if the magnetic field strength value in the vessel center and border are the same, the non-uniformity factor value is zero and so the measurement region is in totally uniform magnetic field influence. Figure 2.14 indicates the calculated non-uniformity factor values with respect to the H_c values. It is clearly seen that the non-uniformity factor is increases with increasing H_c values. This is another proof that the magnetic field strength in the measurement location becomes more non-uniform for higher H_c values. The factor is very close to the zero for H_c values of 50 and 100 G, which can be considered almost uniform while it increases to 0.19 for maximum H_c values of 400 G which means the flux density becomes very non-uniform.

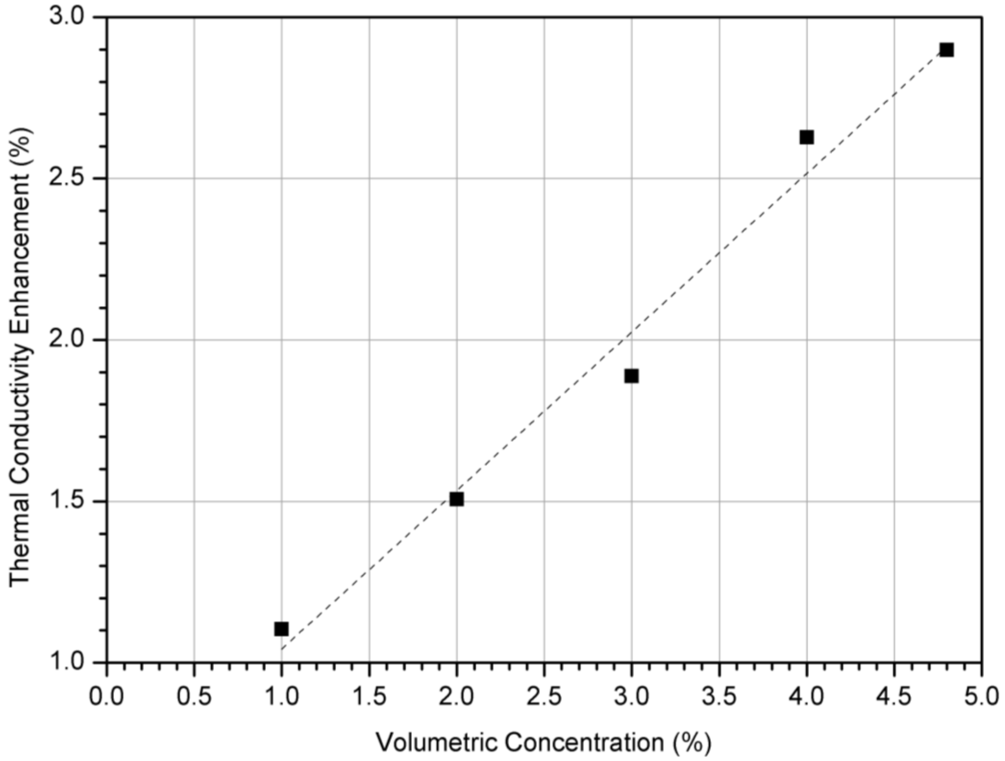

Figure 2.15 Thermal conductivity enhancement with respect to volumetric particle concentration in the absence of the magnetic field

The thermal conductivity of the Fe_3O_4-water samples was first measured in the absence of the external magnetic field. It is observed that the addition of the nanoparticles influences thermal conductivity. Figure 2.15 shows that thermal conductivity enhances with increasing volumetric concentration. The enhancement is about 0.1% for 1 vol. % concentration which can be considered as almost no enhancement while it is about 2.9% for maximum particle concentration.

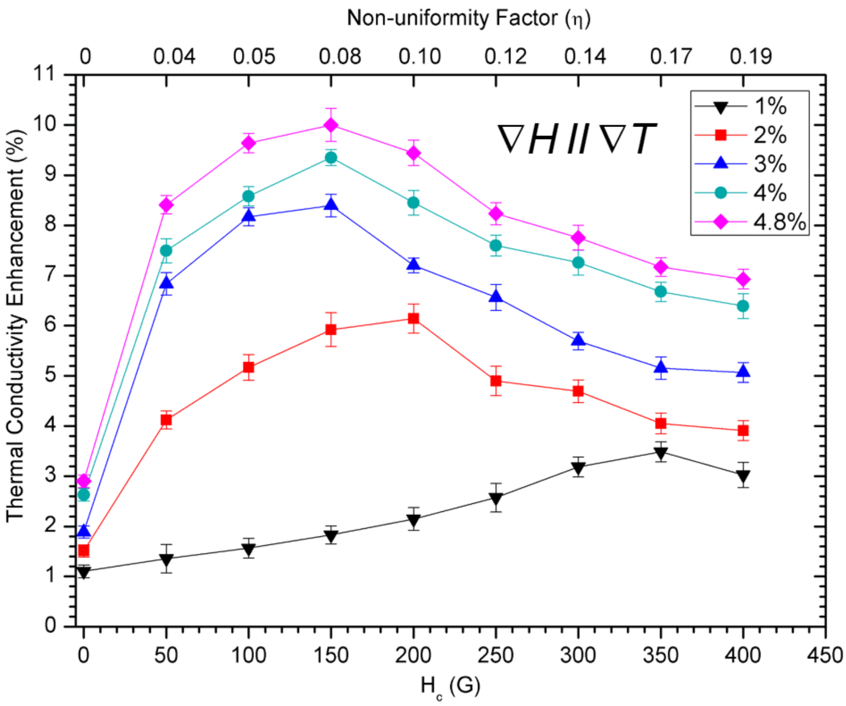

Figure 2.16 Thermal conductivity enhancement with respect to volumetric particle concentration in the presence of an external magnetic field parallel to the temperature gradient

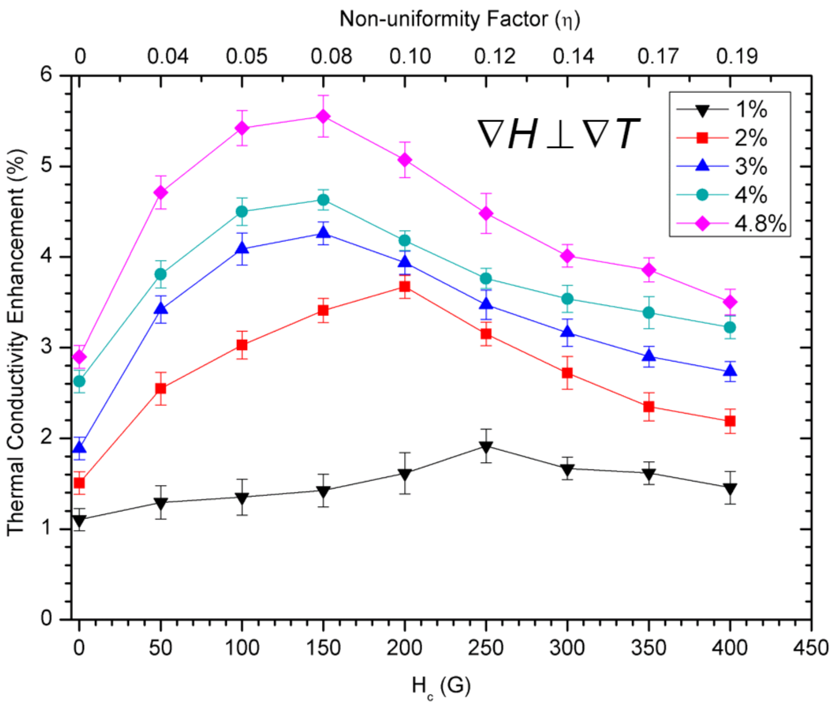

Figure 2.17 Thermal conductivity enhancement with respect to volumetric particle concentration in the presence of an external magnetic field perpendicular to the temperature gradient

Figure 2.16 and Figure 2.17 indicate the variation of thermal conductivity enhancement in Fe_3O_4-water magnetic nanofluid with the application of the external magnetic field in both parallel and perpendicular orientation, respectively. It seems that there is modest thermal conductivity enhancement with the application of an external magnetic field. The physical reason behind this phenomenon can be explained by the chain aggregation formation of the magnetic nanoparticles under the influence of an external magnetic field. Each magnetic nanoparticle in a magnetic nanofluid is considered as a single domain particle with the magnetic moment of **m**. In the absence of the external magnetic field, the nanoparticles are scattered and the direction of the magnetic moments of these particles are oriented randomly. The magnetic dipole-dipole interaction between a pair of magnetic nanoparticles can be expressed by (Mendelev & Ivanov, 2004):

$$U_d\left(ij\right) = -\left[3\frac{\left(\mathbf{m}_i.\mathbf{r}_{ij}\right)\left(\mathbf{m}_j.\mathbf{r}_{ij}\right)}{r_{ij}^5} - \frac{\left(\mathbf{m}_i - \mathbf{m}_j\right)}{r_{ij}^3}\right] \tag{2.5}$$

where,

$$\mathbf{r}_{ij} = \mathbf{r}_i - \mathbf{r}_j \tag{2.6}$$

$U_d\,(ij)$ is the magnetic dipole-dipole interaction between two nanoparticles, $\mathbf{r}_{ij}$ is the distance between i^{th} and j^{th} nanoparticles, $\mathbf{m}_i$ and $\mathbf{m}_j$ are the magnetic moments of the i^{th} and j^{th} nanoparticles, respectively. If the dipolar energy between magnetic nanoparticles gets sufficiently strong, the chain aggregation formation occurs (Shima et al., 2009). This interaction between the particles can be measured by a dipolar coupling constant:

$$\lambda = \frac{m^2}{d^3 k_B T} \tag{2.7}$$

Here, m^2/d^3 is the interaction energy between two particles, and k_BT is the thermal energy where d is the particle diameter, k_B is the Boltzmann constant and T is the temperature. The chain-like structure occurred due to the dipolar energy becomes longer with the higher external magnetic field.

Figure 2.16 and Figure 2.17 also reveal that the thermal conductivity of Fe_3O_4-water samples indicates a sudden increment with the application of the external magnetic field apart from 1vol. % concentrated sample. The increment continues until 150 G for 3, 4, and 4.8 vol. % concentration, 200 G for 2 vol. % concentration and 350 G in parallel and 250 G in perpendicular for 1% vol. concentration. Then, the thermal conductivity enhancement begins to decrease. The reason behind that is the increment in the non-uniformity factor, which means that the non-uniformity of the applied magnetic field is increasing. In the non-uniform magnetic field, there will be a force acting on the magnetic nanoparticles as (Pamme, 2006),

$$\mathbf{F_m} = \frac{Q\,\Delta\chi}{\mu_0}\left(\mathbf{B}\cdot\nabla\right)\mathbf{B} \tag{2.8}$$

where the magnetic flux density $\mathbf{B} = \mu_0\left(1+\chi\right)\mathbf{H}$, Q is the magnetizable volume (m^3), $\Delta\chi$ is the susceptibility difference between particles and base fluid, μ_0 is the permeability of free space, **H** is the external magnetic field strength (T). When the force generated overcomes the static drag force between the magnetic nanoparticle and the fluid, the particles move, and the chain aggregation formation becomes breaking. This phenomenon can be simply depicted for our measurements, as sketched in Figure 2.18. In the absence of the external magnetic field, nanoparticles are randomly dispersed in the fluid. In the case of almost uniform external magnetic field application, the nanoparticles align in the direction of the field by forming in a chainlike structure. For these cases, we observed that the magnetic nanofluid in the vessel has a flat surface appearance. If the external magnetic field becomes non-uniform, the nanoparticles feel a force generated due to the magnetic field gradient. This leads the nanoparticles to move toward the vessel wall gradually according to the magnitude of the generated force. Moreover, we observed a curved surface look in this case.

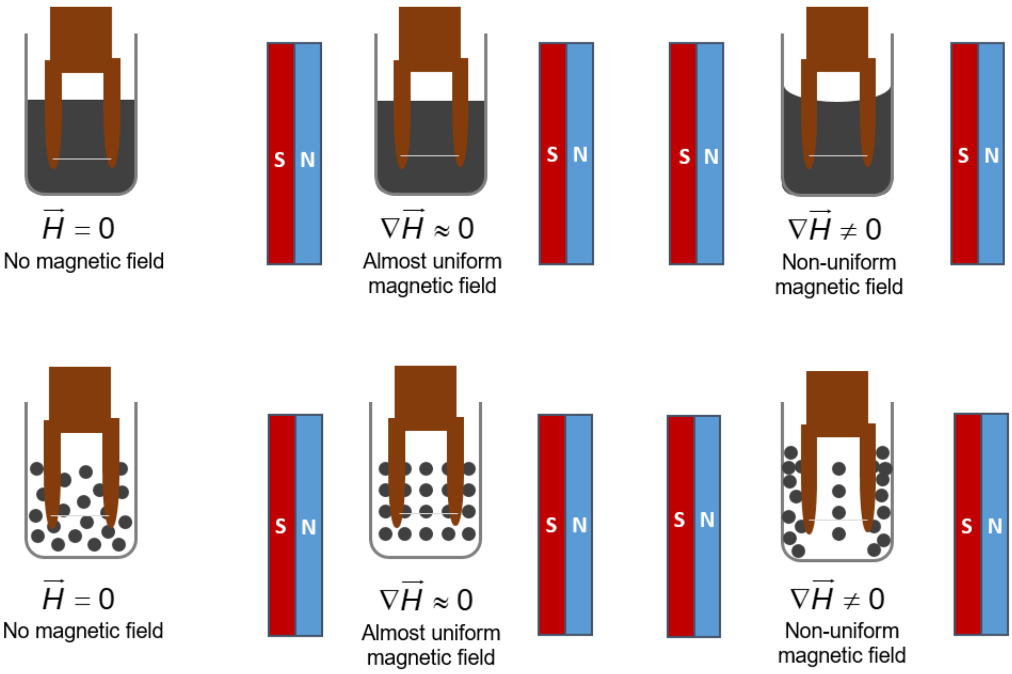

Figure 2.18 Magnetic nanofluid sample behavior under the influence of external magnetic field

In order to have a better understanding of the influence of the non-uniformity factor, the additional axis was added to the top of Figure 2.16 and Figure 2.17. The influence of the non-uniformity factor on the thermal conductivity enhancement varies with respect to particle concentration. For instance, the non-uniformity factor of 0.08 provides the maximum value of the thermal conductivity enhancement for 3, 4 and 4.8 vol. concentration while it is 0.1 for 2 vol. % and 0.17 in parallel and 0.12 in perpendicular for 1 vol. % concentration, respectively. In other words, the non-uniformity factor has a more significant effect on higher concentrated samples. This may be due to the increment in the ratio of the immigrated magnetic nanoparticles towards the vessel wall with the increasing particle concentration.

It is also observed that the thermal conductivity enhancement is more significant with the parallel orientation. The thermal conductivity has increased up to 10% with parallel orientation and up to 5.6% with perpendicular orientation for the volumetric concentration of 4.8%. The reason behind the influence of the external magnetic field direction can be explained by analyzing thermal resistances (Mousavi & Kumar, 2018). As mentioned before, when the external magnetic field is applied, the magnetic nanoparticles will be aligned in the field direction. If the temperature gradient is in the parallel direction to this field, the heat will flow through both aligned chains and the fluid gap between them simultaneously. However, when the temperature gradient is in the perpendicular direction to the field, the heat will flow through aligned chains and the fluid gap in series. The thermal resistance can be expressed as shown in Figure 2.19 for both cases. It is evident that the equal thermal resistance in parallel orientation is lower than the perpendicular orientation. Therefore, the thermal conductivity enhancement is more significant for parallel orientation.

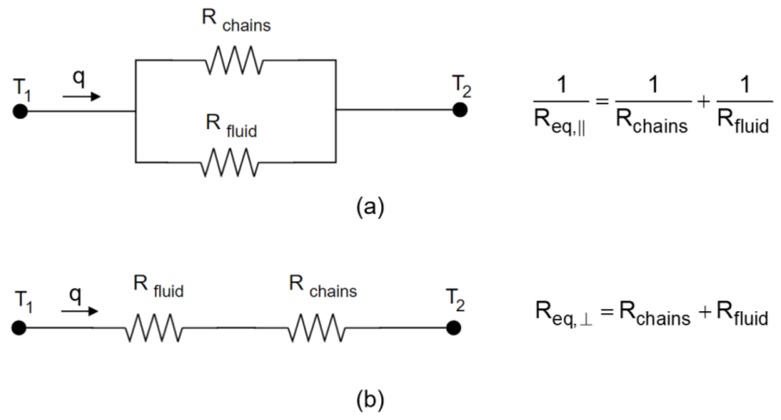

Figure 2.19 Thermal resistance calculations for (a) parallel and (b) perpendicular orientations

CHAPTER THREE
DESIGN AND STRUCTURE OF VALVELESS MICROPUMP

3.1 Introduction

This chapter includes the operation principle and structure of the valveless micropump with respect to design parameters. The valveless micropump consists of a microchannel unit, a permanent magnetic actuator (PMA), and a control unit. The microchannel unit was designed to contain the Fe_3O_4-water magnetic nanofluid which will be transported during the pumping operation. PMA was used to generate a magnetic field gradient which results in a magnetic force on the magnetic nanofluid. The control unit was employed to provide the desired signal to alter the angular speed of the PMA for the pumping process.

3.2 Operation Principle

One of the initial requirements for a valveless micropump process is a contactless power source. In this point of view, magnetic actuation appears as a good candidate for the pumping of magnetic nanofluids. Basically, the magnetic actuation for the magnetic nanofluids can be implemented with two methods: *(i)* permanent magnets *(Passive method)*, or *(ii)* current-carrying coils *(Active method)* (Niarchos 2003). Both methods have different pros and cons, depending on the application. The main advantage of the active method is the possibility to control the magnetic field intensity by just adjusting the applied current. However, in some cases, integration of the active method with miniaturized systems becomes a challenging issue, since the large dimensions of the system components (Wang & Yuan, 2008). In addition to installation drawbacks, a vast amount of heat is generated by the current-carrying coil during the operation. The heat that is dissipated from the coil may cause a remarkable temperature increment in the magnetic material and influence its magnetic and thermal properties. Permanent magnets, on the other hand, have various advantages over the active method in magnetic actuation, even though the controllability of the magnetic field strength is not as simple as in active methods.

Permanent magnets are easy to use and provide a high magnetic field intensity without requiring large spaces and causing minimal heat generation (Ahn, Oh & Choi, 2003). They are non-uniform magnetic field sources without requiring a continuous expenditure of energy. When a rapid spatial change in the magnetic field is demanded, they are very favorable to utilize (Coey, 2002). Therefore, the actuation of magnetic nanofluids by permanent magnets in small channels can be considered as effective, advantageous, and promising for micropumping applications (Yamahata & Gijs, 2004).

The magnetic force density can be calculated from the magnetic energy density (e_m) in the absence of the electric current and electric field (Nguyen, 2012).

$$\mathbf{F_m} = -\nabla e_m \tag{3.1}$$

$$-\nabla e_m = -\nabla \mathbf{M}\cdot\mathbf{B} = \mathbf{M} \times (\nabla \times \mathbf{B}) + \mathbf{B} \times (\nabla \times \mathbf{M}) + (\mathbf{M}\cdot\nabla)\mathbf{B} + (\mathbf{B}\cdot\nabla)\mathbf{M} \tag{3.2}$$

One should note that according to the Ampere's Law, the first two terms on the right-hand side, i.e., $(\nabla \times \mathbf{B}) = 0$ and $(\nabla \times \mathbf{M}) = 0$ are omitted in the absence of an electric field. Hence, the magnetic force density becomes,

$$\mathbf{F_m} = (\mathbf{M}\cdot\nabla)\mathbf{B} + (\mathbf{B}\cdot\nabla)\mathbf{M} \tag{3.3}$$

If the magnetic medium is homogenous, there will be no magnetization gradient. Therefore, the magnetic force that is acting on a medium is defined regarding the magnetic field gradient as follows (Weston, Gerner & Fritsch, 2010),

$$\mathbf{F_m} = (\mathbf{M}\cdot\nabla)\mathbf{B} \tag{3.4}$$

If an appropriate magnetic field gradient can be created along the channel or tube, the magnetic force can be utilized for magnetic nanofluids (Hejazian, Li & Nguyen, 2015). The permanent magnets should possess either a rotary or reciprocal motion to make them turn back to their initial positions for continuous operation. In such a way, the pumping effect inside flow channels could be achieved. One of the main challenging issues to maintain a continuous fluid flow is the perpetual existence of the magnetic field during the return motion. In the case of the reciprocal motion, the permanent magnets move along the flow direction and then return to the initial position by using the same path to complete the cycle. In the first stage of the cycle, the magnetic force acts along the flow direction. However, when the direction of the magnets is inverted, bidirectional forces are observed. Irregular force interactions inside the magnetic fluid cause fluctuations and prevent the continuous fluid flow along a particular path. In order to resolve this problem, a semicircular microchannel-based rotating PMA was proposed for the current valveless micropump (Figure 3.1a).

The proposed actuator design consists of a semicircular microchannel and two pairs of permanent magnets. Each permanent magnet pair was formed of two cylindrical magnets which are placed side-by-side with a reversed magnetization direction. Each pair was located under the semicircular microchannel to generate a magnetic field gradient along the arc segment of the circular path (Figure 3.1b). The arc segment under the influence of the permanent magnet pair should be steered along the circular path by a rotor-like structure to create a magnetic actuation on the magnetic nanofluid. Using two pairs of permanent magnets which are placed under the semicircular microchannel with 180° apart provides a continuous magnetic actuation. The magnetic nanofluid moves towards the closest permanent magnet under the effect of the magnetic field. Hence, a small amount of magnetic nanofluid is confined within a pair of magnets inside an arc length of $r\theta$. The continuous rotary motion of the rotor-like structure sweeps the magnetic nanofluid, which is confined within magnet pairs along the semicircular channel. After a magnet pair completes the half-turn, the second pair starts acting on semicircular microchannel to maintain continuous actuation. The tangential component of magnetic force that is acting on the semicircular microchannel is critical as it drives the fluid motion and directly controls the flow rate of magnetic nanofluid. The tangential component the magnetic force occurs due to the spatial distribution of magnetic flux density within the flow channel and which heavily depends on the angular interval between each member of magnet pairs, i.e., $\Delta\theta$. Therefore, a parametric study is going to be carried out in the next chapter to reveal the relationship between the angular interval between each member of magnet pairs, $\Delta\theta$, and the magnetic flux density along the tangential direction.

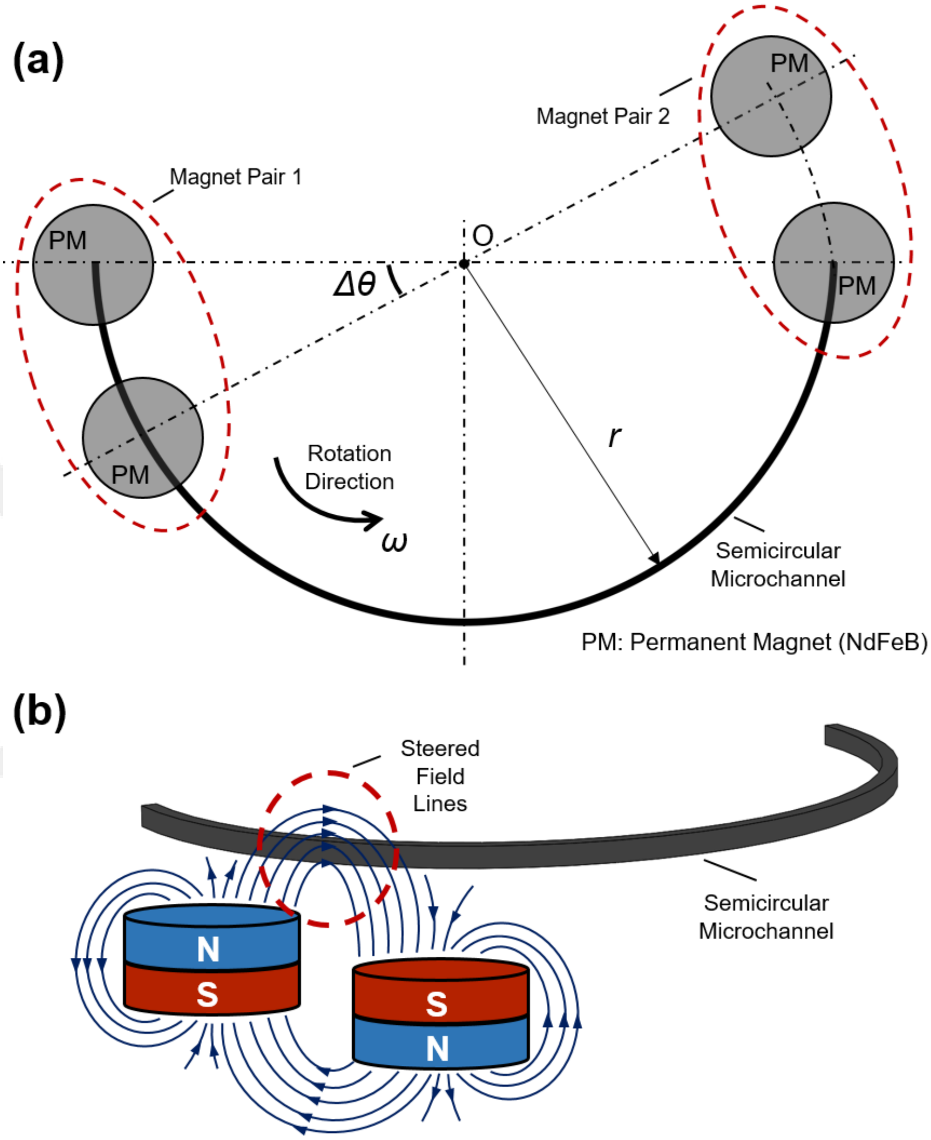

Figure 3.1 (a) Geometry of the PMA based semicircular microchannel (top view), (b) The principle of directing the magnetic field lines on the semicircular microchannel

3.3 Structure of the Valveless Micropump

The valveless micropump was designed according to the operation principle of PMA provided in the previous section. Figure 3.2 indicates the digital rendering for the solid model of the valveless micropump.

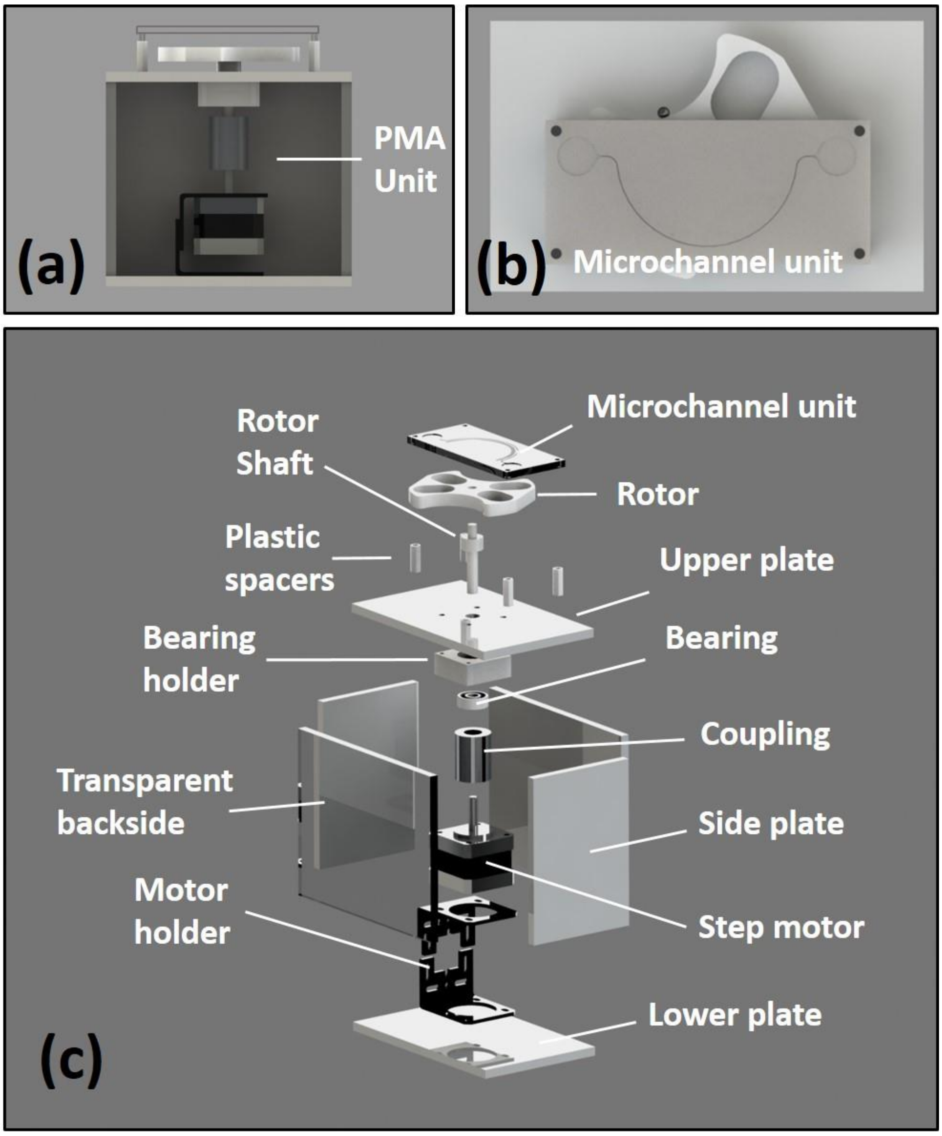

Figure 3.2 (a) Side view of the valveless micropump, (b) Top view of the valveless micropump, (c) Exploded view of valveless micropump

The designed valveless micropump has two main parts. The first one is the PMA unit which consists of a rotor and a rotor shaft, plastic spacers, upper, lower and side plates, a bearing and a bearing holder, a coupling, a step motor and two step motor holders. The other one is a microchannel unit which includes a semicircular microchannel with two reservoirs for the inlet and outlet of the magnetic nanofluid. Details with the microchannel unit will be provided in the following chapter. To achieve a better visual design, apart from the rotor, all components of the PMA unit is kept in an enclosed volume. The enclosed volume is created by poly (methyl methacrylate) (PMMA) plates. The backside plate is designed as a transparent wall in order to visualize the inside of this enclosed volume. The assembly drawing for the valveless micropump is provided in Appendix 2.

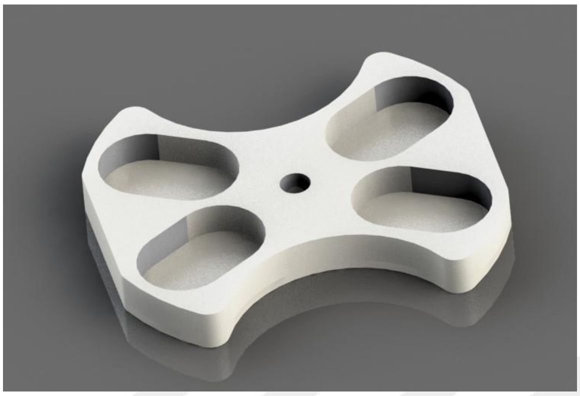

Figure 3.3 Structure of the rotor

Figure 3.3 shows the rotor structure. It has four slots to hold the cylindrical permanent magnets. The slotted structure is preferred for adjusting the distance of magnets from the center of the rotor when it is necessary. To manufacture a lighter rotor, the four corners are designed with chamfers and two arc-shaped blocks are subtracted from two sides. The angular interval $\Delta\theta$ between magnet slots is given randomwise for the solid model presented in Figure 3.3. The exact value of the angular interval $\Delta\theta$ will be determined in the following chapter.

Figure 3.4 A single aluminum motor holder

The rotor was determined to be rotated by a step motor (Nema 14) for achieving a precise speed control. In the present structure of valveless micropump the motor should be located in the vertical position, as shown in Figure 3.2a. In order to hold the motor in the vertical position, two ready to use aluminum motor holders are selected and placed. Figure 3.4 indicates a single motor holder and the dimensions of the motor holder are given in Appendix 3.

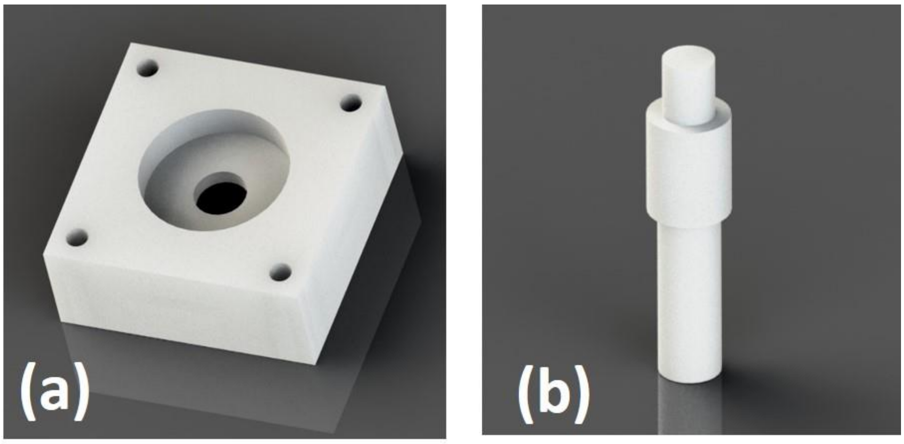

Figure 3.5 (a) Bearing holder, (b) Plastic stepped rotor shaft

In order to couple the motor shaft with the rotor, a coupling, a ceramic ball bearing, a bearing holder (Figure 3.5a) and a plastic stepped rotor shaft (Figure 3.5b) were utilized. Coupling is selected for reducing the plastic stepped shaft diameter of 6 mm to a motor shaft diameter of 5 mm. The ceramic bearing (606) with the dimensions of 6×117×16 mm is placed in a bearing holder. The dimensions of the bearing holder and plastic stepped shaft is provided in Appendix 4 and 5. After coupling the motor shaft and the rotor, to produce an enclosed volume, plastic plates are mounted to two sides, upper, lower, front, and backward.

CHAPTER FOUR
MAGNETIC NANOFLUID FLOW

4.1 Introduction

This chapter begins with a set of numerical study with two different purposes, i.e., *(i)* determining an optimal $\Delta\theta$ value for magnet pairs, and *(ii)* investigating the magnetic nanofluid flow at the specified $\Delta\theta$ value while the permanent magnets are stationary. Next, the experimental setup was built with the specified $\Delta\theta$ value. In order to test the capability of the setup, preliminary experiments were conducted for stationary magnet configuration. Finally, the magnetic nanofluid flow inside the semicircular microchannel is experimentally studied at various angular speeds of PMA for performance tests of the valveless micropump.

4.2 Numerical Study
4.2.1 Numerical Model

A 3D numerical model was developed in COMSOL Multiphysics to simulate the interaction between the magnetic actuator and the magnetic nanofluid. The numerical study is divided into two parts. In the first part, the magnetic flux density variations inside the microchannel are evaluated to determine the effect of the angular interval between magnets, i.e., $\Delta\theta$. In the second part, on the other hand, the magnetic flux density analysis was coupled with the magnetic nanofluid flow problem in a semicircular microchannel, and the fluid velocity was examined for a specific alignment of permanent magnets, i.e., for a certain $\Delta\theta$, by varying the volumetric concentration of magnetic nanofluid.

The magnetic flux density simulations were conducted at five different angular intervals of $\Delta\theta$ = 35°, 45°, 60°, 75°, and 90°. The magnetic flux density caused by permanent magnets in the microchannel region is determined by Gauss' Law for magnetism,

$$\nabla \cdot \left(\mu_0 \mu_r \mathbf{H} + \mathbf{B_r} \right) = 0 \tag{4.1}$$

where μ_0 is the permeability of the free space, μ_r is the relative permeability of the permanent magnets, and $\mathbf{B_r}$ is the remanence of the permanent magnets. Equation (4.1) is solved for the external magnetic field (**H**) which depends on magnetic scalar potential (V_m) as,

$$\mathbf{H} = -\nabla V_m \tag{4.2}$$

The steady-state analysis of the magnetic nanofluid flow in the semicircular microchannel was conducted by coupling the laminar flow problem with magnetic flux density analyses in COMSOL Multiphysics. In the case of well suspended superparamagnetic particles in the carrying fluid, the entire magnetic nanofluid is considered as a homogenous medium (Nguyen, 2012). Therefore, the magnetic nanofluid flow can be governed by the Navier-Stokes equations with continuum approximation (Banerjee et al., 2017) for continuity and momentum, respectively.

$$\nabla \cdot \mathbf{u} = 0 \tag{4.3}$$

$$\rho \left(\mathbf{u} \cdot \nabla \right) \mathbf{u} = -\nabla p + \nabla \cdot \left[\mu \left(\nabla \mathbf{u} + \nabla \mathbf{u}^T \right) \right] + \mathbf{F}_b \tag{4.4}$$

where ρ, u, p, μ, and $\mathbf{F_b}$ are density, velocity vector, pressure, the viscosity of the magnetic nanofluid and the body force, respectively. For the current problem, the only body force, i.e., $\mathbf{F_b}$, is the magnetic force per unit volume ($\mathbf{F_m}^{'''}$). The magnetic force that is acting on magnetic nanofluid can be evaluated from the magnetic field distribution as previously presented in Chapter 2, with Equation 2.8 (Pamme, 2006).

In the computational model, four NdFeB permanent magnets and the semicircular microchannel geometry is placed inside an air domain (Figure 4.1a). The cubic air domain has an edge length of 100 mm. In the magnetic flux density analysis, the guess value of the magnetic scalar potential (V_m) was assumed as zero. The magnitude of the remanence of the permanent magnets ($\mathbf{B_r}$) was considered as 1.32 T. For the laminar flow analysis, magnetic flux density (**B**) obtained from the magnetic flux density analysis was integrated into the flow module for the calculation of the body force arising from Equation 2.8. The magnetic susceptibility and the viscosity of the magnetic nanofluid samples were exploited from the experimentally determined results in Chapter 2.

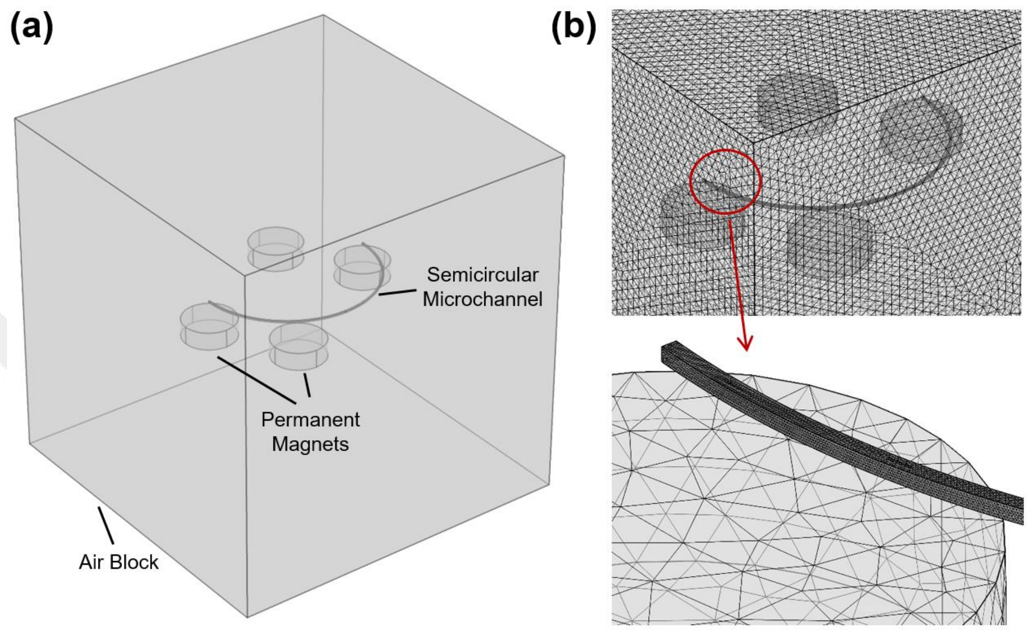

Figure 4.1 (a) The isometric view of the cubic air block, permanent magnets, and semicircular microchannel assembly, (b) The view of mesh intensity depending on the domains

The flow condition was assumed as single-phase laminar, and the working fluid is incompressible. The boundary conditions were defined as no-slip on the walls and atmospheric pressure at the inlet and outlet sections of the channel. The free tetrahedral mesh structure was generated within the air domain, and quadrilateral elements are used inside the microchannel domain. As seen in Figure 4.1b, fine mesh structure is defined within the channel to capture the high spatial gradients.

Five different mesh intensities of 12756 (M1), 52337 (M2), 270617 (M3), 3569815 (M4), and 6233996 (M5) are generated to ensure that the results are independent of the number of mesh. Figure 4.2 depicts the magnetic density variations along the semicircular channel with five different mesh intensities. Even though a similar tendency is observed for each mesh configuration, there occur some deviations, especially regions near the inversion points. At lower mesh intensities, i.e., M1, M2, and M3, fluctuations are observed with a maximum mean absolute difference of 1.6%. The fluctuations are suppressed by increasing the mesh intensity. At higher mesh intensities, i.e., M4 and M5, there is no remarkable difference, and the mean absolute difference is 0.0019%. M4 was selected for the numerical analyses in order to save the computational time.

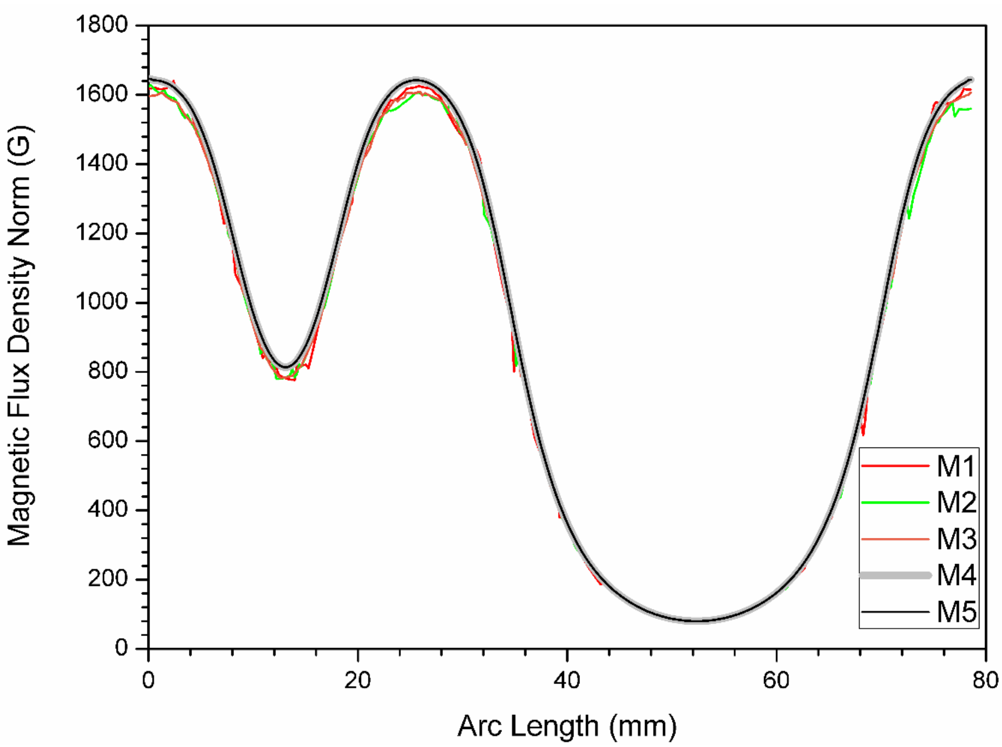

Figure 4.2 The influence of mesh intensity on the magnetic flux density variation along the semicircular channel

4.2.2 Verification of the Model

Before going through the numerical simulations of the present work, the numerical effort of Ozbey, Karimzadehkhouei, Yalcin, Gozuacik & Kosar (2015) is reproduced for the model verification.

An identical model is developed regarding the geometrical parameters, material properties, and mesh configurations that are provided in the reference work. For the verification, the magnetic flux density distribution obtained at a 0° rotor angle position was considered. The variations of x-component of magnetic flux density along the channel length are compared with the reference work in Figure 4.3. The results indicate that there is a good agreement between the current results and the reference work. The mean absolute error is less than 4.5%.

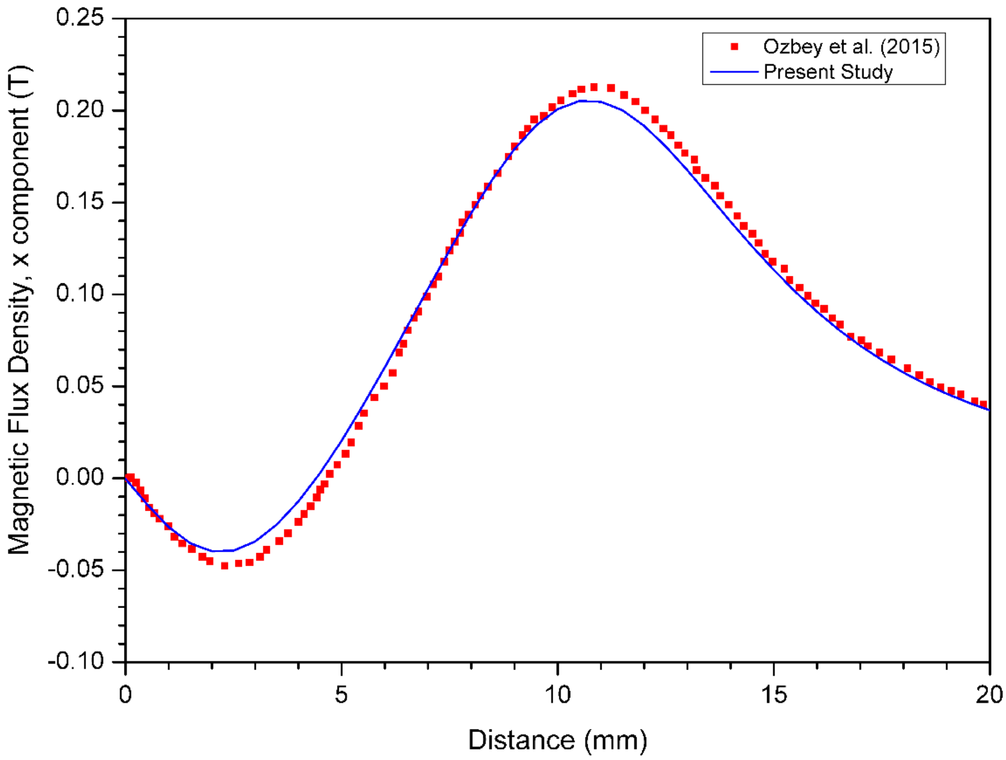

Figure 4.3 Comparison between the present study and the reference work of Ozbey et al. (2015)

4.2.3 Numerical Results and Discussions

As discussed previously, the angular interval ($\Delta\theta$) between permanent magnets of each pair has a significant role in the magnetic field gradient obtained in the microchannel region. For determining the appropriate magnet configuration to achieve more efficient actuator, the angular interval between magnets, i.e., $\Delta\theta$, was altered as 35°, 45°, 60°, 75°, and 90° in the magnetic flux density simulations. The spatial distributions of tangential (B_t) and the normal (B_n) components of magnetic flux density (Figure 4.4) influence the driving force for the magnetic nanofluid and undesired interactions with walls, respectively.

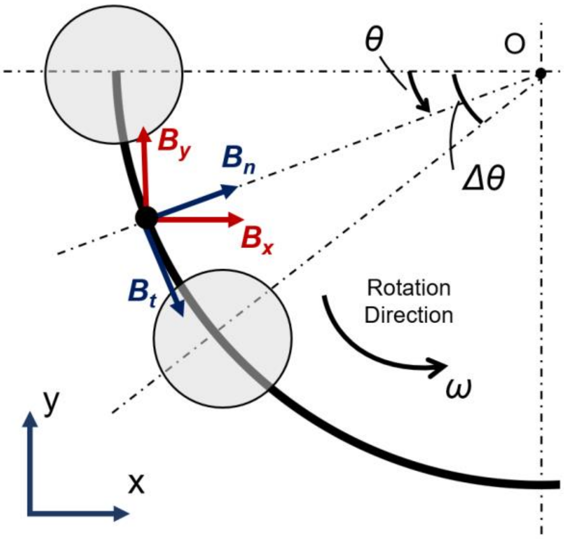

Figure 4.4 Schematic for the determination of the tangential and normal components of the magnetic flux density

For an arbitrary point on the central axis of the semicircular channel, the magnitudes of tangential and the normal components of the magnetic flux density can be calculated as

$$B_t = B_x \sin\theta - B_y \cos\theta \tag{4.5}$$

$$B_n = B_x \cos\theta + B_y \sin\theta \tag{4.6}$$

This study concerns the combined effect of the magnets, the positive component of B_t between the magnets for the $\Delta\theta$ = 35°, 45°, 60°, 75°, and 90° have been presented in Figure 4.5.

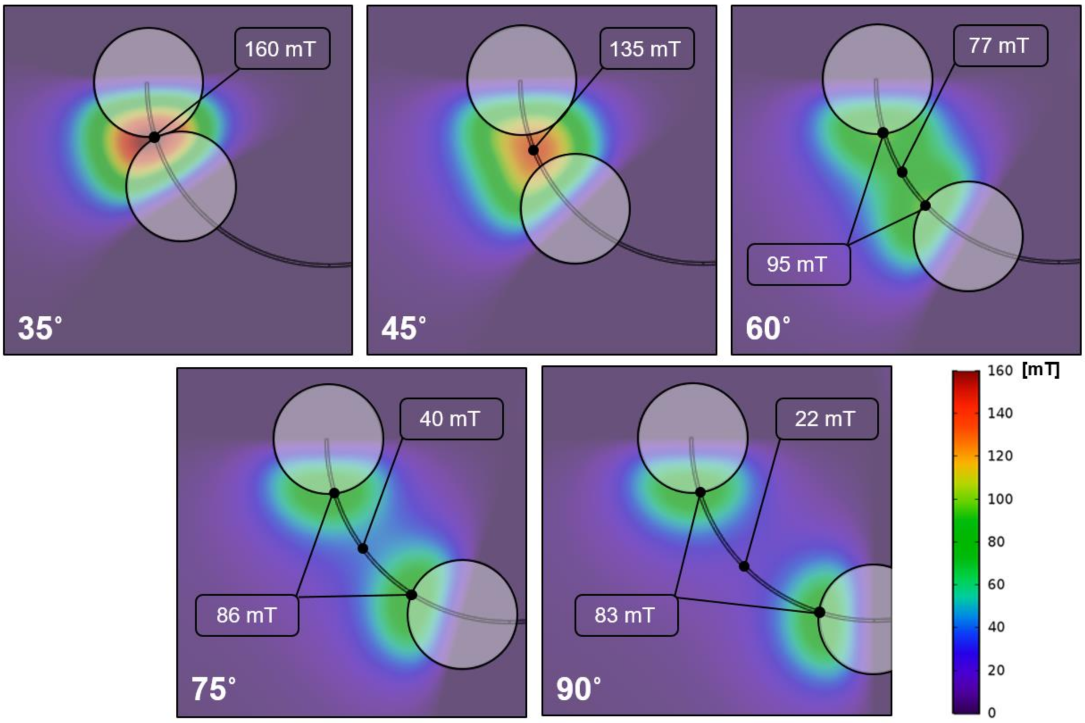

Figure 4.5 Magnetic flux density distribution for different angular intervals (Δθ)

Due to the symmetry of the permanent magnet pairs, the distribution of the tangential component of the magnetic flux density was only provided for one pair. It is obvious that the magnitude of the magnetic flux density between magnets decreases with increasing the angular interval ($\Delta\theta$). The maximum field strength appears in the middle of the magnets for $\Delta\theta$ = 35°, and 45° as 160 mT and 135 mT, respectively. However, the maximum values for $\Delta\theta$ = 60°, 75°, and 90° are obtained at two symmetrical points close to each magnet as 95 mT, 86 mT, and 83 mT, respectively. For the minimum possible angular interval, i.e., $\Delta\theta$ = 35°, the magnetic field arising from each magnet is observed as a combined region between magnets. The unified region gets wider as $\Delta\theta$ increases from 35° to 75°. For the angular intervals larger than 75°, the magnetic field of each magnet is observed as almost two separate regions. More specifically, the maximum field strength changes about 14.4% when $\Delta\theta$ is increased from 60° to 90°. However, the value in the middle of the magnets changes about 250% which means that the combined effect of the magnets drastically decreases.

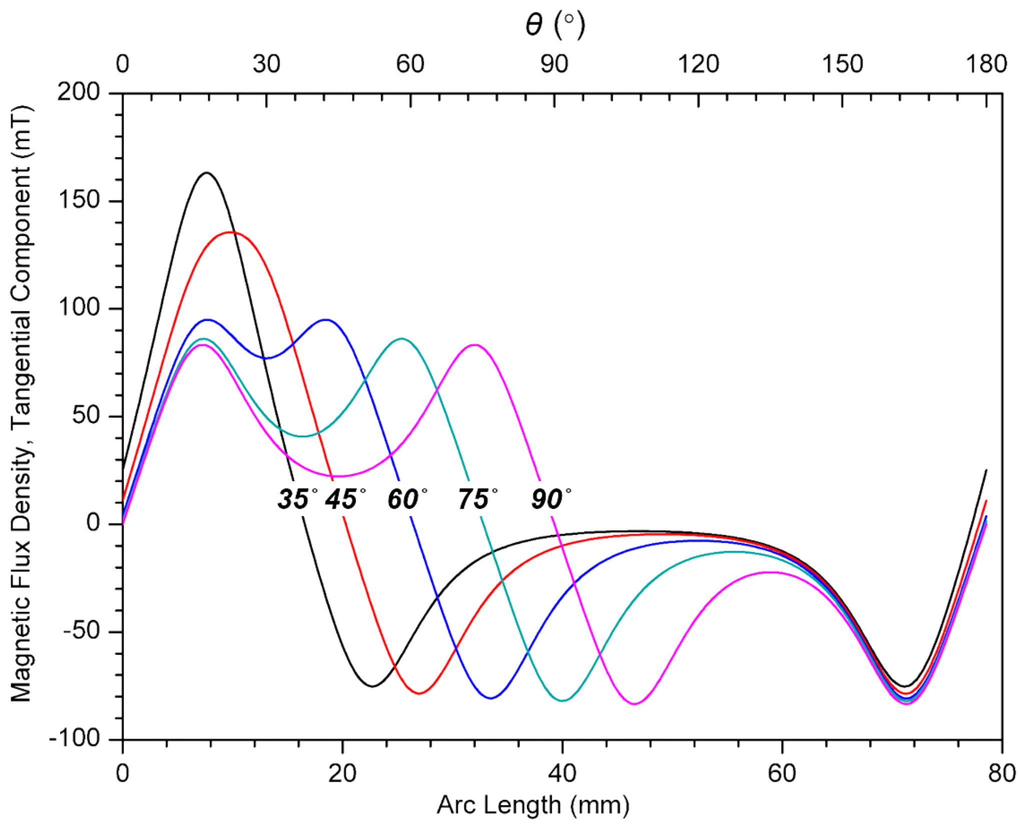

Figure 4.6 Variation of the tangential component of the magnetic flux density in the centerline of the semicircular microchannel

In Figure 4.6, the tangential component of the magnetic flux density on the centerline of the semicircular microchannel is provided for five different angular positions of the magnets. The magnetic flux density variations have positive peaks for 35° and 45° configurations in the middle of the active magnet pairs (the pair on the semicircular channel). Beyond these peaks, the magnetic flux density gradually reduces, and negative peaks are observed at 17.5° and 22.5° for 35° and 45° configurations, respectively. The magnetic flux density curves have inflection points around 135°. The magnetic flux densities are almost zero at this specific point at the left-hand side of the passive pair (the pair leaving the semicircular channel), then additional negative peaks are observed. For the configurations with angular intervals of 60°, 75°, and 90°, two discrete positive peaks are observed. B_t distribution between magnets expands to a larger area with two peaks, and beyond the second peak, the variations are similar to the narrow configurations.

Before going through the flow simulations, it is aimed to determine the angular distance between magnets to define the rotor structure of the actuator. For this purpose, three evaluation parameters were considered as form factor (*FF*) (Equation 4.7) (Vasilescu, 2006), crest factor (*CF*) (Equation 4.8) (Wagner et al., 1993) and B_n/B_t ratio.

$$FF = \frac{B_{rms}}{B_{avg}} \tag{4.7}$$

$$CF = \frac{B_{peak}}{B_{avg}} \tag{4.8}$$

The form factor (*FF*) and crest factor (*CF*) are parameters that are used in the signal analysis to represent characteristics of transient variables. In this study, on the other hand, they are used for evaluating spatial distributions of the magnetic field. These non-dimensional performance indicators were calculated from the magnetic flux density variations along the centerline of the semicircular microchannel. The evaluation parameters for different angular intervals are presented in Table 4.1.

Table 4.1 The performance indicators for different angular intervals of magnets

Performance Indicator	**35°**	**45°**	**60°**	**75°**	**90°**
Form Factor	0.634	0.918	1.062	1.096	1.114
Crest Factor	2.714	2.305	1.594	1.658	1.579
B_n/B_t	0.028	0.005	0.103	0.121	0.162

The form factor is the ratio between RMS and average of the magnetic flux density values. It represents the measure of how effectively the generated magnetic flux density distributed along the centerline. For better performance, the form factor should be close to unity. Hence, $\Delta\theta$ = 45, 60, and 75° are highlighted in Table 4.1 to indicate that considering the form factor, these configurations look promising. The crest factor is the fraction of the peak value of the magnetic flux density to the average value. One can infer that this is the opposite of the form factor and the measure of "non-uniformity" of the magnetic flux density distribution. It is aimed to obtain the most uniform distribution, to provide a consistent flow field between the magnets. That is, the *CF* value should be the lowest in the best configuration. Similar configurations are highlighted in Table 4.1 as the promising ones when the crest factor is considered. As the third performance measure, B_n/B_t is taken into account for minimizing frictional effects arising from the magnetic field. The tangential component should be higher to ensure the dominance of the driving force along the flow path. That is, the lowest value of B_n/B_t is the most appropriate configuration. $\Delta\theta$ = 35, 45, and 60° are highlighted in Table 4.1 to indicate that the tangential component is dominant in these configurations. Three performance measures should be taken into account to end up with an overall evaluation. Consequently, $\Delta\theta$ = 60° is found to be the most appropriate design. In the rest of the analyses, the selected configuration is implemented.

In order to investigate the flow characteristics of magnetic nanofluids inside the semicircular microchannel, parametric analyses were conducted for three different volumetric concentrations of magnetic nanofluids with 1, 2, and 3% at a specific angular interval of $\Delta\theta$=60°. In the current analyses, the semicircular microchannel was assumed to be entirely filled by magnetic nanofluids.

Before analyzing the magnetic nanofluid flow inside the semicircular microchannel, the tangential component of the magnetic force is determined. The tangential magnetic force can be evaluated as:

$$F_t = F_x \sin\theta - F_y \cos\theta \tag{4.9}$$

where F_x and F_y are the *x*- and *y*- components of the magnetic force. As mentioned previously, the magnetic force acting on the magnetic nanofluids can be evaluated by Equation 2.8. The equation can be written for *x*- and *y*- components as follows:

$$F_x = \frac{Q\,\Delta\chi}{\mu_0}\left(B_x \frac{\partial B_x}{\partial x} + B_y \frac{\partial B_x}{\partial y} + B_z \frac{\partial B_x}{\partial z} \right) \tag{4.10}$$

$$F_y = \frac{Q\,\Delta\chi}{\mu_0}\left(B_x \frac{\partial B_y}{\partial x} + B_y \frac{\partial B_y}{\partial y} + B_z \frac{\partial B_y}{\partial z} \right) \tag{4.11}$$

The tangential magnetic force per unit volume on magnetic nanofluid samples when the permanent magnets are in the initial position is presented in Figure 4.7. It is seen from the figure that the magnetic nanofluid sample tends to move the closest magnet. Moreover, the magnitude of the magnetic force per unit volume is significantly increased with increasing particle concentration, due to the increase in magnetization capability.

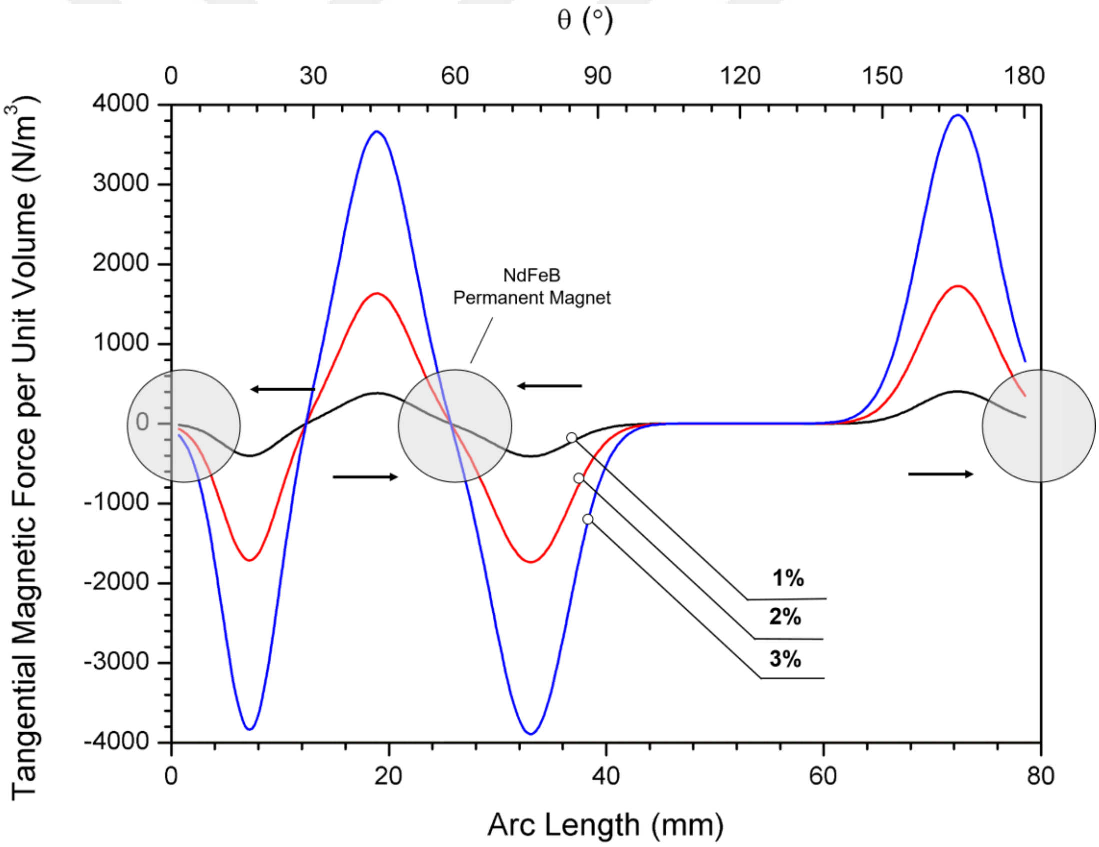

Figure 4.7 The influence of concentration of the magnetic nanofluids on the variation of the tangential component of the magnetic force along the semicircular channel

The velocity fields that are obtained from the simulations are also reduced into the tangential velocity component. Following expression is implemented to determine the tangential component of the fluid velocity using the same vector analysis as in Figure 4.4,

$$V_t = u_x \sin\theta - u_y \cos\theta \tag{4.12}$$

where u_x and u_y are the *x*- and *y*- components of the velocity vector, respectively.

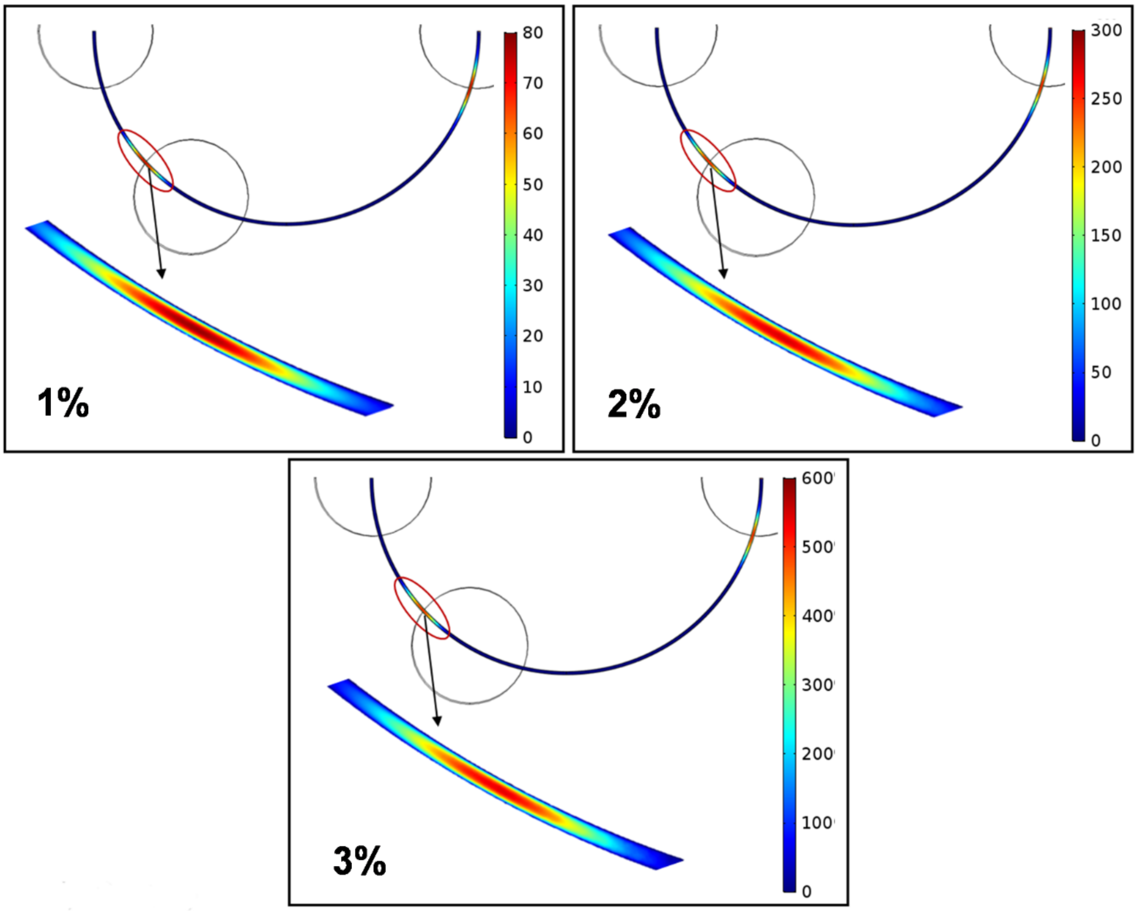

Figure 4.8 The influence of concentration of the magnetic nanofluids on the tangential velocity distributions inside the semicircular microchannel in µm/s

Figure 4.8 depicts the distribution of the tangential component of the magnetic nanofluid velocity in a semicircular microchannel for magnetic nanofluids with three different concentrations. For the sake of simplicity, only the flow distribution along the positive direction is provided in the figure. The tangential velocity variations have similar characteristics for each working fluids. Due to the viscous boundary layer adjacent to walls, the velocity magnitude is lower near the microchannel walls, and it increases through the centerline. Besides, the magnitude of the tangential velocity remarkably increases with increasing particle concentration. The present velocity distribution resembles the velocity field obtained by a similar study by Ozbey et al. (2015).

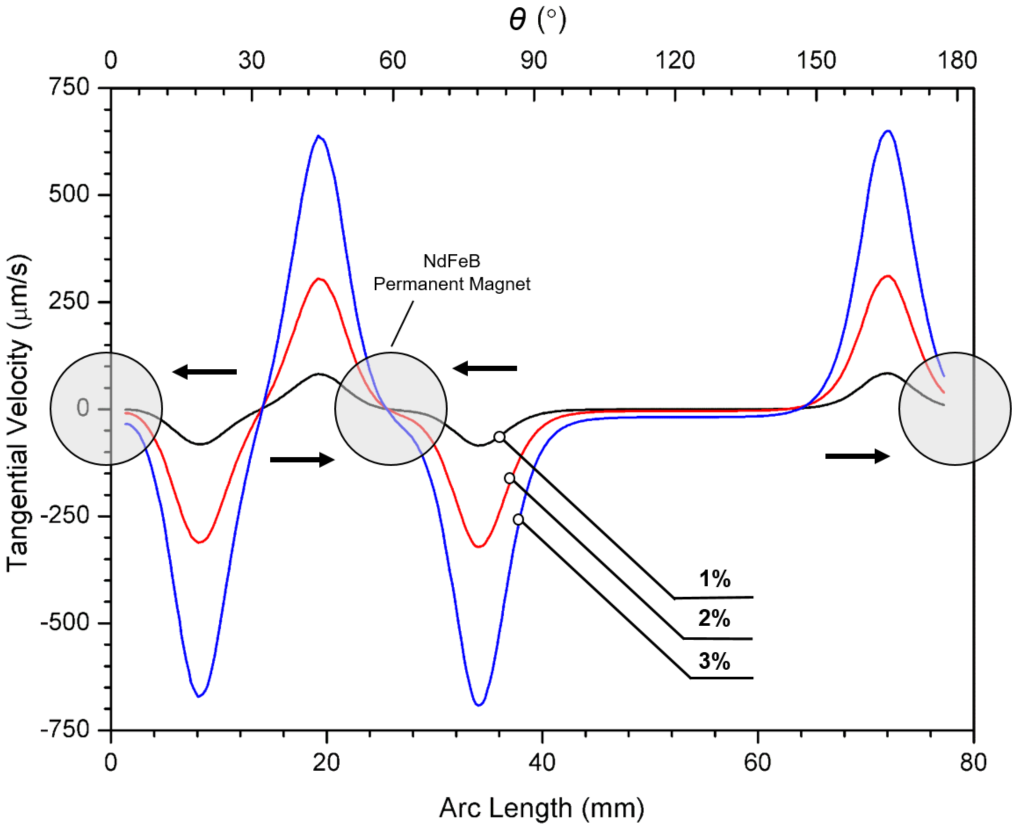

Figure 4.9 The influence of concentration of the magnetic nanofluids on the variation of the tangential component of the magnetic nanofluid velocity along the semicircular channel

In Figure 4.9, the tangential component of the magnetic nanofluid velocity distribution inside semicircular microchannel is given for a particular permanent magnet arrangement. The permanent magnets are at their initial positions, and they are stationary. A schematic representation of the permanent magnets is provided in the figure to illustrate the positions of the magnets. The shaded circles indicate the position of the permanent magnets, and the black arrows show the flow direction. The tangential velocity of the magnetic nanofluids increases with increasing magnetic nanoparticle concentration. Moreover, magnetic nanofluids tend to move towards to center of the closest permanent magnet due to the magnetic field gradients, as expected.

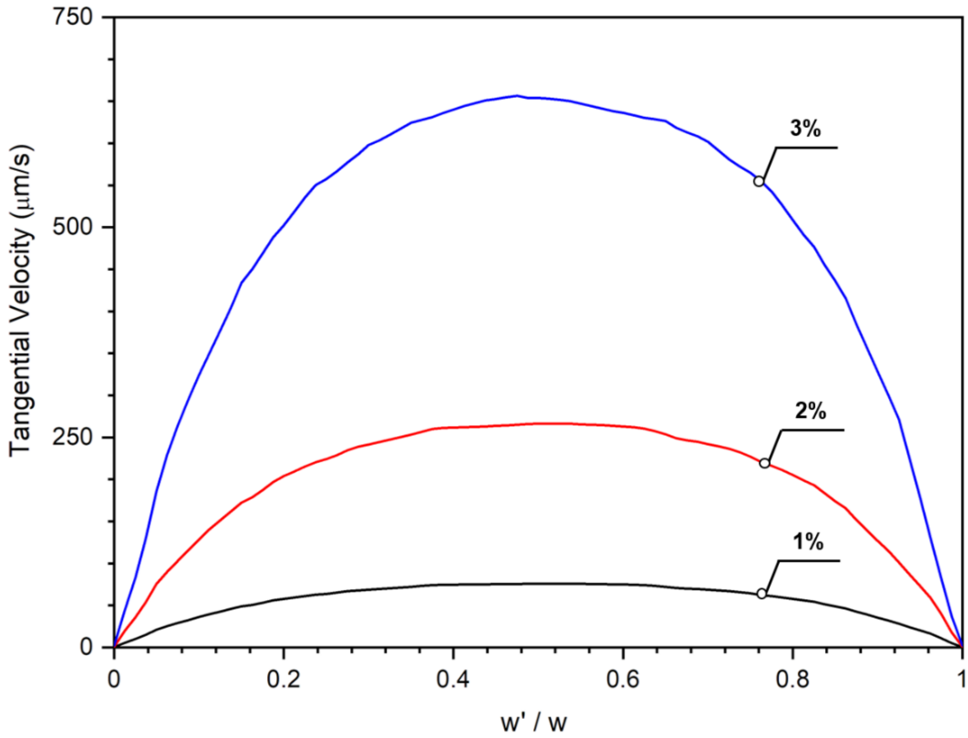

Figure 4.10 Variation of the tangential component of the magnetic nanofluid velocity in the cross-section

The velocity distribution in the cross-section for the positive part near the permanents ($\theta \approx 45°$) is also demonstrated in Figure 4.10. In the figure, w' is the position in the radial direction which varies between inner and outer walls (between 0 – 400 μm) of the microchannel. It is seen that the velocity is zero at boundaries and it increases through the center. Also, the velocity increases with increasing magnetic particle concentration.

4.3 Experimental Study

The experimental study includes two folds. The experiments were carried out with stationary and rotary permanent magnets. The former one is conducted to validate the numerical analyses, and the latter one is conducted to evaluate the performance of the proposed PMA.

4.3.1 Experimental Setup

The schematic representation of the experimental setup is given in Figure 4.10a. The setup consists of a PMA assembly, a semicircular microchannel unit, a control unit, and a digital camera (Figure 4.11b).

Mainly, the PMA assembly comprises a step motor, a rotor, four permanent magnets mounted on the rotor, machine elements, and other necessary parts for assembly (provided in the previous chapter). Bipolar Nema 14 step motor was selected for the rotating motion that needs to be transmitted to the rotor. The motor operates at 10 V with 1 kg.cm holding torque. It has 200 steps for a full revolution, which corresponds to 1.8° for each step. The motor shaft is 5 mm, and dimensions of the motor are 35×35×28 mm.

The rotor that was made of polyoxymethylene (POM) has four slots in order to hold permanent magnets. It was fabricated by a high precision cutting tool with a CNC milling machine (TMW-1050, Tongtai, Taiwan). Details of the structure of the rotor were mentioned in the previous chapter and the technical drawing for rotor is provided in Appendix 6. The cylindrical NdFeB permanent magnets have D_m = 15 mm diameter and t = 5 mm thickness. The distance between the center of the rotor, and each magnet was fixed to the r = 25 mm (Figure 4.11c).

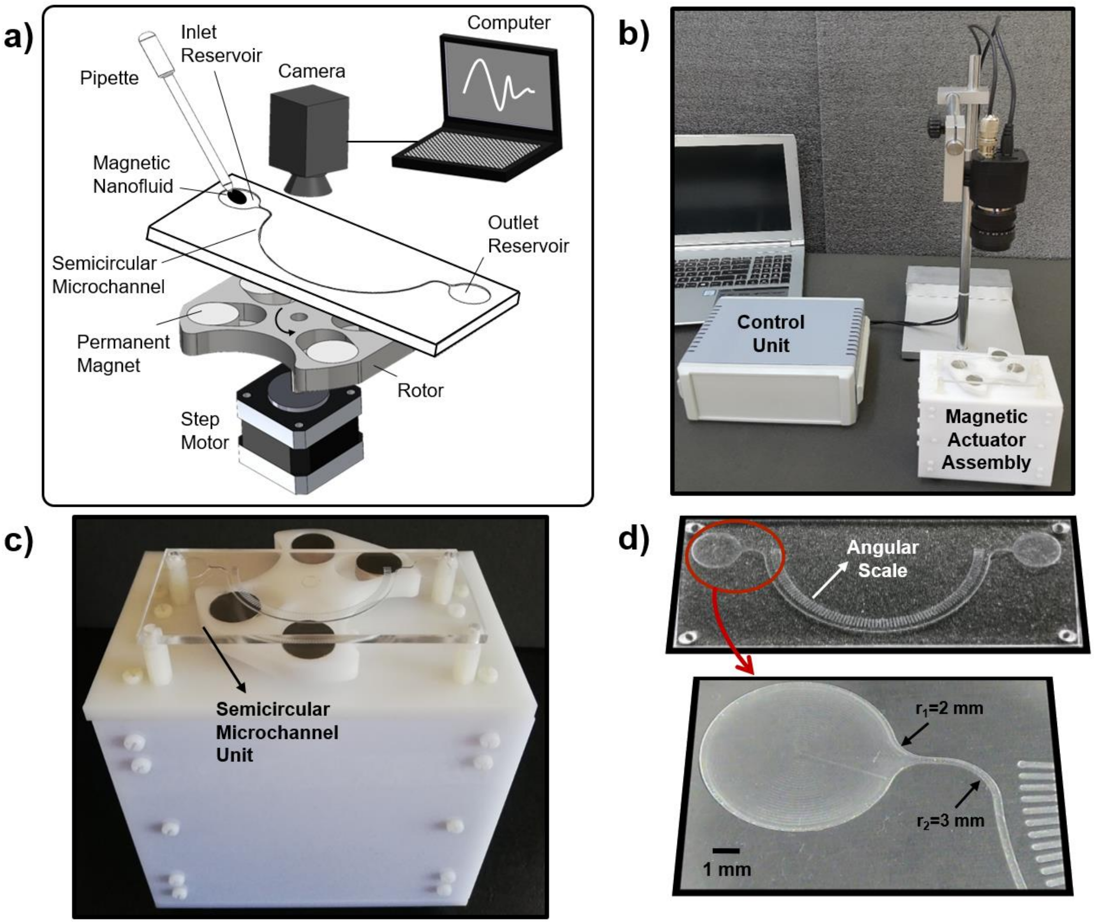

Figure 4.11 (a) Schematic of the setup, (b) Experimental setup for permanent magnetic actuation of the magnetic nanofluid samples and measuring its velocity, (c) The view of the PMA assembly with the semicircular microchannel unit, (d) Semicircular microchannel unit and the optical image of the inlet reservoir connection (Personal archive, 2019)

PMMA substrate was used for the production of the semicircular microchannel unit, due to its low-cost, easy fabrication, good chemical and mechanical properties, transparency, and biocompatibility. Owing to these advantages, they are commonly used for the manipulation of water-based magnetic nanofluids. The semicircular microchannel was also fabricated by a high precision cutting tool with a CNC milling machine (TMW-1050, Tongtai, Taiwan). The semicircular microchannel has 400 μm × 400 μm square cross-section, and its radius is r = 25 mm. For the inlet and outlet of the fluid into the semicircular microchannel, two reservoirs were connected to the semicircular microchannel. The reservoirs have D_r = 10 mm diameter and d = 400 μm depth. They were connected to the semicircular microchannel by two radii to decrease the pressure drop during the charge and the discharge of the magnetic nanofluid. The semicircular microchannel unit was placed 5 mm over the rotor. To keep this distance fix and balanced in order to prevent any gravitational effect, plastic spacers are used. Eventually, a 180˚ precise angular scale was marked by a CNC milling machine for the determination of the magnetic nanofluid position (Figure 4.11d). A technical drawing is provided in Appendix 7 for the microchannel unit.

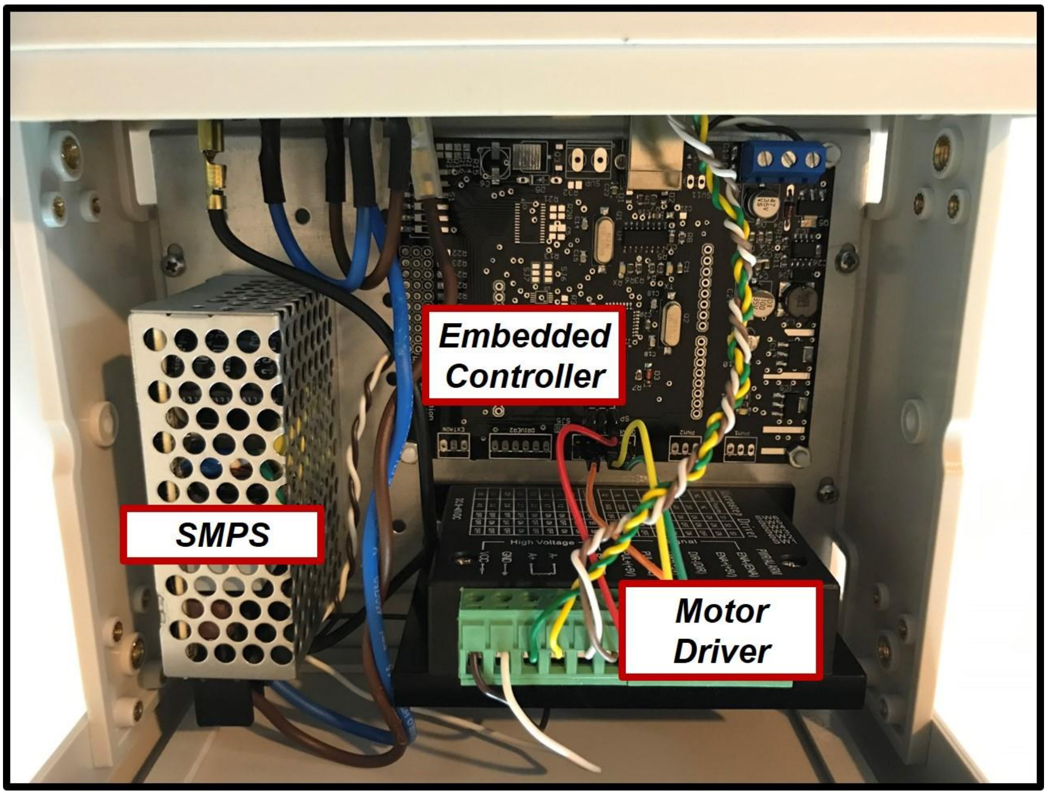

Figure 4.12 Components of the control unit (Personal archive, 2019)

Figure 4.12 indicates an image from the inside of the control unit. The control unit comprises a switch-mode power supply (SMPS), an embedded controller, and a micro-step motor driver. SMPS is able to supply voltage value of 12 V and current value up to 4.2 A. The embedded controller operates with 12 V supply voltage. It has a serial port to communicate with a PC. The embedded controller is also programmable via the serial port. It has ten channels of 12 bit PWM output and two pieces of 16 bit ADC input. Before the experiments, a speed control algorithm is coded into the embedded controller in the control unit, which provides constant speed motion during the operation. In order to the more precise and stable operation of the step motor, a micro-step motor driver was utilized. The driver operates with a supply voltage value range of 9-40 V and provides a current value up to 4 A. It is able to divide each step of the step motor into 16 steps. In other words, by using this micro-step motor driver, the steps of the Nema 14 step motor increased to 3200 steps (200 steps × 16) for a full revolution, which corresponds to 0.1125° (1.8° / 16) for each step.

An online video is recorded via the digital camera (Basler ace Series, acA1920-25uc) during the experiments. The digital camera has a rolling type shutter. It has a CMOS type sensor with dimensions of 4.2 mm×2.4 mm. The resolution and the frame rate of the digital camera are 2 MP (1920×1080) and 26 fps, respectively. The digital camera has a USB 3.0 interface to connect with the PC. The captured video by the digital camera is analyzed offline to determine the fluid velocity. The video recording was started when the magnetic nanofluid sample passes through the inlet section of the semicircular microchannel and recording is stopped when the fluid reaches the outlet. The angular position of the fluid is measured by analyzing video sequences using the angular scale on the microchannel unit, and the average fluid velocity is then determined from the following expression,

$$V_{avg} = \frac{x_2 - x_1}{t_2 - t_1} \tag{4.13}$$

where (x_2-x_1) represents the displacement of the fluid along in the semicircular microchannel, and (t_2-t_1) indicates the elapsed time. After the determination of the average fluid velocity, the average flow rate can be found by,

$$Q_{avg} = A_c.V_{avg} \tag{4.14}$$

where A_c is the cross-sectional area of the semicircular microchannel.

4.3.2 Experimental Procedure

The experiments were conducted for three different Fe_3O_4-water magnetic nanofluid samples, i.e., 1%, 2%, and 3% by volume. For each sample, the fluid motion was observed for five cases in which the permanent magnets are either stationary or rotating with an angular velocity of 7.5, 15, 22.5, and 30 rpm. The stationary experiments were performed to compare the experimental measurements and results of the numerical analyses. The constant speed experiments were then conducted for the performance evaluation of the proposed PMA setup. During the stationary permanent magnet experiments, the rotor was kept at the initial position, as shown in Figure 3.1. For the performance tests, the rotor was started to move from the initial position with a constant angular speed. Each experiment was repeated three times, and the average results are reported in the following section.

4.3.3 Experimental Results and Discussions

4.3.3.1 Compatibility with Numerical Results

Figure 4.13 compares the numerical and experimental velocities of magnetic nanofluids inside the semicircular microchannel when the PMA is stationary. It is observed that the present model predicts well the velocity at the lowest particle concentration. The error is less than 9% for the lowest concentration. However, the discrepancy between the measured and predicted velocities increases up to 40% at higher magnetic nanofluid concentrations.

Similar deviations between the model and the experimental data were also mentioned by Ozbey et al. (2015). In the present model, the characteristics of the magnetic nanofluids are idealized. The influences of surfactant, sedimentation, and agglomeration of the nanoparticles, which may lead to a significant deviation between the predicted and measured velocities at higher concentrations, could not be taken into account in the model. Besides, the magnetic nanoparticles form a chainlike structure in the direction of the field lines that affects the thermophysical properties of the magnetic nanofluids in the presence of the external magnetic field (Khairul, Doroodchi, Azizian & Moghtaderi, 2017) Especially at higher concentration fractions, the viscosity of the magnetic nanofluid may drastically increase (Yang et al., 2014), which results in higher flow resistance and lower flow velocity. The discrepancy between the predicted results and the experimental measurements could be reduced by taking into account the increment in the viscosity of magnetic nanofluid when it is exposed to the external magnetic field.

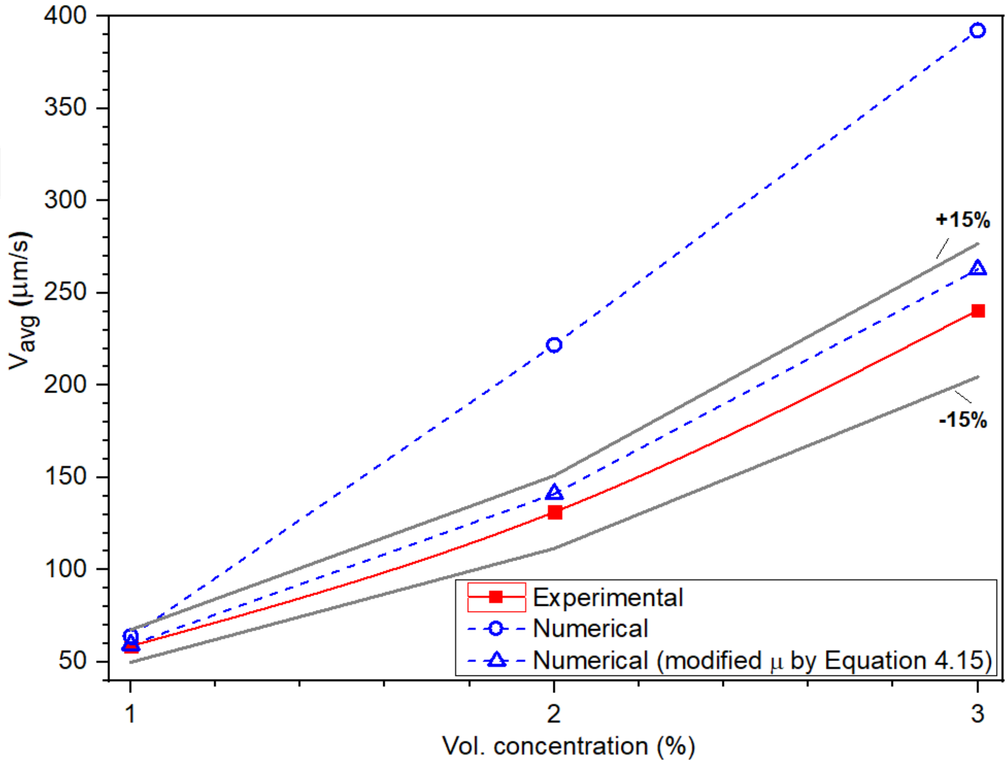

Figure 4.13 Comparison of the numerical and experimental results – Stationary PMA

Additional simulations are conducted by defining the viscosity as a function of the magnetic field,

$$\mu_{nf} = \left(0.035H^2 + 3.1H - 27886.4807\phi^2 + 4263.02\phi + 316.0629 \right) e^{-0.02T} \quad (4.15)$$

Equation 4.15 is proposed by Wang et al. (2016) for Fe_3O_4-water magnetic nanofluids. Comparative results that are provided in Figure 4.13 reveal that the implementation of the viscosity model of Wang et al. (2016) significantly alters the results, and the variable viscosity definition reduces the deviation below 9%.

4.3.3.2 Performance Tests

Performance tests of the PMA are conducted in terms of flow speed induction capability. The experiments were carried out at four different PMA speeds of 7.5, 15, 22.5, and 30 rpm for each concentration of magnetic nanofluid. Figure 4.14 reveals that the average fluid velocity increases with increasing nanoparticle concentration. The reason for this behavior is that the magnetization capability of the superparamagnetic samples increases as the particle concentration increases. Hence, the magnetization of the samples increases, although the external magnetic field strength applied by PMA remains constant. Eventually, the magnetic force acting on the sample increases, which results in higher average fluid velocities.

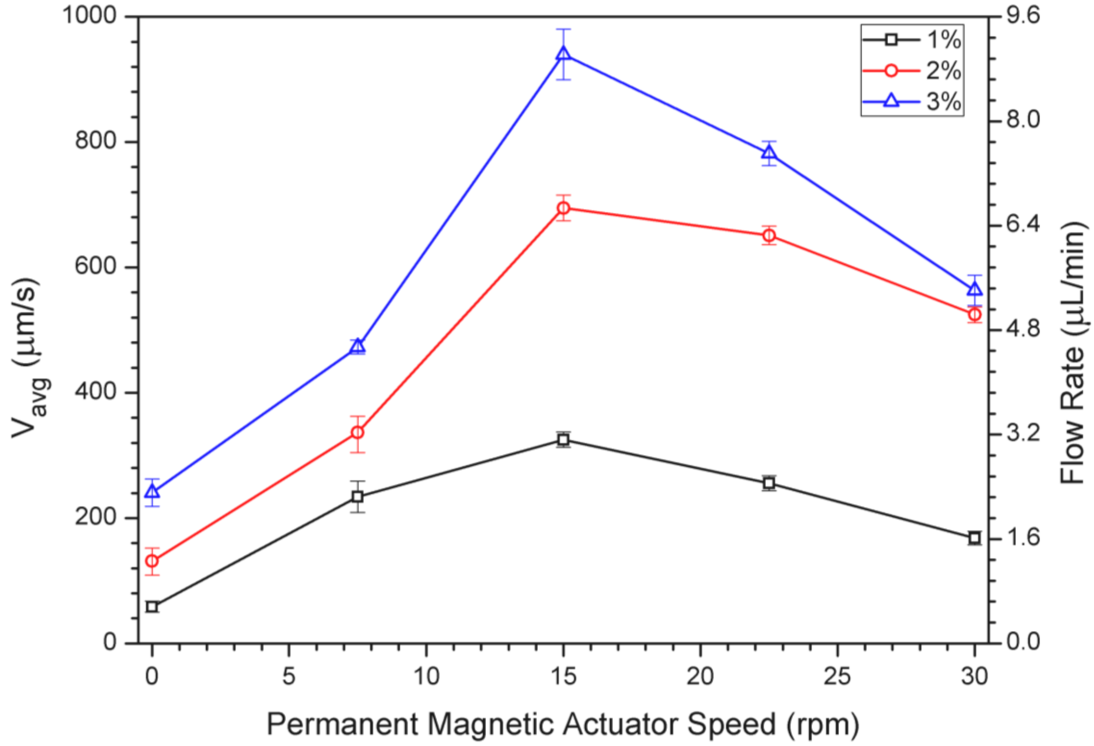

Figure 4.14 The average magnetic nanofluid velocity inside the semicircular microchannel obtained by the experiments for different particle concentrations with respect to actuator speed

The maximum average velocity values are obtained as 325, 695, and 940 µm/s (3.12, 6.67, and 9.02 µL/min) for magnetic nanofluids with vol. concentrations of 1%, 2%, and 3%, respectively. The velocity tends to increase as the speed of the PMA increases. It seems that the critical actuator speed is 15 rpm to achieve the highest fluid velocity. Further increasing the actuator speed reduces the fluid velocity. Similar inversion points were also reported in the previous works of (Kurtoglu et al., 2012; Lee et al., 2011; Liu et al., 2018; Shen, Dovat & Gijs, 2011) for different actuator designs. The observation may be attributed due to the switching of the dominant effect from attractive to adverse effect. When the PMA speed is lower than the critical value, the attractive effect by permanent magnets on the magnetic nanofluid is more dominant than the opposition arising from the interaction between magnetic nanofluid and microchannel walls, i.e., adverse effect, up to a critical actuator speed. Beyond the critical actuator speed, the reactive effect becomes more dominant than the attraction effect, and the amount of the transferred magnetic nanofluid per unit time decreases (Liu et al., 2018).

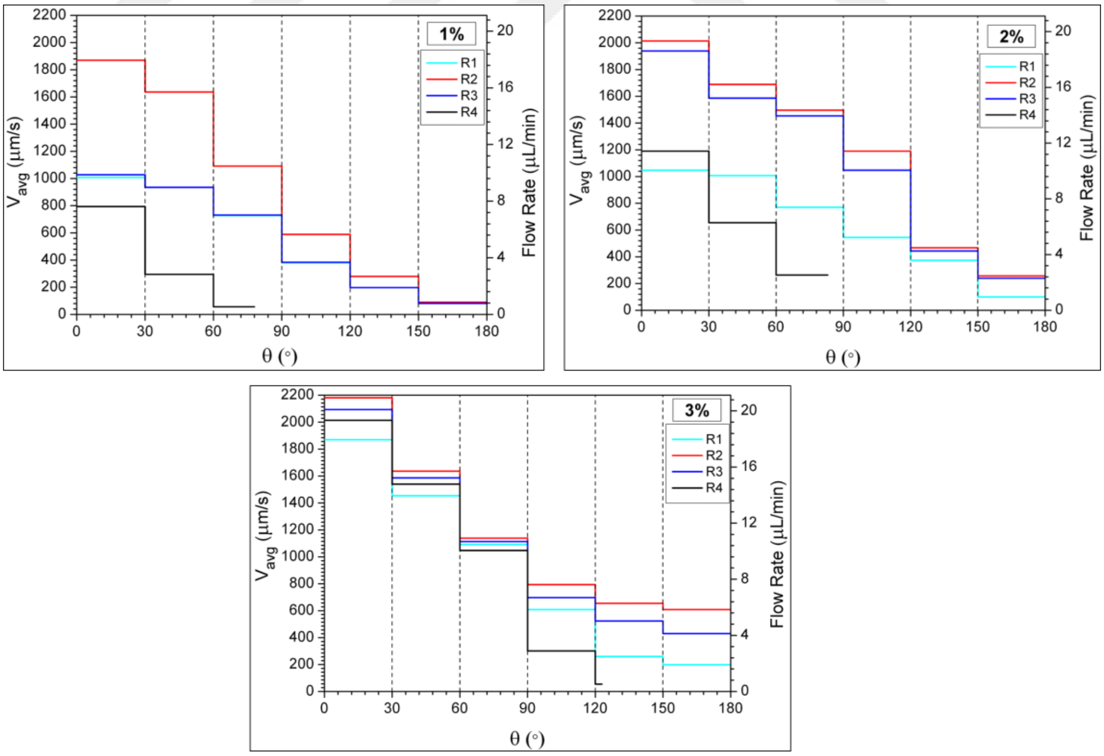

Figure 4.15 The local average interface velocity variation of all samples with four different PMA speed values of R1=7.5, R2=15, R3=22.5, R4=30 rpm

Experimental measurements revealed that the velocities of the magnetic nanofluids do not remain constant along with the angular position of the semicircular microchannel. The semicircular microchannel was divided into six equal segments, and the average fluid velocity was calculated for each segment in order to investigate the variation of interface velocity. The results for four different actuator speeds are shown in Figure 4.15.

It is obtained that the fluid velocity decreases with increasing θ angle with a staircase-like behavior for all cases. The decrease in the velocity may be attributed to two phenomena. First one is the concurrent capillary effect in the semicircular microchannel due to the high ratio between the channel length and width. The velocity caused by the capillary effect in rectangular microchannels can be expressed as (Ichikawa, Hosokawa & Maeda, 2004; Zhu & Duran, 2010):

$$u = -a_0 \frac{h^2}{8\mu} \frac{\Delta P - P_c}{x} \tag{4.16}$$

$$a_0 = \frac{64}{\pi^4} \sum_{n=0}^{\infty} \frac{1}{(2n+1)^4} \left\{ 1 - \frac{2h}{(2n+1)\pi w} \tanh \frac{(2n+1)\pi w}{2h} \right\} \tag{4.17}$$

where h and w are the channel height and width, μ is the viscosity of the fluid, ΔP is the pressure drop through the channel, P_c is the capillary pressure drop and x is the position. In the case of negligible pressure drop when it is compared with the capillary pressure, the velocity of the interface can be expressed as (Banerjee et al., 2017):

$$u = a_0 \frac{h^2}{8\mu} \frac{P_c}{x} \tag{4.18}$$

where,

$$P_c = 2\sigma \frac{\cos\theta}{h} \tag{4.19}$$

In Equation 4.19, σ and θ are the surface tension and contact angle, respectively. If we assume the surface tension and contact angle of the interface are not changing through the microchannel, P_c will be constant. In this case, the velocity drop due to the capillary effects can be estimated by order of magnitude analysis depending on the interface position in the microchannel. The velocity caused by the capillary effect is expected to be maximum at the entrance of the microchannel. Then, it should become to decrease. Therefore, the velocity drop characteristic can be estimated by normalizing each predicted velocity (V') value with the predicted velocity at the entrance (V'_{max}).

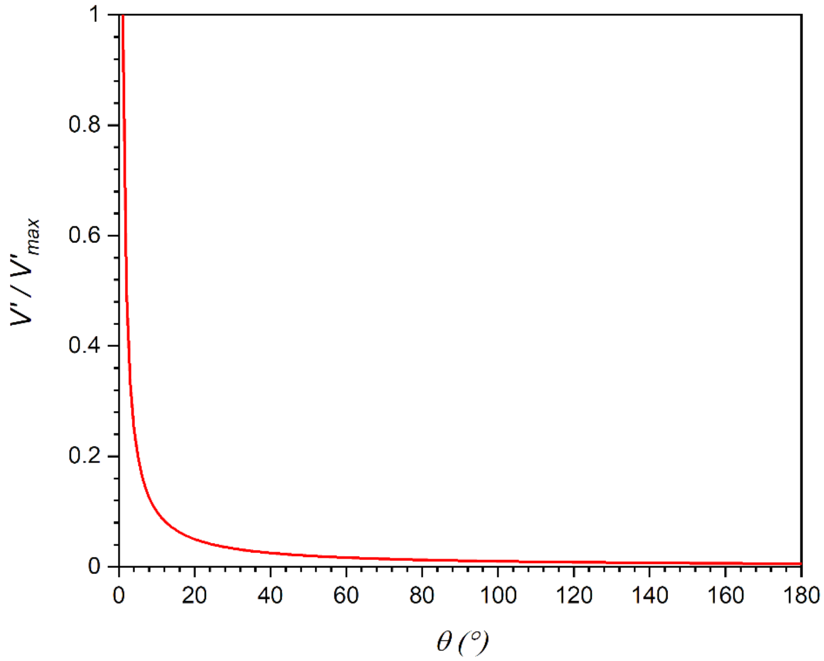

Figure 4.16 Estimation of the velocity drop due to the reducing capillary effects with respect to interface position.

It is seen from Figure 4.16 that the capillary effect decreases as fluid travels inside the channel. The velocity drop related to capillary effects is significant at the beginning (until about $\theta \approx 60°$). Then, this effect is almost negligible.

The second phenomena is increasing frictional effect due to the increasing hydraulic resistance between fluid and microchannel wall. Since the magnetic nanofluid amount inside the microchannel region increases during the actuation, it is expected that there will be an increment in frictional effect. The hydraulic resistance (R) in a microfluidic channel can be expressed by (Damiri & Bardaweel, 2015):

$$R = \frac{\mu L \beta_g}{A^2} \tag{4.20}$$

In Equation 4.20, β_g is a geometric factor depends on channel dimensions. In our setup, the microchannel dimensions are constant, hence β_g and A are constant. Also, viscosity can be assumed as constant for a specific magnetic field characteristic occurs during a constant actuator speed. Therefore, the hydraulic friction characteristic with respect to the interface position can be estimated by normalizing the hydraulic resistance for a corresponding interface position (R) value with the maximum hydraulic resistance (R_{max}) while the microchannel is fully-charged with the fluid.

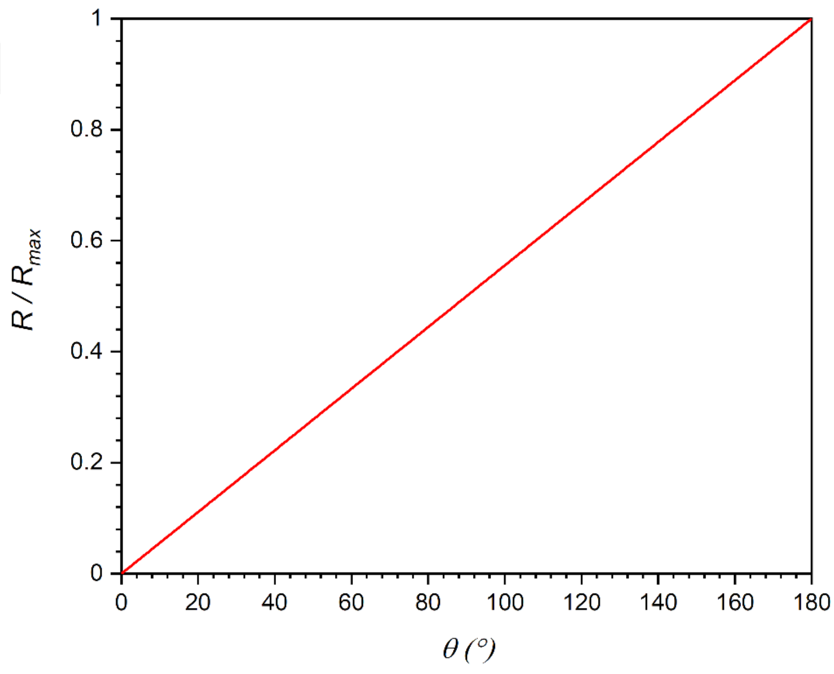

Figure 4.17 Estimation of the hydraulic resistance increment with respect to interface position.

Figure 4.17 demonstrates that the hydraulic resistance linearly increases while the fluid is being charged to the microchannel. This results in an increasing frictional effect during the actuation. Therefore, the fluid velocity gradually decreases under a constant speed actuation effect. The further remarkable observation is that the fluid cannot flow through the whole channel at 30 rpm PMA speed for all magnetic nanofluid samples. Moreover, it is found that the flow discontinues at θ = 78°, 83°, 123° for 1, 2, 3% vol. concentrations, respectively. This is evidence that the resistance by the microchannel walls surpasses the attraction effect and fluid cannot be swept further. Hence, the actuation speed of the system is limited.

CHAPTER FIVE
MAGNETIC NANOFLUID FLOW WITH CONTROLLER

5.1 Introduction

The findings in the previous chapter indicated that the magnetic nanofluid velocity gradually decreases with increasing distance from the semicircular microchannel entrance. In this chapter, it is aimed to alleviate this problem for achieving a more stable magnetic nanofluid flow by applying a real-time control strategy. For this purpose, a digital image processing methodology is developed to estimate the real-time magnetic nanofluid velocity. Following, a closed-loop feedback control algorithm is studied. Then, it is applied to the Fe_3O_4-water magnetic nanofluid flow experiments for 1 vol. % concentrated sample.

5.2 Flow Control Method

5.2.1 Real-time Fluid Velocity Measurement

To achieve a flow rate control in a channel with a constant cross-section area, the velocity of the fluid should be controlled. As it is also can be obtained from Equation 4.13, the flow rate of the magnetic nanofluid will be in a linear relationship with the velocity of magnetic nanofluid.

In micro-sized channels, it is not easy to measure fluid velocity with conventional methods such as mechanical-based, pressure-based and variable area based flowmeters due to the miniaturized structure of the microchannel. On the other hand, digital image processing provides an opportunity to measure fluid velocity without contacting and interfering with the flow structure inside the microchannel. The velocity of a fluid can be estimated precisely with a specific image process methodology to the related application by just determining the displacement of the fluid at a known time interval.

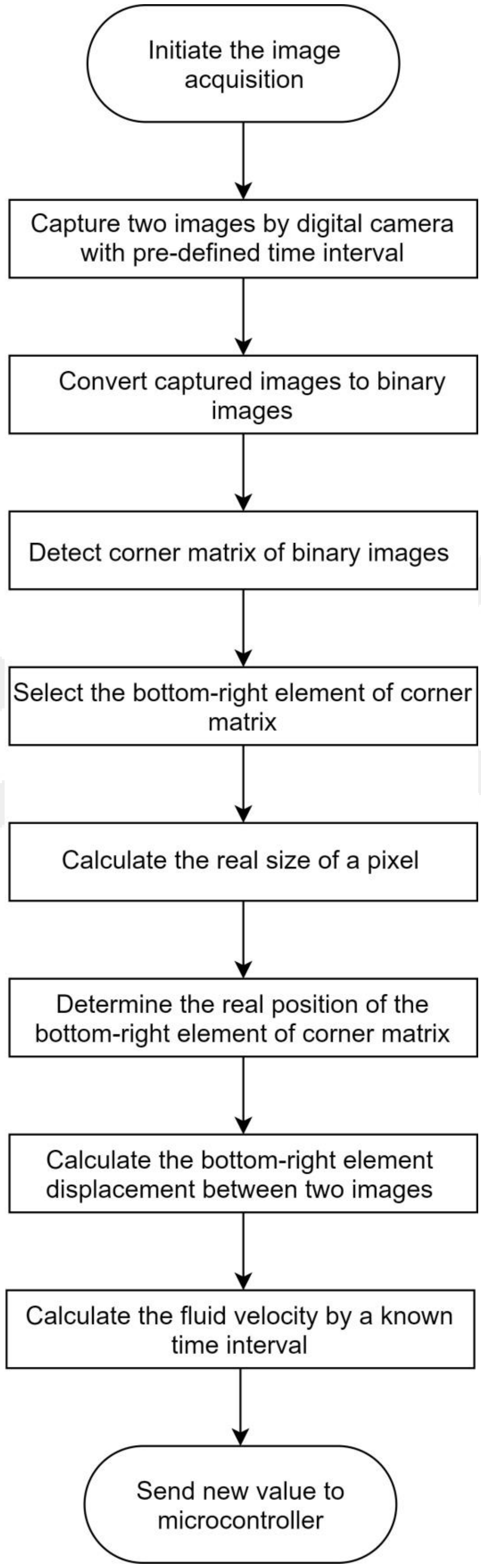

Figure 5.1 Steps of the real-time fluid velocity measurement procedure

In order to estimate the real-time magnetic nanofluid velocity inside the semicircular microchannel, a specific digital image processing algorithm is developed in this thesis. The steps of the real-time magnetic nanofluid velocity measurement structure by digital image processing is presented in Figure 5.1. To apply the image processing procedure given in Figure 5.1, a MATLAB script file is developed.

The same digital camera (Basler ace Series, acA1920-25uc) which was utilized in the previous chapter is employed during the image acquisition. The resolution of the camera is 1920×1080 pixels which will determine the size of the matrices of the captured images. After the initialization of the image acquisition, two images with a pre-defined "*t*" interval are captured by the digital camera. The captured images are three dimensional with a matrix size of 1080×1920×3. Following, the color image is converted to a grayscale image in order to obtain a two-dimensional matrix with a size of 1080×1920. The pixel values for the grayscale images are calculated by Eq. 5.1 with the recommended values by the International Telecommunication Union (ITU) as follows:

$$\mathrm{GR} = 0.299\mathrm{R} + 0.857\mathrm{G} + 0.114\mathrm{B} \tag{5.1}$$

where, *GR*, *R*, *G*, and *B* are pixel values among 0-255 for grayscale, red, green, and blue colors, respectively. Then, the obtained grayscale image is converted to a binary image by using a threshold constant (K_T), which can be varied in the range of 0 to 1. The multiplication of the threshold constant with the range of pixel values specifies the threshold value for the binarization. The pixel values greater than the threshold replace with the value of "1" (white), and the other pixel values replace with the value of "0" (black). In order to enhance the binary image conversion process, in this chapter, the microchannel unit was utilized with white ground color (Figure 5.2). The dimensions and material specifications of the microchannel unit with white ground color are identical with the transparent microchannel unit which was used in the previous chapter.

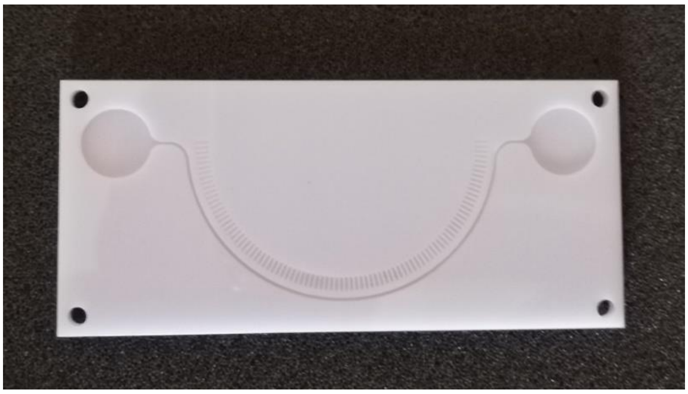

Figure 5.2 The semicircular microchannel unit with white ground color (Personal archive, 2019)

Figure 5.3a demonstrates an example of captured images during real-time image processing. Figure 5.3b and Figure 5.3c indicate the binary images at two different moments. As it can be obtained from the figure, by using a white microchannel surface for a magnetic nanofluid sample with black color, it is possible to binarize the images with good quality.

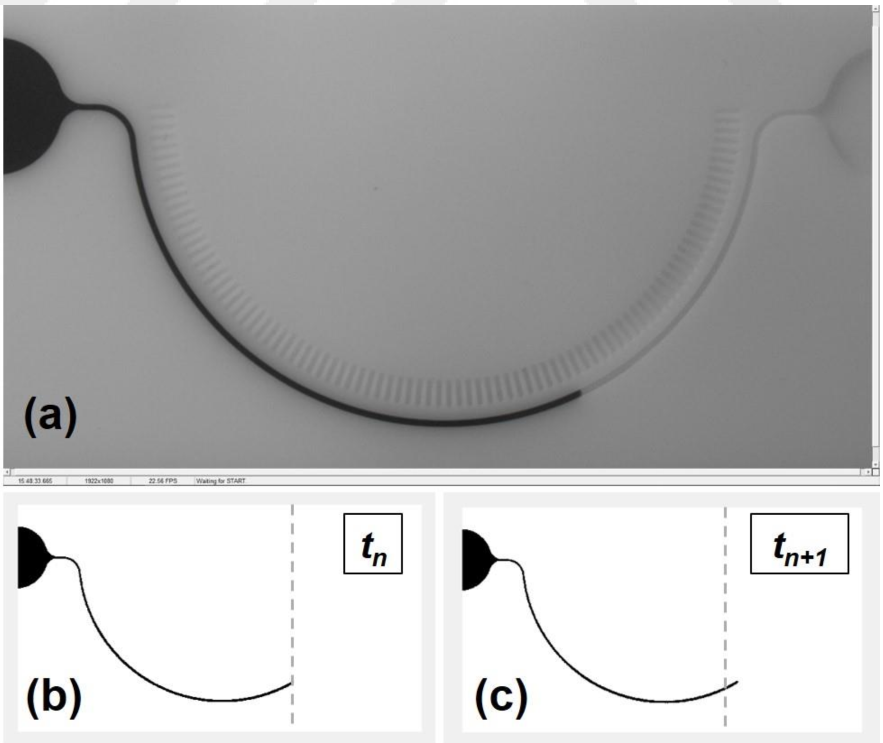

Figure 5.3 (a) A capture from real-time image processing, (b) binary image of the microchannel at "t_n", (c) binary image of the microchannel at "t_n+1"

The accuracy of the real-time velocity estimation heavily depends on the performance of the binarization process, as it directly influences the detection of the endpoint of the magnetic nanofluid inside the microchannel. To demonstrate the performance of the binarization process, a set of conversion is carried out for various threshold constant values, i.e., K_T. Figure 5.4 shows the conversion of an original image into four different binary images for different K_T values of 0.15, 0.25, 0.40, and 0.50.

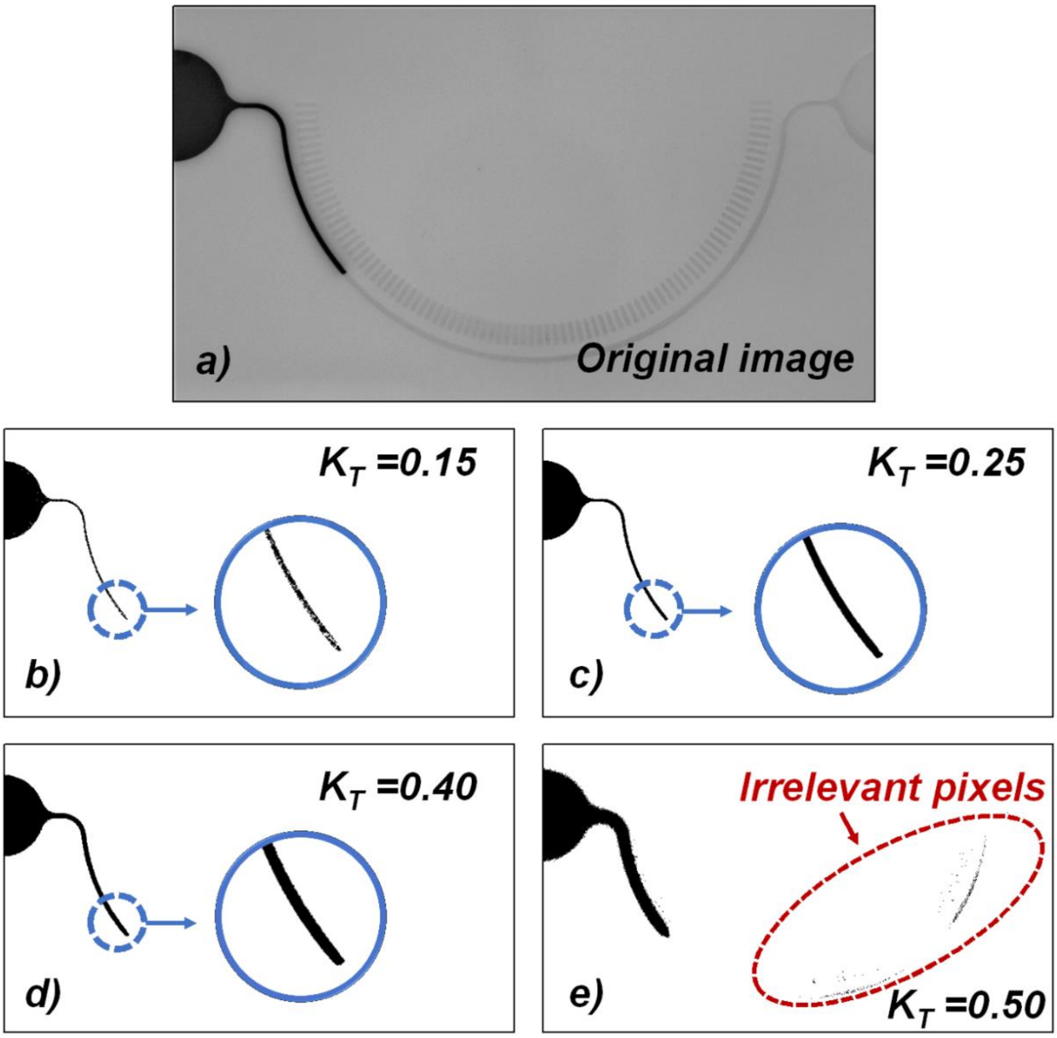

Figure 5.4. (a) An original image of the magnetic nanofluid inside the microchannel during the actuation and its binarized images for different threshold values of (b) K_T =0.15, (c) K_T =0.25, (d) K_T =0.40, and (e) K_T =0.50

Figure 5.4a depicts the magnetic nanofluid inside a white color microchannel, which is the original image captured during the actuation. For the lowest K_T value, the binarization is successfully conducted to determine the overall structure of the magnetic nanofluid inside the microchannel (Figure 5.4b). However, the black pixels are discontinuous in many places, which may cause a considerable error in the position of the endpoint. These discontinuities are eliminated with K_T values of 0.25 and 0.40, as presented in Figure 5.4c and 5.4d. But, this time, it is observed that the width of the detected magnetic nanofluid is different. The detected magnetic nanofluid width measurements in binary images are carried out by comparing them with the original image by using Kinovea software. The measured width values in binary images are found as 396 and 476 μm for K_T values of 0.25 and 0.40, respectively. It means that increasing K_T to 0.40 causes about a 19% error in the detected magnetic nanofluid width which may results in an error in the position of the endpoint. The reason for this increment is attributed to the possible shadows appear on the microchannel due to the edges of the microchannel. Figure 5.4e depicts a binary image obtained with a further increased K_T value of 0.50. It is seen from the figure that there are many irrelevant black pixels are detected on the microchannel unit surface, even there is no magnetic nanofluid. Hence, it is not possible to detect the position of the endpoint correctly.

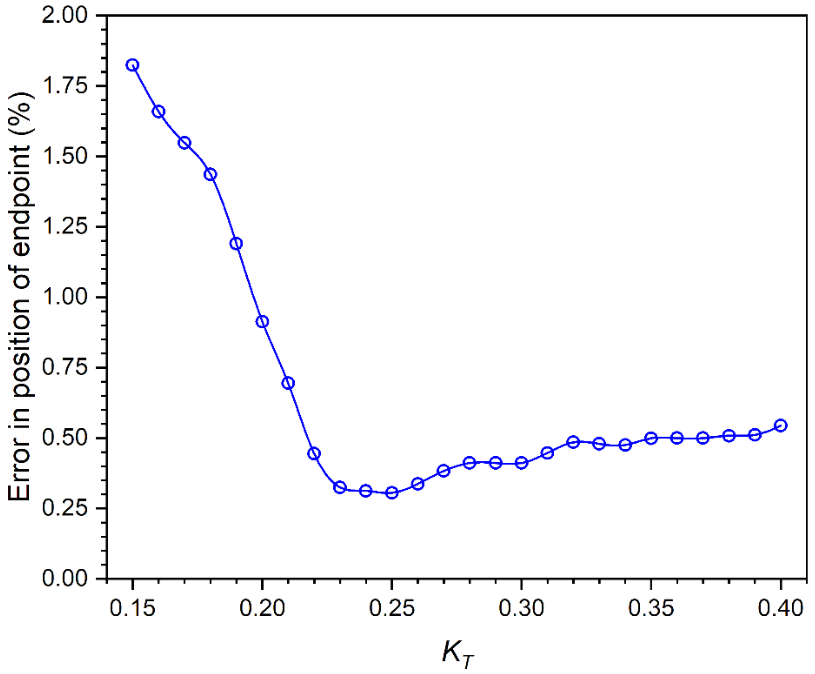

Figure 5.5 Error analysis for the position of the endpoint with respect to K_T

In order to continue with a specific K_T value in real-time velocity estimation during the control process, an error analysis is performed for the position of the endpoint with different K_T values in the range of 0.15-0.40 (Figure 5.5). It is seen from Figure 5.5 that the error in the position of the endpoint is decreased up to a point, and then it starts to increase. More specifically, it is possible to detect the endpoint of the magnetic nanofluid in the microchannel with an error of about 0.3% for K_T values between 0.23 and 0.26. In accordance with this observation, K_T value is selected as 0.25 for the rest of this study.

After the binarization process, the corner matrices for the binary images are determined by using the Harris Corner Detection Algorithm (HCDA) (Harris & Stephens, 1988). HCDA is a mathematical approach for detecting any corners in an image. The basic operation principle of the HCDA is presented in Figure 5.6. If a frame is moved inside a triangular-shaped image, there will be no change in the intensity of black points in any direction (Figure 5.6a). Hence, this region can be considered as a "flat region". In the case of moving a similar frame as shown in Figure 5.6b, there will be a change in the intensity of black points in the only *y*-direction. This means that the region that the frame moves is an "edge". If the movement of the frame is made as it is depicted that in Figure 5.6c, there will be a significant change in the intensity of the black points in both *x*- and *y*- directions. Therefore, the region can be detected as a "corner" in this case.

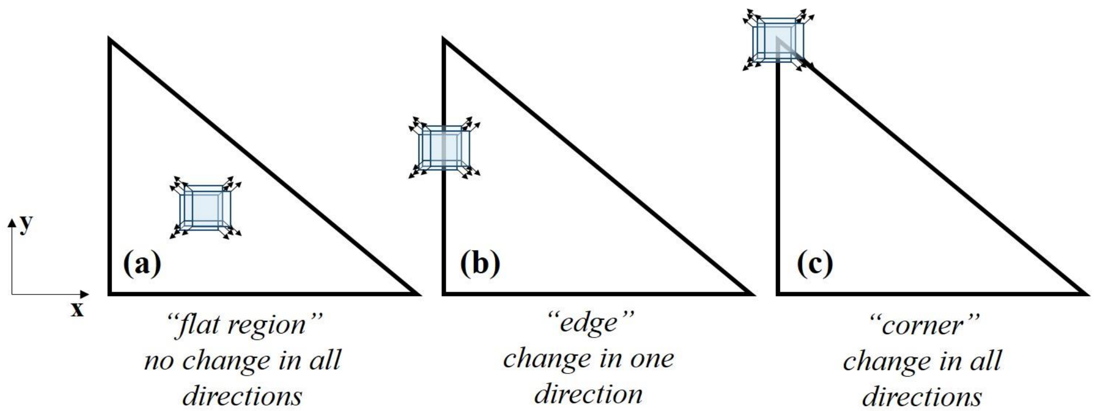

Figure 5.6 Schematic of the HCDA principle to detect (a) flat region, (b) edge, (c) corner

For a two dimensional binary image, the mathematical expression for HCDA is given as:

$$E(\Delta x, \Delta y) = \sum_{x,y} w(x,y)\left[I(x+\Delta x, y+\Delta y) - I(x,y)\right]^2 \tag{5.2}$$

where *w(x,y)* is the window function, *I(x,y)* and *I(x+Δx,y+Δy)* are the intensity functions in the original and shifted position and *E(Δx,Δy)* is the weighted sum of intensity difference multiplied by window function for all pixels. Since solving Equation 5.2 is time-consuming, an approximation can be made by first-order Taylor series expansion for *I(x+Δx,y+Δy)*. Then, Equation 5.2 can be rewritten as:

$$\begin{aligned} E(\Delta x, \Delta y) &= \sum_{x,y} w(x,y)\left[I(x,y) + I_x \Delta x + I_y \Delta y - I(x,y)\right]^2 \\ &= \sum_{x,y} w(x,y)\left[I_x \Delta x + I_y \Delta y\right]^2 \\ &= \sum_{x,y} w(x,y)\left[I_x^2 (\Delta x)^2 + I_y^2 (\Delta y)^2 + 2 I_x I_y (\Delta x)(\Delta y)\right] \end{aligned} \tag{5.3}$$

Equation 5.3 can be expressed in matrix form as follows:

$$E(\Delta x, \Delta y) \approx (\Delta x, \Delta y) M \begin{pmatrix} x \\ y \end{pmatrix} \tag{5.4}$$

$$M = w(x,y) \begin{pmatrix} \sum_{x,y} I_x^2 & \sum_{x,y} I_x I_y \\ \sum_{x,y} I_x I_y & \sum_{x,y} I_y^2 \end{pmatrix} \tag{5.5}$$

In order to classify the different regions as given in Figure 5.5, a score (R) can be defined.

$$R = \det(M) - K\left[tr(M)\right]^2 \tag{5.6}$$

Here, *K* is an empirical constant. According to the obtained value of *R*, the class of the region can be determined as follows. If,

- $R \approx 0$, it is a "flat region",
- $R << 0$, it is an "edge",
- $R >> 0$, it is a "corner".

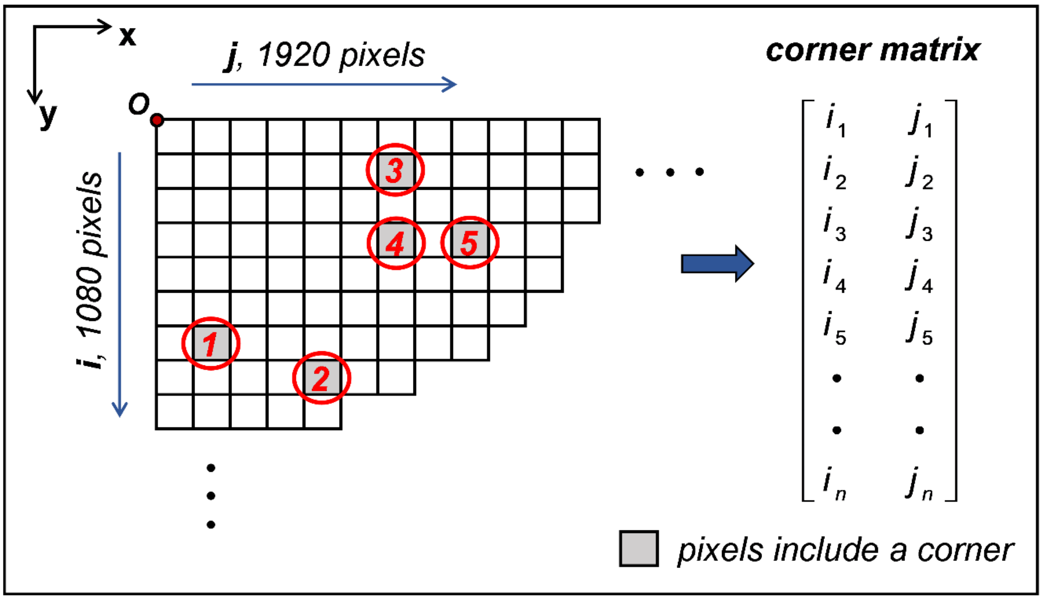

Figure 5.7 Illustration of the logic of the corner matrix generation

Following, the determination of the pixels including a corner is made, and a "corner matrix" is generated. Figure 5.7 demonstrates the idea behind the corner matrix generation. O is set as the origin of the image. The pixels, including a corner, are selected sequentially from left-to-right, and top-to-bottom. Therefore, the last pixel, including a corner, represents the position of the endpoint. By detecting the endpoint of the magnetic nanofluid in pixels, the real position of the endpoint can be determined with Equation 5.7 for the digital camera used in this work.

$$x = j_n \frac{L}{1920}$$
$$y = i_n \frac{W}{1080} \tag{5.7}$$

In Equation 5.7, j_n, and i_n are the positions of the endpoint in x and y direction in terms of pixels, L and W are the lengths and the width of the real captured images in mm.

The geometrical procedure for fluid velocity calculation is presented in Figure 5.8. After specifying the position *(x, y)* of the endpoint in Cartesian coordinates, we are able to determine the angular position of the fluid compared to a reference point.

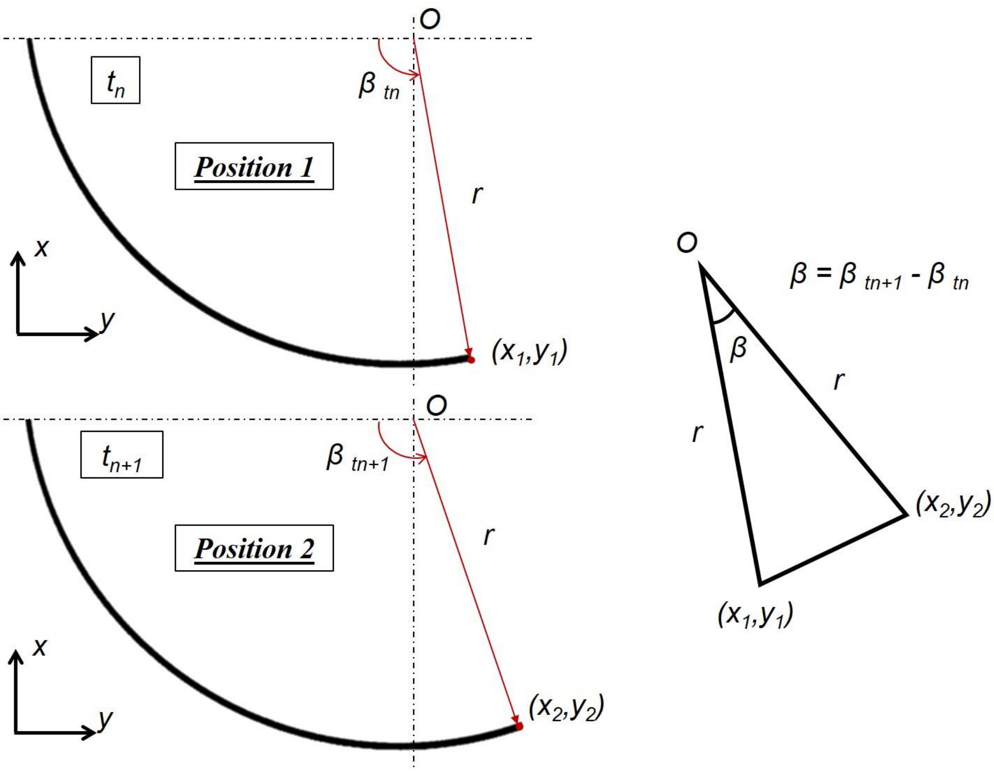

Figure 5.8 Procedure of the determination of the real-time fluid velocity

By applying the law of cosines, the angular displacement (β) between two images can be found. The instantaneous velocity of the fluid is then can be calculated for a specified "*t*" interval by

$$V_f = \frac{(\beta / 180) L_{arc}}{t} \tag{5.8}$$

where L_{arc} is the arc length of the semicircular microchannel.

5.2.2 Control Procedure

The results obtained in the previous chapter indicated that the magnetic nanofluid velocity is not constant and gradually decreases during the entire micropumping process. In order to alleviate the reduction in the fluid velocity and achieve a more stable fluid flow, closed-loop feedback control is applied. An overview of the schematic of the fluid flow control process is given in Figure 5.9.

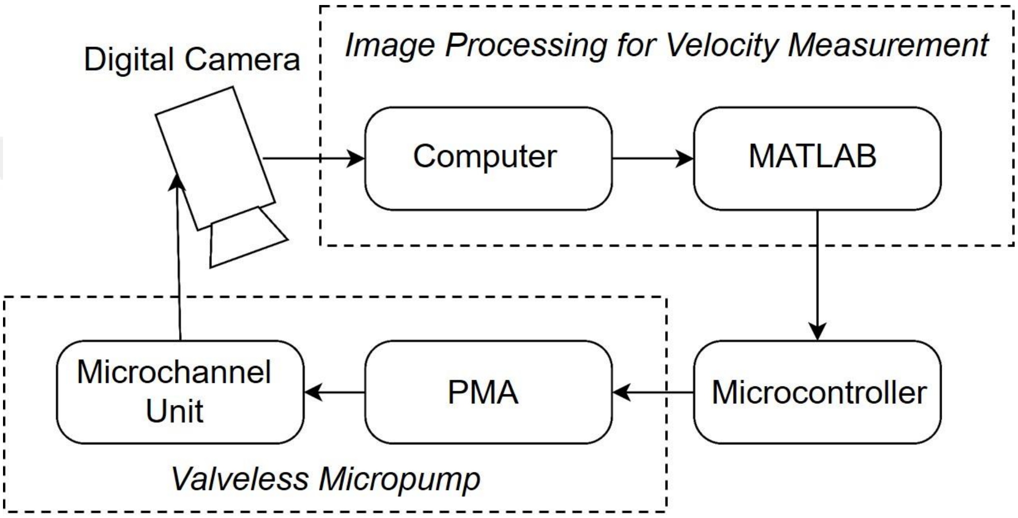

Figure 5.9 Schematic of fluid velocity control process

A digital camera is employed to visualize the magnetic nanofluid inside the microchannel unit. Then, the real-time magnetic nanofluid velocity is determined as explained in the previous section. Following, a microcontroller is utilized to send the necessary control signal to the valveless micropump.

The block diagram of the closed-loop feedback control system is presented in Figure 5.10. During the operation of the valveless micropump, the measured real-time magnetic nanofluid velocity is compared with a reference fluid velocity value. Following, different controllers are applied, i.e., proportional (P), proportional-integral (PI) and proportional-integral-derivative (PID) controls, since this type of controllers is widely used in the control of microfluidics (Delaney et al., 2017). Then, the control signal is sent to the step motor of the PMA via a motor driver. According to the control signal, a new angular speed from the step motor is sent as an input to the I/O system between the beginning of the rotation of the permanent magnets to the velocity achieved inside the microchannel. Then, the output of the system is measured by real-time image processing again as a magnetic nanofluid velocity.

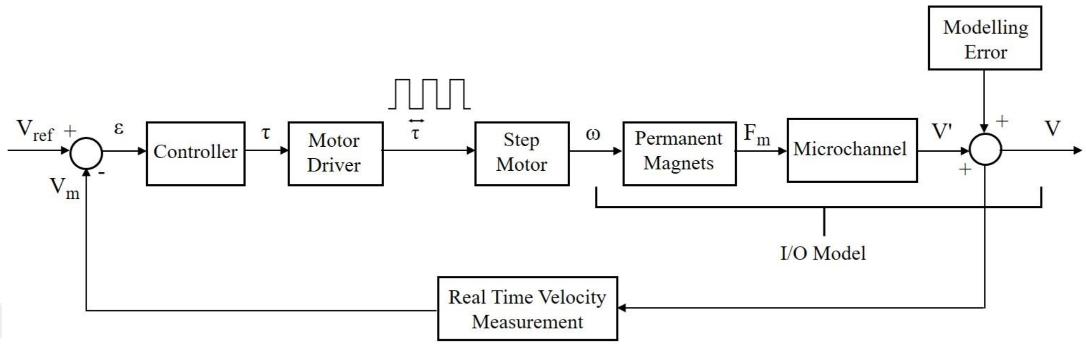

Figure 5.10 Block diagram of the closed-loop feedback control of the valveless micropump

As mentioned above, to observe the more stable magnetic nanofluid flow, P, PI and PID controllers are applied to the valveless micropump. The general equation for a PID controller can be expressed as:

$$u(t) = K_p e(t) + K_i \int_0^t e(t)dt + K_d \frac{de(t)}{dt} \tag{5.9}$$

where u(t) is the control signal, e(t) is the error signal, K_p is the proportional controller coefficient, K_i is the integral controller coefficient, and K_d is the derivative controller coefficient. For P control, K_i is taken as "0", and K_d is taken as "0". Similarly, for PI control, K_d is taken as "0".

To achieve the desired angular speed of the step motor of PMA, the time delay (τ) between each pulse sent by a motor driver to the step motor is altered. Step motor characterization was made for finding the relationship between input (τ) and output (ω) of the step motor. Figure 5.11 demonstrates that the variation of τ with respect to ω. Moreover, an exponential curve is fitted in this figure.

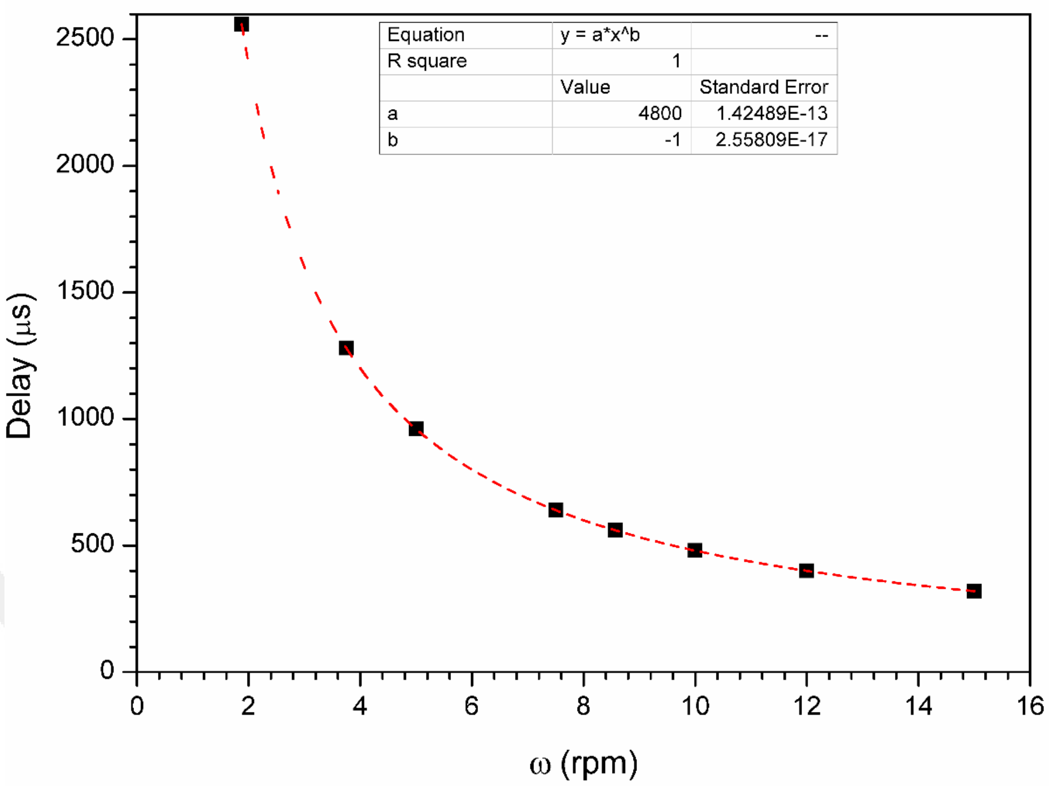

Figure 5.11 The time delay with respect to the angular speed of PMA

The fitted exponential curve presents the relationship between τ and ω almost without any error. The form of the fitted exponential curve can be written as below:

$$\tau = \mathrm{a}\omega^{\mathrm{b}} \tag{5.10}$$

where *a* is the coefficient, and *b* is the exponent.

The relationship between the angular speed of step motor and magnetic nanofluid velocity gained inside microchannel is considered as an I/O model. In order to achieve the I/O model for valveless micropump, experimental data are utilized. As presented in the previous chapter, magnetic nanofluid velocity inside the semicircular microchannel increased up to 15 rpm PMA speed, and then it began to decrease. Therefore, the effective operation range of the valveless micropump is assumed between 0-15 rpm and while estimating the valveless micropump system characteristics, the behavior in this region is considered. Then, the control process is applied in this operating range. Table 5.1 indicates that the operation limits of valveless micropump during the control process.

Table 5.1 Operation limits of valveless micropump during the control process

Parameter	**Min. value**	**Max. value**
***ω* (Input) [rpm]**	0	15
***V* (Output) [μm/s]**	58.8	325.2

To estimate the relationship between *ω* and *V*, a curve fitting is performed by experimental data. In order to enhance the accuracy of this process, further experiments in the valveless micropump were performed at 1.875, 3.75, 5, 8.5, 10, and 12 rpm for 1% vol. Fe_3O_4-water magnetic nanofluid.

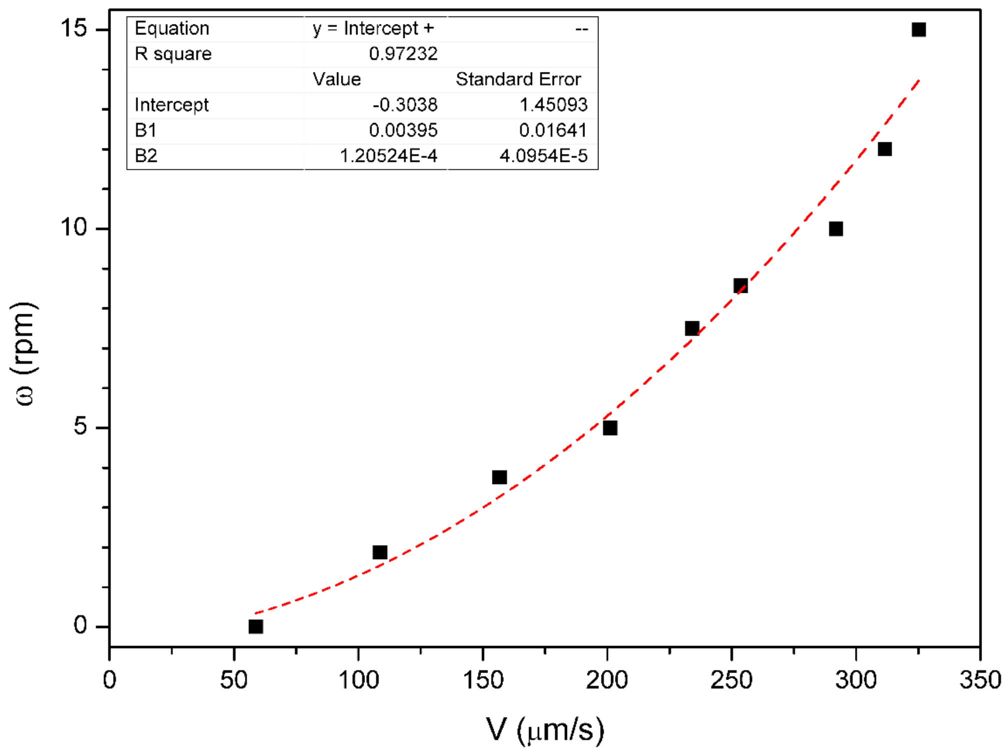

Figure 5.12 The magnetic nanofluid velocity with respect to the angular speed of PMA

The results and the fitted curve is demonstrated in Figure 5.9. It is seen that the fitted curve can successfully predict the relationship between ω and V. The fitted curve is in the form of a second-order polynomial as below:

$$\omega = B_2 V^2 + B_1 V + c \tag{5.11}$$

where B_1, B_2 and c are the constants for the second-order term, first-order term, and intercept, respectively.

The flow chart for the algorithm of the above-presented control process is demonstrated in Figure 5.13. In the beginning, a microcontroller is initiated for serial communication with PC. Following, K_p, K_i, K_d and V_{ref} values are introduced by the user. In the case of the introduced V_{ref} is in the out of the range as presented in Table 5.1, the user is invited to insert a new V_{ref}. After that, the required ω is determined by Equation 5.11. If the calculated ω is not suited to the limits presented in Table 5.1, the user is invited to insert another V_{ref} once more. The time delay to be sent to the step motor for achieving "ω" is then calculated by using Equation 5.10. Following, the instantaneous magnetic nanofluid velocity is measured by image processing procedure, as mentioned in Figure 5.1. The measured velocity is compared with V_{ref}. According to the difference between measured and reference velocity values, the error is determined. After the determination of the error, a new time delay value is specified to drive step motor with a new ω value by applying P, PI, or PID control. If the new ω value is lower than ω_{min} or higher than ω_{max}, then a new ω is assigned as $\omega = \omega_{min}$ or $\omega = \omega_{max}$, respectively.

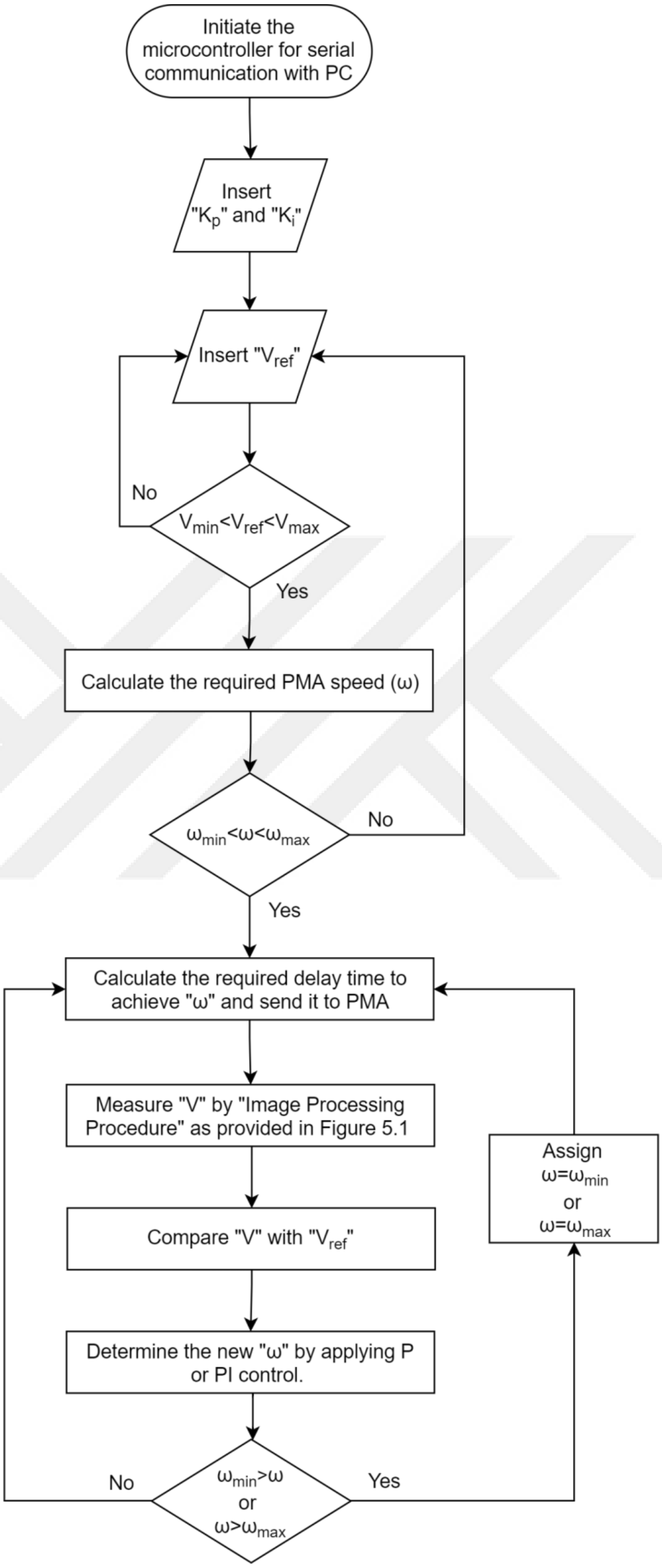

Figure 5.13 The flow chart for the algorithm of the control process

5.3 Results and Discussions

As mentioned previously, P, PI, and PID controls are applied for 1% Fe_3O_4-water magnetic nanofluid to alleviate the gradually decreasing fluid velocity. Figure 5.14 depicts that the real-time magnetic nanofluid velocity while rotating PMA has a constant angular speed with the maximum value of 15 rpm. In other words, there is no controller in this case.

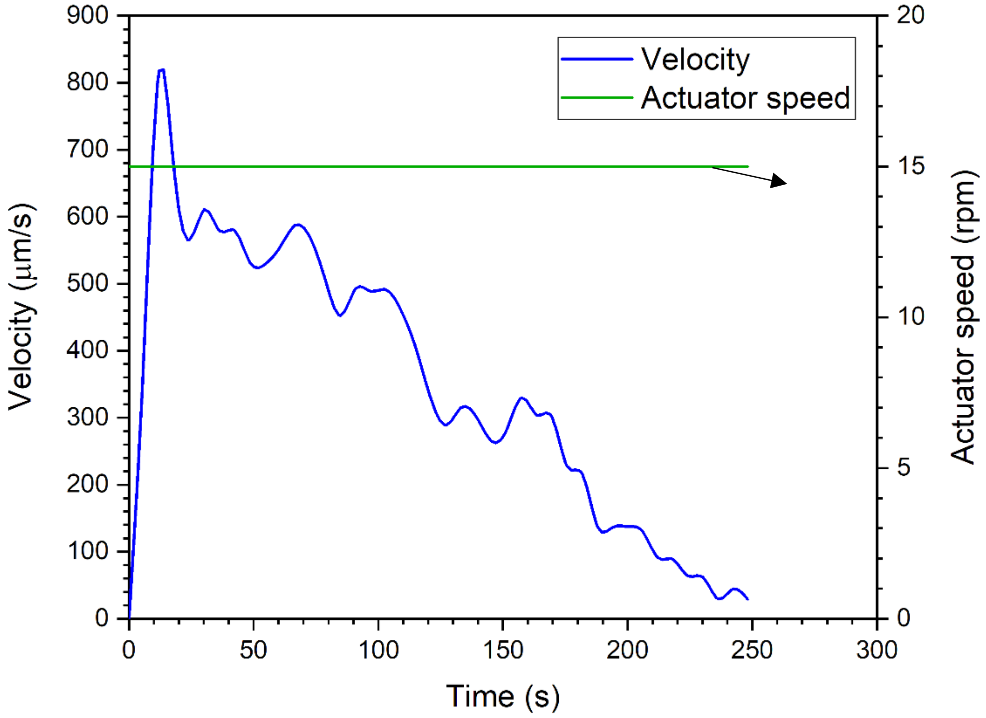

Figure 5.14 Real-time magnetic nanofluid velocity for a constant actuator speed of 15 rpm while there is no controller

The main observation from this figure is the magnetic nanofluid velocity is unstable and drastically decreases almost from 820 µm/s to 20 µm/s during the transportation. This also confirms the gradual decrement in the average magnetic nanofluid velocity explained in the previous chapter. To alleviate this and achieving more stable magnetic nanofluid flow, a P controller is implemented at the beginning.

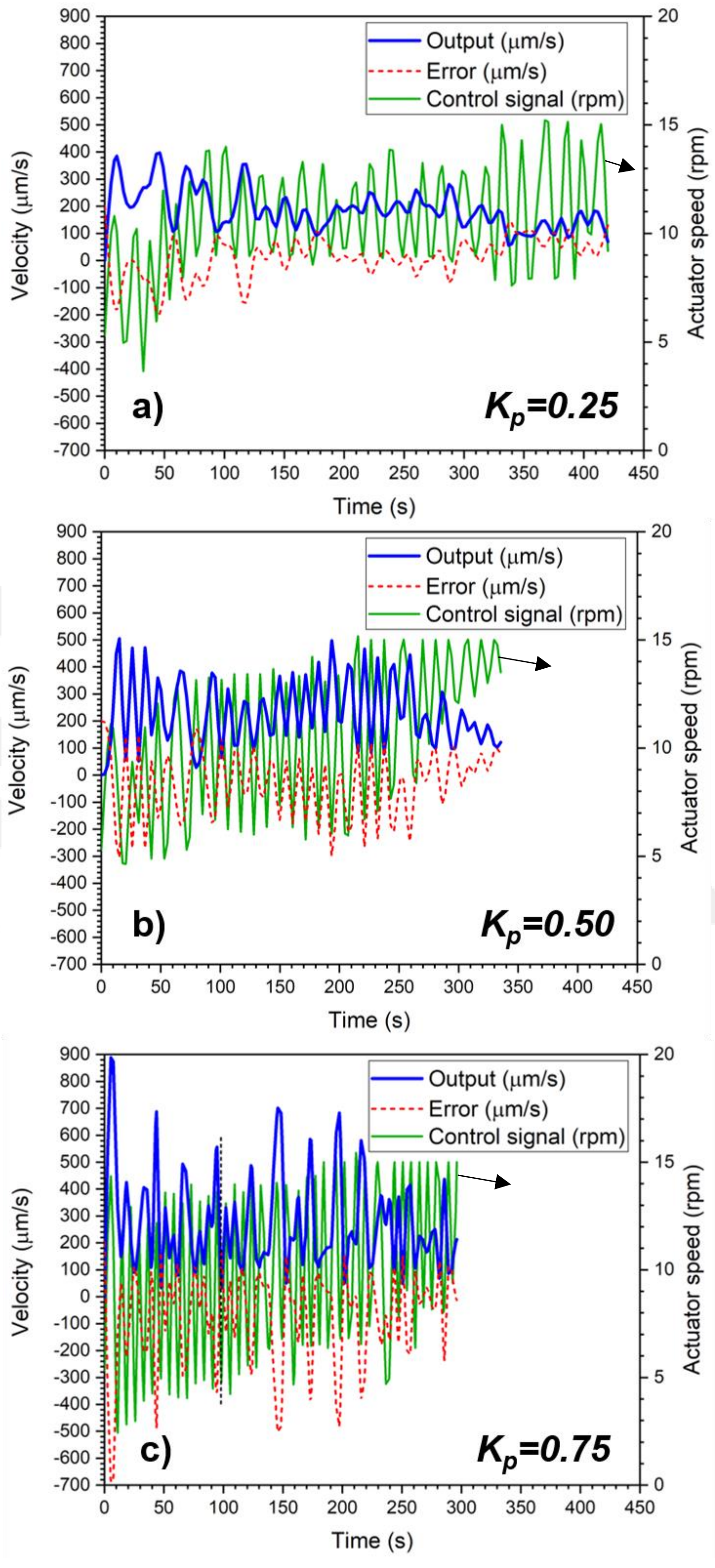

Figure 5.15 Variation of magnetic nanofluid velocity (output), difference between reference and real-time velocity (error), and actuator speed (control signal) for different P controller gains (K_p) of (a) 0.25, (b) 0.50, and (c) 0.75 with 200 μm/s reference fluid velocity value

Figure 5.15 demonstrates that the variation of magnetic nanofluid velocity (output), the difference between reference and real-time velocity (error), and actuator speed (control signal) for different P controller gain values of K_p=0.25, K_p=0.50, and K_p=0.75. The reference velocity value is also set as 200 μm/s. For three K_p values, it is seen that the magnetic nanofluid velocity oscillates around the reference velocity with a considerably high amplitude. As an expected result, it can be inferred from the figure that the amplitude of the oscillations increases, as the K_p value increases. The reason behind that is the increment in the multiplier of the error signal for higher K_p values. Another observation is that the time required for the magnetic nanofluid to reach the outlet of the semicircular microchannel considerably decreases with increasing K_p values. Figure 5.15a depicts that there is still a small decrement trend in magnetic velocity; however, the gradual decrement rate is remarkably lower than no controller case. Therefore, the gradual decrement in the case of no controller can be enhanced when K_p=0.25. The magnetic nanofluid velocity oscillates between ~60-400 μm/s. The average value of the output signal is found at about 187 μm/s. Although a small decrement trend is available after about 270s for K_p=0.50, Figure 5.15b shows that the gradual decrement behavior is almost suppressed. In this case, the magnetic nanofluid velocity oscillates between ~40-500 μm/s. The average value of the signal is obtained by about 233 μm/s. Figure 5.15c indicates that there is almost no decrement trend when K_p=0.75. However, the deviation from the reference velocity remarkably increases. The oscillation of the magnetic nanofluid velocity varies between ~40-880 μm/s. The average value of the signal is observed at about 269 μm/s.

The above-mentioned observations reveal that the microfluidic system is responsive to the P controller compared to operation without a controller. Therefore, the gradual decrement problem can be alleviated with this type of controller. However, the system cannot reach the steady-state due to the presence of an inconstant magnetic force effect caused by significant oscillations in the actuator speed. Moreover, the fluid velocity deviates from the reference velocity with a significant error. In order to suppress this error and achieve a more stable fluid flow, a PI controller is implemented for the next step.

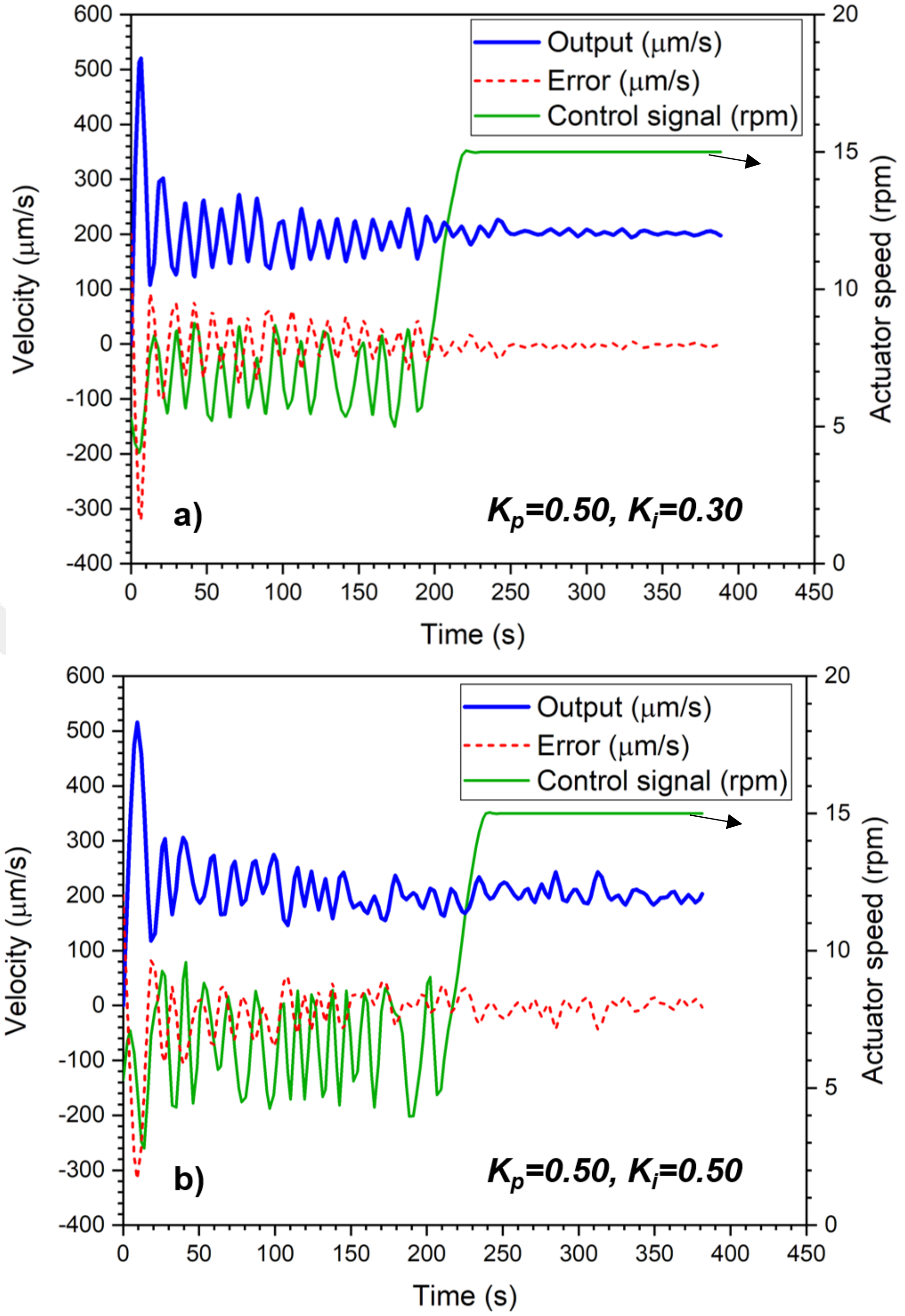

Figure 5.16 Variation of magnetic nanofluid velocity (output), difference between reference and real-time velocity (error), and actuator speed (control signal) for different PI controller parameters of (a) K_p=0.50; K_i=0.30, (b) K_p=0.50; K_i=0.50 with 200 μm/s reference fluid velocity value

Figure 5.16 indicates that the variation of magnetic nanofluid velocity (output), the difference between reference and real-time velocity (error), and actuator speed (control signal) for two different PI controller parameters. K_p is kept constant as 0.50, where K_i is changed from 0.30 to 0.50 for two cases for the same reference velocity. It can be clearly inferred from the figure that the amplitude of the oscillations decreases when compared to the P controller. However, overshoots are still available. It is also observed that by the implementation of the PI controller, the stability of the magnetic nanofluid velocity is considerably enhanced. As provided in Equation 5.9, the integrative controller deals with the cumulative error rather than the current error considered in the proportional controller. This almost causes the elimination of error, and therefore, the magnetic nanofluid velocity varies around the reference value. In the case of K_i=0.30, it is seen from Figure 5.16a that the magnetic nanofluid velocity has a peak value at the beginning of about 520 μm/s. Then, the velocity oscillates between ~110-300 μm/s. After 255 s, the overshoot almost disappears and fluid velocity goes around the reference value until it reaches the outlet of the semicircular microchannel. In that period maximum deviation of the magnetic nanofluid velocity from the reference value is found by about 4%. The average value of the signal is observed as 202 μm/s. Figure 5.16b reveals that the magnetic nanofluid velocity in the case of K_i=0.50. Similarly, with K_i=0.30, the magnetic nanofluid velocity makes a peak of about 520 μm/s at the beginning of the actuation. Also, the oscillation amplitude range of the fluid velocity is very similar for the case of K_i=0.30. However, in this case, the overshoots are more apparent which deteriorates the stability of the flow a little bit when compared with K_i=0.30. The average value of the signal is obtained about 210 μm/s for K_i=0.50.

According to the observations, it seems that the gradual decrement problem can be eliminated by the implementation of the PI controller as well as enhancing the stability of the fluid flow. In the beginning, magnetic nanofluid velocity oscillates around the reference value. Meanwhile, the actuator speed also oscillates around 7 rpm. After passing this region, the actuator speed winds up to a maximum value of 15 rpm and saturation occurs. At the same time, the system reaches the steady-state, and the error becomes around “0”. This means that it is possible to obtain a steady-state region by choosing an integral parameter which will cause a winding up in the control signal.

In order to investigate the possible suppression of the overshoots at the beginning and extent the length of the steady state region, a PID controller is implemented.

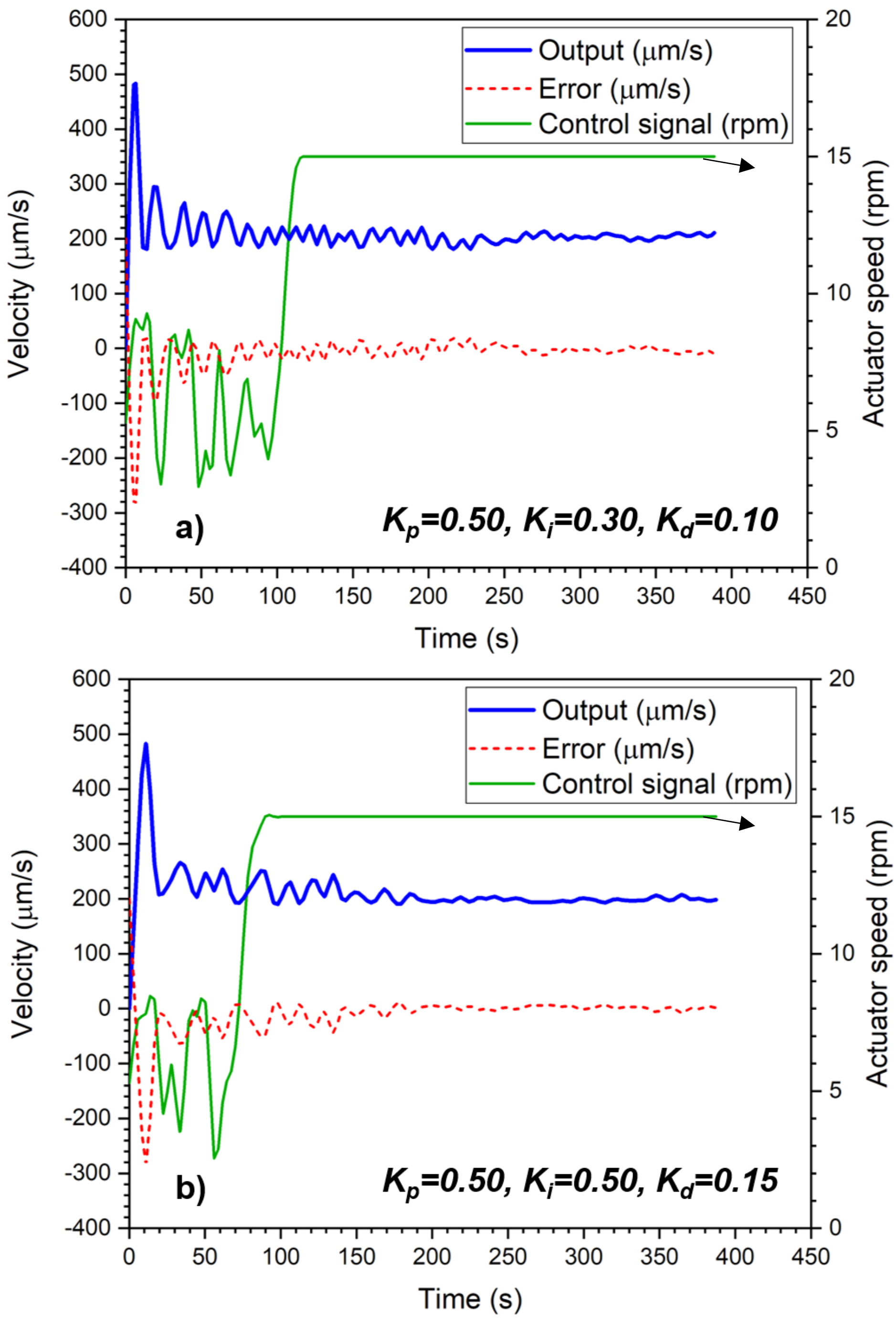

Figure 5.17 Variation of magnetic nanofluid velocity (output), difference between reference and real-time velocity (error), and actuator speed (control signal) for different PID controller parameters of (a) K_p=0.50; K_i=0.30; K_d=0.10, (b) K_p=0.50; K_i=0.30; K_d=0.15 with 200 μm/s reference fluid velocity value

Figure 5.17 depicts the variation of magnetic nanofluid velocity (output), the difference between reference and real-time velocity (error), and actuator speed (control signal) with two different PID controller parameters. In both cases, K_p and K_i are kept constant as 0.50 and 0.30, where K_d is changed from 0.10 to 0.15. It is seen that the overshoots can be reduced further by the implementation of the PID controller when compared with the PI controller. It is also indicated in the figure that the gradual velocity decrement problem can be overcome, and stability of the magnetic nanofluid flow can be enhanced by this type of controller. As provided in Equation 5.9, the derivative controller deals with the slope of the error with respect to time. It means that the derivative term predicting the system behavior which results in enhanced stability and reduced settling time. Figure 5.17a indicates that the magnetic nanofluid velocity has a peak value at the beginning of about 480 μm/s at the beginning of the pumping in the case of K_d=0.10. Then, the velocity becomes to oscillate in the range of ~180-290 μm/s. After 235 s, there is almost no overshoot, and fluid velocity goes around the reference value until it reaches the outlet of the semicircular microchannel. In this case, the average value of the signal is obtained as 206 μm/s. Figure 5.17b demonstrates that the magnetic nanofluid velocity in the case of K_d=0.15. Similarly, with K_d=0.10, the magnetic nanofluid velocity makes a peak of about 480 μm/s at the beginning of the pumping. Then, the velocity oscillates in the range of ~195-260 μm/s, which means that overshoots are more suppressed when compared to K_d=0.15. Moreover, this time, the overshoot disappears after 190 s, and then the fluid velocity goes around the reference velocity. In that period, the maximum deviation of the magnetic nanofluid velocity from the reference value is found by about 3%. The average value of the signal is found to be 207 μm/s.

The implementation of the PID controller depicts that the gradual decrement and stable flow problems can be alleviated. Furthermore, the amplitude of the oscillations decreases gradually. Therefore, the PID controller is a useful tool to control the magnetic nanofluid velocity with reduced overshoots. For both K_d value, the actuator speed oscillates around 6 rpm. Then, actuator speed winds up to a maximum value of 15 rpm, and the system reaches to steady-state. Similarly to PI control, the system saturates, and the error decreases almost around “0”. In contrast to PI control, the time required to reach steady-state remarkably decreases by the implementation of PID control. In other words, adding a derivative parameter provides the system in a wider steady-state region.

In order to evaluate the performance of different controllers, integral square error (ISE) of the signals are considered (Ray, Mohanti & Kishor, 2011).

$$ISE = \int_0^t e^2(t)\,dt \tag{5.12}$$

ISE is a measure for evaluation of system performance by integrating the square of the error for each time interval. Table 5.2 indicates that the different controller parameters and corresponding normalized ISE. The normalization has been made by dividing the ISE value of each controller by the ISE value of “No. 1” which corresponds that all controller parameters are zero.

Table 5.2 Normalized ISE for different controllers

No.	K_p	K_i	K_d	Normalized ISE
#1	0	0	0	1.0000
#2	0.50	0	0	0.3474
#3	0.50	0.30	0	0.0538
#4	0.50	0.30	0.15	0.0311

According to the normalized ISE values in Table 5.2, the error can significantly be reduced by the implementation of PI and PID controllers. However, it seems that the PID controller displays a better performance in terms of ISE due to the reduced oscillations.

Finally, to better understand the stability of magnetic nanofluid flow inside the valveless micropump, the arc segment based average velocity was determined. The semicircular microchannel was divided into six arc segments with 30° angular intervals.

Figure 5.18 depicts that the local average velocity variation for different controller parameters provided, as also in Table 5.2. It is clearly seen from the figure that the stability of the magnetic nanofluid flow enhances significantly by the implementation of P, PI, or PID controllers. It means that the gradual decrement of the magnetic nanofluid velocity can be alleviated by the implementation of three types of controller. When we compared the controllers, the P controller has some fluctuations in terms of the average velocity and there is an appreciable decrement, especially after 150°. However, this decrement can be eliminated by PI and PID controllers. In terms of the PI and PID controllers, the average magnetic nanofluid velocity seems to have a little bit better stability with the PID controller, since the suppression of the oscillations.

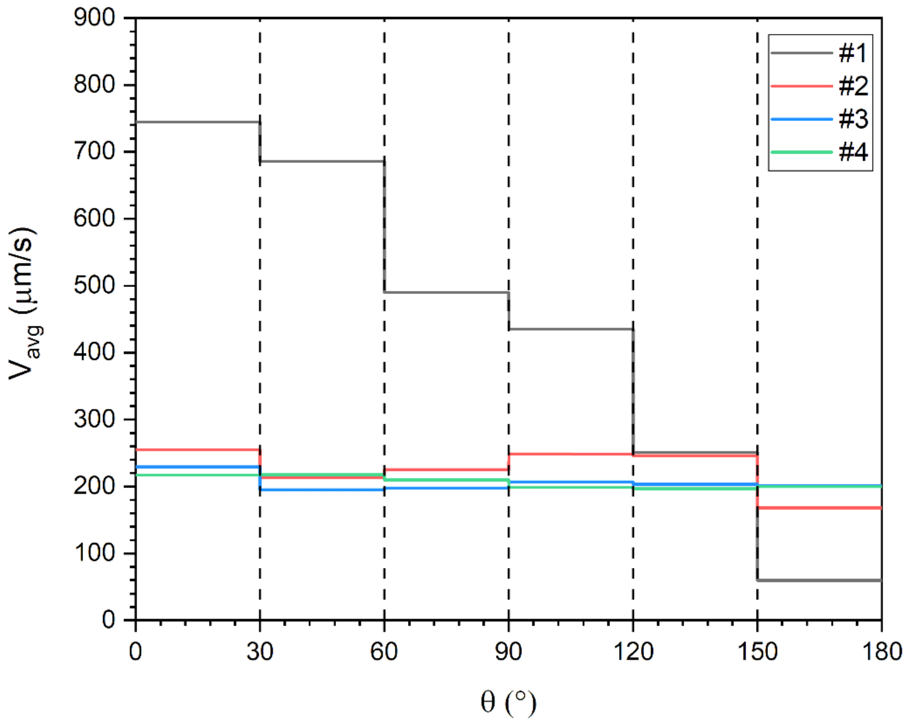

Figure 5.18 The local average velocity variation for different controller parameters

CHAPTER SIX
CONCLUSIONS AND FUTURE WORKS

6.1 Main Findings

A magnetically actuated valveless micropump with Fe_3O_4-water magnetic nanofluid is designed and controlled in the scope of this thesis. First, the properties of magnetic nanofluid are measured. Following, the magnetic nanofluid flow inside the designed valveless micropump is investigated both numerically and experimentally. Finally, a controller is implemented to the valveless micropump in order to control magnetic nanofluid flow. The main findings can be presented as follows:

- Increasing the magnetic particle concentration inside the Fe_3O_4-water magnetic nanofluid results in the increment of viscosity, magnetization capability and thermal conductivity.

- Increasing the magnetic particle concentration from 1 to 4.8 vol. % results in about 97% viscosity increment.

- All Fe_3O_4-water magnetic nanofluid samples demonstrated a superparamagnetic behavior. It means that magnetic particles are getting magnetized in the presence of the magnetic field the external magnetic field is removed, all particles are demagnetized, and there will be no remanence on them.

- Magnetic susceptibility increases about nine times by increasing the magnetic particle concentration from 1 to 4.8 vol. %.

- Magnetic saturation of the Fe_3O_4-water magnetic nanofluid increased with increasing nanoparticle concentration. Maximum saturation value for the most concentrated sample is found as 4.22 emu/g.

• The addition of the magnetic nanoparticles to the base fluid enhanced the thermal conductivity up to 3%. Moreover, this enhancement can be increased by up to 10% with the implementation of the external magnetic field. This confirms that the magnetic nanofluid based micropumping can be a good candidate for thermal management systems in micro-scale.

• The angular interval $\Delta\theta$ between magnet, the pair has a significant influence on the magnetic field generated for the proposed actuator in this thesis. To determine the most appropriate $\Delta\theta$, FF, CF, and B_n/B_t ratio are utilized as evaluation criteria, and $\Delta\theta=60°$ is selected for the present PMA concept.

• By employing a magnet pair rather than a single magnet gave an opportunity to control the arc segment length on the circular path by adjusting the angular interval $\Delta\theta$ between the magnet pair.

• Viscosity has a significant influence on the magnetic nanofluid flow. The model can estimate the magnetic nanofluid velocity for the lowest concentration, i.e., 1% vol., with approximately 9% error by employing experimental viscosity value measured in the absence of the magnetic field. However, this deviation increases by up to 40% for 2 and 3% volumetric concentrations. On the other hand, by using a magnetic field dependent viscosity correlation, this deviation can be reduced to 8.4%.

• It is possible to transport Fe_3O_4-water magnetic nanofluid inside the valveless micropump with an average velocity of the magnetic nanofluid of 940 μm/s for the sample with 3% volumetric concentration at 15 rpm.

• The average velocity of the magnetic nanofluid increases with increasing PMA speed up to 15 rpm, and then it becomes to decrease.

• The performance of the PMA based valveless micropump can just be enhanced by improving the magnetic properties of the magnetic fluid. One should note that when the consumed electrical power by the PMA is constant, e.g., the performance tests at

15 rpm, the flow rate increases almost three times by just increasing the particle concentration of the magnetic nanofluid from 1 to 3% volumetric concentration which resulted in a viscosity increment about 1.4 times. Normally, a remarkable pumping power consumption increment is expected in such a case when the other type of actuators is utilized. It is a significant superiority of magnetic actuators over other types of actuators.

- The velocity of the magnetic nanofluid decreases gradually through the semicircular microchannel. Moreover, the fluid flow discontinues at a specific position for 30 rpm actuator speed for all magnetic nanofluid samples.

- The developed image processing algorithm is able to detect the position of the magnetic nanofluid with an error below 1%. This enables accurate determination of the real-time magnetic nanofluid velocity.

- It is possible to overcome the gradual decrement behavior of the magnetic nanofluid velocity by closed-loop feedback control strategy in order to achieve a more stable magnetic nanofluid flow.

- Application of P control almost overcomes gradual decrement problem in the magnetic nanofluid velocity. However, the fluid flow is still unstable due to the oscillations in velocity.

- PI controller is able to eliminate the gradual decrement of the magnetic nanofluid velocity as well as enhancing the stability of the fluid flow. Oscillations are still available; however, the magnitude of the oscillations is reduced.

- Implementation of the PID controller provided a more stable fluid flow than the other type of controllers by preventing the gradual decrement of the magnetic nanofluid velocity. In addition, it provides a velocity with a maximum 3% deviation from the reference value in the stable zone where the oscillations are almost suppressed.

6.2 Compatibility of the Present Micropump with Analytical Applications

The compact structure of the present valveless micropump enables a simple integration opportunity of the current concept in various microfluidics applications. The microchannel unit is placed at the top part of the micropump, and it is possible to approach the workspace from any other directions. It is also possible to easily visualize the workspace during the actuation when a microscopic observation is necessary from the top of the workspace. Herein a separately designed control unit is implemented rather than utilizing an embedded control unit inside the actuator unit. This approach ensures a flexible scaling opportunity for the micropump.

Micropumping is an essential part of microfluidic systems, where a small amount of fluid transport is required with high precision. The main challenge in micropump design is driving the fluid at a specific flow rate requirement for analytical microfluidics applications. Therefore, the compatibility of a micropump with a candidate application should be determined by comparing the supplied and required flow rates. The required flow rates for some specific analytical applications in various biological, medical, and heat transfer systems are summarized in Table 6.1.

Table 6.1 Flow rate ranges in various microfluidic applications

Application	Flow Rate Range
Low Flow Drug Delivery (Shawgo, Grayson, Li & Cima, 2002)	1-10 μL/min
Chemical Analysis System (Zengerle, Ulrich, Kluge, Richter & Richter, 1995)	160 μL/min
Cell Sorting (Sim, Yoon, Jeong & Yang, 2003)	6.1 μL/min
Cell Culture (Xu et al., 2010)	0.33 μL/min
Pathogen Detection (Rosa, Prakash, Tilley, Fox & Kaler, 2007)	3-5.83 μL/min
Cooling System for Miniature Electronics (Chan, Chen & Liu, 2010)	37.8 μL/min
Microchannel Cooling System (Singhal & Garimella, 2007)	10.5 μL/min

The performance tests indicate that the valveless micropump can drive the working fluid in the flow rate range of 0.56-9.02 μL/min. According to the working ranges for commonly used analytical applications in the available literature given in Table 6.1, the supplied flow rate range of the present valveless micropump system suits well with the requirements for low flow drug delivery, cell sorting, and pathogen detection applications. However, it is possible to reach the flow rate requirements for cell culture and microchannel cooling system with the present design strategy of the valveless micropump due to its scaling flexibility. Moreover, the valveless micropump allows driving the working fluid at lower flow rates, i.e., <10 μL/min, by adjusting the PMA speed. This feature makes the system a good candidate when precise flow control is required.

6.3 Future Works

The interest of the researchers on the idea of contactless actuation of magnetic nanofluids by external magnetic field sources for micropumping systems increases day by day. Therefore, further future studies are still required for specific solutions to the pumping of a tiny amount of liquids in micro-sized channels. The following expressions can be inspirational for the initialization of future research.

- Present valveless micropump is able to operate without any heat generation. This makes it suitable for the pumping of biological liquids. As a future effort, the valveless micropumping strategy may be used for the manipulation of an immiscible secondary biological fluid.

- Different magnetic nanofluids can be investigated and employed inside the valveless micropump to enhance the performance of the system.

- By utilizing the magnetic actuator design strategy in this thesis, application-dependent rescaling of the valveless micropump might be conducted.

- A time-dependent numerical model can be developed in order to investigate the dynamic performance of the valveless micropump depending on different geometrical parameters. Therefore, the cost and time required for the experimental setup can be reduced.

- The adaptive controller strategy can be implemented and the controller parameters can be tuned for enhancing the performance of the flow control.

REFERENCES

Abadeh, A., Passandideh-Fard, M., Maghrebi, M. J., & Mohammadi, M. (2019). Stability and magnetization of Fe_3O_4/water nanofluid preparation characteristics using Taguchi method. *Journal of Thermal Analysis and Calorimetry*, *135*(2), 1323-1334.

Ahn, J. J., Oh, J. G., & Choi, B. (2003). A study on the novel type of ferrofluid magnetic pipette. *Nanotech–Technical Proceedings of the 2003 Nanotechnology Conference and Trade Show, 1*, 226-229.

Ahn, J. J., Oh, J. G., & Choi, B. (2004). A novel type of a microfluidic system using ferrofluids for an application of μ-TAS. *Microsystem Technologies, 10*(8-9), 622-627.

Altan, C. L., Elkatmis, A., Yuksel, M., Aslan, N., & Bucak, S. (2011). Enhancement of thermal conductivity upon application of magnetic field to Fe_3O_4 nanofluids. *Journal of Applied Physics, 110*(9), 093917.

Amani, M., Amani, P., Kasaeian, A., Mahian, O., Kasaeian, F., & Wongwises, S. (2017). Experimental study on viscosity of spinel- type manganese ferrite nanofluid in attendance of magnetic field. *Journal of Magnetism and Magnetic Materials, 428*, 457-463.

Andhariya, N., Chudasama, B., Patel, R., Upadhyay, R. V., & Mehta, R. V. (2008). Field induced rotational viscosity of ferrofluid: Effect of capillary size and magnetic field direction. *Journal of Colloid and Interface Science, 323*(1), 153-157.

Ando, B., Baglio, S., & Beninato, A. (2011). An IR methodology to assess the behavior of ferrofluidic transducers-case of study: A Contactless driven pump. *IEEE Sensors Journal, 11*(1), 93-98.

Arana, M., Bercoff, P. G., & Jacobo, S. E. (2017). Thermomagnetic characterization of organic-based ferrofluids prepared with Ni ferrite nanoparticles. *Materials Science and Engineering B-Advanced Functional Solid-State Materials, 215*, 1-8.

Arulmurugan, R., Vaidyanathan, G., Sendhilnathan, S., & Jeyadevan, B. (2005). Co-Zn ferrite nanoparticles for ferrofluid preparation: Study on magnetic properties. *Physica B-Condensed Matter, 363*(1-4), 225-231.

Ashouri, M., Shafii, M. B., & Moosavi, A. (2017). Theoretical and experimental studies of a magnetically actuated valveless micropump. *Journal of Micromechanics and Microengineering, 27*(1), 015016.

Assadsangabi, B., Ali, M. S. M., & Takahata, K. (2012). Bidirectional actuation of ferrofluid using micropatterned planar coils assisted by bias magnetic fields. *Sensors and Actuators A-Physical, 173*(1), 219-226.

Azizian, R., Doroodchi, E., & Moghtaderi, B. (2016). Influence of controlled aggregation on thermal conductivity of nanofluids. *Journal of Heat Transfer-Transactions of the ASME, 138*(2), 021301.

Bacri, J. C., Perzynski, R., Shliomis, M. I., & Burde, G. I. (1995). Negative-viscosity effect in a magnetic field. *Physical Review Letters, 75*(11), 2128-2131.

Banerjee, U., Sabareesh, M., & Sen, A. K. (2017). Manipulation of magnetocapillary flow of ferrofluid in a microchannel. *Sensors and Actuators B-Chemical, 246*, 487-496.

Basheed, N. G. A., Jain, K., Pathak, S., & Pant, R. P. (2018). Dipolar interaction and magneto-viscoelasticity in nanomagnetic fluid. *Journal of Nanoscience and Nanotechnology, 18*(4), 2746-2751.

Cahill, D. G. (1990). Thermal conductivity measurement from 30 to 750 K: the 3ω method. *Review of Scientific Instruments, 61*(2), 802-808.

Chang, Y. J., Hu, C. Y., & Lin, C. H. (2013). A microchannel immunoassay chip with ferrofluid actuation to enhance the biochemical reaction. *Sensors and Actuators B-Chemical, 182,* 584-591.

Cheng, H. B., Zhang, P., Zhang, Q. J., Wu, J. F., Dai, Y. W., Hu, W., et al. (2014). Effects of surface modification on the stability of suspension and thermal conductivity enhancement of composite Fe nanofluids. *IEEE Transactions on Magnetics, 50*(11), 1-4.

Cherief, W., Avenas, Y., Ferrouillat, S., Kedous-Lebouc, A., Jossic, L., Berard, J., et al. (2015). Effect of the magnetic field direction on forced convection heat transfer enhancements in ferrofluids. *European Physical Journal-Applied Physics, 71*(1), 10901.

Coey, J. M. D. (2002). Permanent magnet applications. *Journal of Magnetism and Magnetic Materials, 248*(3), 441-456.

Dababneh, M. S., Ayoub, N. Y., Odeh, I., & Laham, N. M. (1993). Viscosity, resistivity and surface tension measurements of Fe_3O_4 ferrofluid. *Journal of Magnetism and Magnetic Materials, 125*(1-2), 34-38.

Dadwal, A., & Joy, P. A. (2018). Influence of chain length of long-chain fatty acid surfactant on the thermal conductivity of magnetite nanofluids in a magnetic field. *Colloids and Surfaces A-Physicochemical and Engineering Aspects, 555,* 525-531.

Damiri, H. S., & Bardaweel, H. K. (2015). Numerical design and optimization of hydraulic resistance and wall shear stress inside pressure-driven microfluidic networks. *Lab on a Chip, 15*(21), 4187-4196.

Darabi, J., Rada, M., Ohadi, M., & Lawler, J. (2002). Design, fabrication, and testing of an electrohydrodynamic ion-drag micropump. *Journal of Microelectromechanical Systems*, *11*(6), 684-690.

Delaney, C., McCluskey, P., Coleman, S., Whyte, J., Kent, N., & Diamond, D. (2017). Precision control of flow rate in microfluidic channels using photoresponsive soft polymer actuators. *Lab on a Chip*, *17*(11), 2013-2021.

Desai, R., Upadhyay, R. V., & Mehta, R. V. (2014). Augmentation of chain formation in a magnetic fluid by the addition of halloysite nanotubes. *Journal of Physics D-Applied Physics, 47*(16), 165501.

Devi, N. P., Rao, C. S., & Kumar, K. K. (2018). Suitability of magnetic nanofluid in heat transfer loops. *International Journal of Heat and Technology, 36*(1), 195-200.

Djurek, I., Znidarsic, A., Kosak, A., & Djurek, D. (2007). Thermal conductivity measurements of the $CoFe_2O_4$ and γ-Fe_2O_3 based nanoparticle ferrofluids. *Croatica Chemica Acta, 80*(3-4), 529-532.

Dong, Y. Z., Piao, S. H., & Choi, H. J. (2018). Fe_3O_4/sepiolite magnetic composite particles and their magneto-responsive characteristics. *Colloid and Polymer Science, 296*(1), 11-19.

Ebrahimi, S., & Saghravani, S. F. (2017). Influence of magnetic field on the thermal conductivity of the water based mixed Fe_3O_4/CuO nanofluid. *Journal of Magnetism and Magnetic Materials, 441*, 366-373.

Eijkel, J. C. T., Dalton, C., Hayden, C. J., Burt, J. P., & Manz, A. (2003). A circular AC magnetohydrodynamic micropump for chromatographic applications. *Sensors and Actuators B-Chemical*, *92*(1-2), 215-221.

Esashi, M., Shoji, S., & Nakano, A. (1989). Normally closed microvalve and micropump fabricated on a silicon-wafer. *Sensors and Actuators, 20*(1-2), 163-169.

Fe_3O_4 iron oxide nanoparticles. (n.d.). Retrieved March 8, 2020, from https://www.us-nano.com/inc/sdetail/16809

Foner, S. (1959). Versatile and Sensitive Vibrating-Sample Magnetometer. *Review of Scientific Instruments, 30*(7), 548-557.

Gao, R. L., Li, J., Han, S. N., Wen, B. C., Zhang, T. Z., Miao, H., et al. (2012). Magnetisation behaviour of mixtures of ferrofluids and paramagnetic fluids with same particle volume fractions. *Journal of Experimental Nanoscience, 7*(3), 282-297.

Gavili, A., Zabihi, F., Isfahani, T. D., & Sabbaghzadeh, J. (2012). The thermal conductivity of water base ferrofluids under magnetic field. *Experimental Thermal and Fluid Science, 41*, 94-98.

Ghasemi, E., Mirhabibi, A., & Edrissi, M. (2008). Synthesis and rheological properties of an iron oxide ferrofluid. *Journal of Magnetism and Magnetic Materials, 320*(21), 2635-2639.

Ghasemil, E., Mirhabibi, A., Edrissi, M., Aghababazadeh, R., & Brydson, R. M. (2009). Study on the Magnetorheological Properties of Maghemite-Kerosene Ferrofluid. *Journal of Nanoscience and Nanotechnology, 9*(7), 4273-4278.

Goharkhah, M., Gharehkhani, S., Fallah, S., & Ashjaee, M. (2019). Dynamic measurement of ferrofluid thermal conductivity under an external magnetic field. *Heat and Mass Transfer, 55*(6), 1583-1592.

Gu, H., Tang, X., Hong, R. Y., Feng, W. G., Xie, H. D., Chen, D. X., et al. (2013). Ubbelohde viscometer measurement of water-based Fe_3O_4 magnetic fluid prepared by coprecipitation. *Journal of Magnetism and Magnetic Materials, 348,* 88-92.

Gui, N. G. J., Stanley, C., Nguyen, N. T., & Rosengarten, G. (2018). Ferrofluids for heat transfer enhancement under an external magnetic field. *International Journal of Heat and Mass Transfer, 123*, 110-121.

Hajiyan, M., Ebadi, S., Mahmud, S., Biglarbegian, M., & Abdullah, H. (2019). Experimental investigation of the effect of an external magnetic field on the thermal conductivity and viscosity of Fe_3O_4-glycerol. *Journal of Thermal Analysis and Calorimetry, 135*(2), 1451-1464.

Harris, C. G., & Stephens, M. (1988). A combined corner and edge detector. *Alvey Vision Conference, 15*(50), 147-151.

Hartshorne, H., Backhouse, C. J., & Lee, W. E. (2004). Ferrofluid-based microchip pump and valve. *Sensors and Actuators B-Chemical, 99*(2-3), 592-600.

Hatch, A., Kamholz, A. E., Holman, G., Yager, P., & Bohringer, K. F. (2001). A ferrofluidic magnetic micropump. *Journal of Microelectromechanical Systems, 10*(2), 215-221.

Hejazian, M., Li, W. H., & Nguyen, N. T. (2015). Lab on a chip for continuous-flow magnetic cell separation. *Lab on a Chip, 15*(4), 959-970.

Hezaveh, H., Faziali, A., & Noshadi, M. (2012). Synthesis, rheological properties and magnetoviscos effect of Fe_2O_3/paraffin ferrofluids. *Journal of the Taiwan Institute of Chemical Engineers, 43*(1), 159-164.

Ho, J. E. (2011). Measuring apparent gravity effect to characterize the magnetization of ferro-fluid. *Advanced Materials Research, 250,* 3615-3618.

Hosseini, S. M., Ghasemi, E., Fazlali, A., & Henneke, D. E. (2012). The effect of nanoparticle concentration on the rheological properties of paraffin-based Co_3O_4 ferrofluids. *Journal of Nanoparticle Research, 14*(7), 858.

Hsieh, J., Mach, P., Cattaneo, F., Yang, S., Krupenkine, T., Baldwin, K., & Rogers, J. A. (2003). Tunable microfluidic optical-fiber devices based on electrowetting pumps and plastic microchannels. *IEEE Photonics Technology Letters, 15*(1), 81-83.

Huang, C. W., Huang, S. B., & Lee, G. B. (2006). Pneumatic micropumps with serially connected actuation chambers. *Journal of Micromechanics and Microengineering, 16*(11), 2265-2272.

Ichikawa, N., Hosokawa, K., & Maeda, R. (2004). Interface motion of capillary-driven flow in rectangular microchannel. *Journal of Colloid and Interface Science, 280*(1), 155-164.

Iverson, B. D., & Garimella, S. V. (2008). Recent advances in microscale pumping technologies: a review and evaluation. *Microfluidics and Nanofluidics, 5*(2), 145-174

Karimi, A., Afghahi, S. S. S., Shariatmadar, H., & Ashjaee, M. (2014). Experimental investigation on thermal conductivity of MFe_2O_4 (M = Fe and Co) magnetic nanofluids under influence of magnetic field. *Thermochimica Acta, 598*, 59-67.

Karimi, A., Goharkhah, M., Ashjaee, M., & Shafii, M. B. (2015). Thermal conductivity of and magnetic nanofluids under the influence of magnetic field. *International Journal of Thermophysics*, *36*(10-11), 2720-2739.

Katiyar, A., Dhar, P., Das, S. K., & Nandi, T. (2015). Near-field magnetostatics and Neel-Brownian interactions mediated magneto-rheological characteristics of highly stable nano-ferrocolloids. *Soft Matter*, *11*(8), 1614-1627.

Katiyar, A., Dhar, P., Nandi, T., & Das, S. K. (2016). Enhanced heat conduction characteristics of Fe, Ni and Co nanofluids influenced by magnetic field. *Experimental Thermal and Fluid Science, 78*, 345-353.

Khairul, M. A., Doroodchi, E., Azizian, R., & Moghtaderi, B. (2017). Thermal performance analysis of tunable magnetite nanofluids for an energy system. *Applied Thermal Engineering, 126*, 822-833.

Khosroshahi, M. E., & Ghazanfari, L. (2012). Preparation and rheological studies of uncoated and PVA-coated magnetite nanofluid. *Journal of Magnetism and Magnetic Materials, 324*(24), 4143-4146.

Kim, E. G., Oh, J., & Choi, B. (2006). A study on the development of a continuous peristaltic micropump using magnetic fluids. *Sensors and Actuators A-Physical, 128*(1), 43-51.

Koca, H. D., Doganay, S., & Turgut, A. (2017). Thermal characteristics and performance of Ag-water nanofluid: Application to natural circulation loops. *Energy Conversion and Management*, *135*, 9-20.

Krichler, M., & Odenbach, S. (2013a). Investigation of the effect of a magnetic field on the thermal conductivity in magnetic fluids. *Magnetohydrodynamics, 49*(3-4), 421-424.

Krichler, M., & Odenbach, S. (2013b). Thermal conductivity measurements on ferrofluids with special reference to measuring arrangement. *Journal of Magnetism and Magnetic Materials, 326*, 85-90.

Kronkalns, G. (1977). Measurement of the thermal and electrical conductivities of a ferrofluid in a magnetic field. *Magnitnaya Gidrodinamika, 3*, 138-140.

Kurtoglu, E., Bilgin, A., Sesen, M., Misirlioglu, I. B., Yildiz, M., Acar, H. F. Y., et al. (2012). Ferrofluid actuation with varying magnetic fields for micropumping applications. *Microfluidics and Nanofluidics, 13*(4), 683-694.

Lee, C. Y., Leong, J. C., Wang, Y. N., Fu, L. M., & Chen, S. J. (2012). A Ferrofluidic magnetic micropump for variable-flow-rate applications. *Japanese Journal of Applied Physics*, *51*(4), 047201.

Lee, S. M., Kuan, Y. D., & Sung, M. F. (2011). Design and fabrication of a magnetic fluid micropump for applications in direct methanol fuel cells. *Journal of Power Sources, 196*(18), 7609-7615.

Lenin, R., Dadwal, A., & Joy, P. A. (2018). Thermal conductivity studies on magnetite nanofluids coated with short-chain and long-chain fatty acid surfactants. *Bulletin of Materials Science, 41*(5), 120.

Lenin, R., & Joy, P. A. (2017). Studies on the role of unsaturation in the fatty acid surfactant molecule on the thermal conductivity of magnetite nanofluids. *Journal of Colloid and Interface Science, 506*, 162-168.

Li, Q., Xuan, Y. M., & Wang, J. (2005). Experimental investigations on transport properties of magnetic fluids. *Experimental Thermal and Fluid Science, 30*(2), 109-116.

Li, Q., Xuan, Y. M., & Wang, J. (2006). Measurement of the viscosity of dilute magnetic fluids. *International Journal of Thermophysics*, *27*(1), 103-113.

Li, Z., Yao, J., & Li, D. (2017). Research on the rheological properties of a perfluoropolyether based ferrofluid. *Journal of Magnetism and Magnetic Materials, 424*, 33-38.

Lin, L. H., Li, J., Lin, Y. Q., Liu, X. D., Chen, L. L., Li, J. M., et al. (2014). The extrinsic hysteresis behavior of dilute binary ferrofluids. *European Physical Journal E, 37*(10), 1-6.

Lin, Y. Q., Li, J. A., Liu, X. D., Zhang, T. Z., Wen, B. C., Zhang, Q. M., et al. (2010). Saturation magnetization and law of approach to saturation for self-formed ionic ferrofluids based on $MnFe_2O_4$ nanoparticles. *Chinese Journal of Chemical Physics, 23*(3), 325-330.

Liu, B. D., Zhang, Z., Yang, J. C., Yang, J. H., & Li, D. S. (2018). Rotary ferrofluidic vane micropump with C shape baffle. *Sensors and Actuators B-Chemical, 263,* 452-458.

Malekzadeh, A., Pouranfard, A. R., Hatami, N., Banari, A. K., & Rahimi, M. R. (2016). Experimental investigations on the viscosity of magnetic nanofluids under the influence of temperature, volume fractions of nanoparticles and external magnetic field. *Journal of Applied Fluid Mechanics, 9*(2), 693-697.

Mendelev, V. S., & Ivanov, A. O. (2004). Ferrofluid aggregation in chains under the influence of a magnetic field. *Physical Review E, 70*(5), 051502.

Mohith, S., Karanth, P. N., & Kulkarni, S. M. (2019). Recent trends in mechanical micropumps and their applications: A review. *Mechatronics, 60,* 34-55.

Mousavi, N. S. S., & Kumar, S. (2018). Effective in-field thermal conductivity of ferrofluids. *Journal of Applied Physics, 123*(4), 043902.

Nagvenkar, A. P., Shani, L., Felner, I., Perelshtein, I., Gedanken, A., & Yeshurun, Y. (2018). Surfactant effect on the thermal and electrical behaviors of sonochemically synthesized Fe and Fe-PVP nanofluids and insight into the magnetism of their in-situ oxidized α-Fe_2O_3 analogues. *Journal of Physical Chemistry C, 122*(36), 20755-20762.

Ng, T. Y., Jiang, T. Y., Li, H., Lam, K. Y., & Reddy, J. N. (2004). A coupled field study on the non-linear dynamic characteristics of an electrostatic micropump. *Journal of Sound and Vibration, 273*(4-5), 989-1006.

Nguyen, N. T. (2012). Micro-magnetofluidics: interactions between magnetism and fluid flow on the microscale. *Microfluidics and Nanofluidics, 12*(1-4), 1-16.

Niarchos, D. (2003). Magnetic MEMS: key issues and some applications. *Sensors and Actuators A-Physical, 109*(1-2), 166-173.

Nkurikiyimfura, I., Wang, Y. M., & Pan, Z. D. (2013). Effect of chain-like magnetite nanoparticle aggregates on thermal conductivity of magnetic nanofluid in magnetic field. *Experimental Thermal and Fluid Science, 44*, 607-612.

Nurdin, I., Yaacob, I.I., & Johan, M. R. (2016). Enhancement of thermal conductivity and kinematic viscosity in magnetically controllable maghemite (γ-Fe_2O_3) nanofluids. *Experimental Thermal and Fluid Science, 77*, 265-271.

Ortiz-Salazar, M., Pech-May, N. W., Vales-Pinzon, C., Medina-Esquivel, R., & Alvarado-Gil, J. J. (2018). Magnetic field induced tunability on the thermal conductivity of ferrofluids loaded with carbon nanofibers. *Journal of Physics D-Applied Physics, 51*(7), 075003.

Ozbey, A., Karimzadehkhouei, M., Yalcin, S. E., Gozuacik, D., & Kosar, A. (2015). Modeling of ferrofluid magnetic actuation with dynamic magnetic fields in small channels. *Microfluidics and Nanofluidics, 18*(3), 447-460.

Pamme, N. (2006). Magnetism and microfluidics. *Lab on a Chip, 6*(1), 24-38.

Parekh, K. (2014). Thermo-magnetic properties of ternary polydispersed $Mn_{0.5}Zn_{0.5}Fe_2O_4$ ferrite magnetic fluid. *Solid State Communications, 187*, 33-37.

Parekh, K., & Lee, H. S. (2010). Magnetic field induced enhancement in thermal conductivity of magnetite nanofluid. *Journal of Applied Physics*, *107*(9), 09A310.

Patel, J., Parekh, K., & Upadhyay, R. V. (2015). Maneuvering thermal conductivity of magnetic nanofluids by tunable magnetic fields. *Journal of Applied Physics, 117*(24), 243906.

Paul, G., Das, P. K., & Manna, I. (2016). Synthesis, characterization and studies on magneto-viscous properties of magnetite dispersed water based nanofluids. *Journal of Magnetism and Magnetic Materials, 404*, 29-39.

Paulovicova, K., Tothova, J., Rajnak, M., Wu, Z., Sunden, B., Wadso, L., et al. (2018). Rheological and thermal transport characteristics of a transformer oil based ferrofluid. *Acta Physica Polonica A, 133*(3), 564-566.

Philip, J., Shima, P. D., & Raj, B. (2008). Nanofluid with tunable thermal properties. *Applied Physics Letters, 92*(4), 043108.

Popplewell, J., Alqenaie, A., Charles, S. W., Moskowitz, R., & Raj, K. (1982). Thermal conductivity measurements on ferrofluids. *Colloid and Polymer Science, 260*(3), 333-338.

Priyananda, P., Sabouri, H., Jain, N., & Hawkett, B. S. (2018). Steric stabilization of γ-Fe_2O_3 superparamagnetic nanoparticles in a hydrophobic ionic liquid and the magnetorheological behavior of the ferrofluid. *Langmuir, 34*(9), 3068-3075.

Rasa, M., Bica, D., Philipse, A., & Vekas, L. (2002). Dilution series approach for investigation of microstructural properties and particle interactions in high-quality magnetic fluids. *European Physical Journal E, 7*(3), 209-220.

Ray, P. K., Mohanty, S. R., & Kishor, N. (2011). Proportional-integral controller based small-signal analysis of hybrid distributed generation systems. *Energy Conversion and Management*, *52*(4), 1943-1954.

Rollat, A., Guyonnet, D., Planchon, M., & Tuduri, J. (2016). Prospective analysis of the flows of certain rare earths in Europe at the 2020 horizon. *Waste Management, 49*, 427-436.

Ryapolov, P. A., Polunin, V. M., & Shel'deshova, E. V. (2020). An alternative way to study magnetic fluid magnetization and viscosity. *Journal of Magnetism and Magnetic Materials, 496,* 165924.

Shah, K., Upadhyay, R. V., & Aswal, V. K. (2012). Influence of large size magnetic particles on the magneto-viscous properties of ferrofluid. *Smart Materials and Structures, 21*(7), 075005.

Shen, M., Dovat, L., & Gijs, M. A. M. (2011). Magnetic active-valve micropump actuated by a rotating magnetic assembly. *Sensors and Actuators B-Chemical, 154*(1), 52-58.

Shima, P. D., & Philip, J. (2011). Tuning of thermal conductivity and rheology of nanofluids using an external stimulus. *Journal of Physical Chemistry C, 115*(41), 20097-20104.

Shima, P. D., Philip, J., & Raj, B. (2009). Magnetically controllable nanofluid with tunable thermal conductivity and viscosity. *Applied Physics Letters, 95*(13), 133112.

Sim, W., Oh, J., & Choi, B. (2006). Fabrication, experiment of a microactuator using magnetic fluid for micropump application. *Microsystem Technologies, 12*(12), 1085-1091.

Socoliuc, V., Bica, D., & Vekas, L. (2003). Estimation of magnetic particle clustering in magnetic fluids from static magnetization experiments. *Journal of Colloid and Interface Science, 264*(1), 141-147.

Spencer, W. J., Corbett, W. T., Dominguez, L. R., & Shafer, B. D. (1978). An electronically controlled piezoelectric insulin pump and valves. *IEEE Transactions on Sonics and Ultrasonic*s, 25(3), 153-156.

Suh, Y. J., & Cho, K. (2015). Thermal conductivity enhancement of magnetic fluids under magnetic field based on percolation theory. *Materials Transactions, 56*(8), 1262-1268.

Sundar, L. S., Ramana, E. V., Singh, M. K., & Sousa, A. C. M. (2015). Magnetic field induced enhancement in thermal conductivity and viscosity of stabilized vacuum pump oil (VPO)-Fe_3O_4 magnetic Nanofluids. *Journal of Nanofluids, 4*(1), 7-15.

Susan-Resiga, D., & Vekas, L. (2018). From high magnetization ferrofluids to nano-micro composite magnetorheological fluids: Properties and applications. *Romanian Reports in Physics, 70*(1), 501.

Taufiq, A., Ikasari, F. N., Yuliantika, D., Sunaryono, S., Mufti, N., Susanto, H. et al. (2019). Structural, magnetic, optical and antibacterial properties of magnetite ferrofluids with PEG-20000 template. *Materials Today-Proceedings, 17,* 1728-1735.

Taufiq, A., Saputro, R. E., Sunaryono, Hidayat, N., Hidayat, A., Mufti, N., et al. (2016). Fabrication of magnetite nanoparticles dispersed in olive oil and their Structural and magnetic investigations. *Materials Science and Engineering, 202*(1), 012008.

Thurm, S., & Odenbach, S. (2002). Magnetic separation of ferrofluids. *Journal of Magnetism and Magnetic Materials, 252*(1-3), 247-249.

Thurm, S., & Odenbach, S. (2003). Particle size distribution as key parameter for the flow behavior of ferrofluids. *Physics of Fluids*, *15*(6), 1658-1664.

Turgut, A., Sauter, C., Chirtoc, M., Henry, J. F., Tavman, S., Tavman, I., et al. (2008). AC hot wire measurement of thermophysical properties of nanofluids with 3 omega method. *European Physical Journal-Special Topics, 153*, 349-352.

Turgut, A., Tavman, I., Chirtoc, M., Schuchmann, H. P., Sauter, C., & Tavman, S. (2009). Thermal conductivity and viscosity measurements of water-based TiO_2 Nanofluids. *International Journal of Thermophysics, 30*(4), 1213-1226.

Vanlintel, H. T. G., Vandepol, F. C. M., & Bouwstra, S. (1988). A piezoelectric micropump based on micromachining of silicon. *Sensors and Actuators*, *15*(2), 153-167.

Vasilescu, G. (2006). *Electronic noise and interfering signals: principles and applications* (1st ed.). Berlin, Heidelberg: Springer.

Vekas, L., Bica, D., & Avdeev, M. V. (2007). Magnetic nanoparticles and concentrated magnetic nanofluids: Synthesis, properties and some applications. *China Particuology, 5*(1-2), 43-49.

Vibrating sample magnetometer. (n.d.). Retrieved March 8, 2020, from https://www.magnetic-instrument.com/vibration-sample-magnetometer.htm

Vinod, S., & Philip, J. (2017). Role of field-induced nanostructures, zippering and size polydispersity on effective thermal transport in magnetic fluids without significant viscosity enhancement. *Journal of Magnetism and Magnetic Materials, 444*, 29-42.

Vinod, S., & Philip, J. (2018). Experimental evidence for the significant role of initial cluster size and liquid confinement on thermo-physical properties of magnetic nanofluids under applied magnetic field. *Journal of Molecular Liquids*, *257*, 1-11.

Vshivkov, S. A., Rusinova, E. V., & Galyas, A. G. (2016). Effect of a magnetic field on the rheological properties of iron oxide-water-glycerol system. *Rheologica Acta, 55*(2), 155-161.

Wagner, V. E., Balda, J. C., Barnes, T. M., Emannuel, A. E., Ferraro, R. J., Griffith,et al. (1993). Effects of harmonics on equipment. *IEEE Transactions on Power Delivery, 8*(2), 672-680.

Wang, C. H., & Lee, G. B. (2006). Pneumatically driven peristaltic micropumps utilizing serpentine-shape channels. *Journal of Micromechanics and Microengineering, 16*(2), 341-348.

Wang, J. M., Zuo, Z. P., Zhao, Y. Q., Hou, D. B., & Li, Z. X. (2019). Preparation and viscosity characteristics of nano-scale magnetic fluid oil-film bearing oil. *Journal of Nanoscience and Nanotechnology, 19*(5), 2688-2694.

Wang, J. Z., Fan, M. X., Bian, X. F., Yu, M. C., Wang, T. Q., Liu, S., et al. (2018). Enhanced magnetic heating efficiency and thermal conductivity of magnetic nanofluids with FeZrB amorphous nanoparticles. *Journal of Magnetism and Magnetic Materials, 465*, 480-488.

Wang, L., & Yuan, F. G. (2008). Vibration energy harvesting by magnetostrictive material. *Smart Materials and Structures, 17*(4), 045009.

Wang, L. J., Wang, Y. H., Yan, X. K., Wang, X. Y., & Feng, B. (2016). Investigation on viscosity of Fe_3O_4 nanofluid under magnetic field. *International Communications in Heat and Mass Transfer, 72*, 23-28.

Wang, S. H., Yang, C. C., & Bian, X. F. (2012). Magnetoviscous properties of Fe_3O_4 silicon oil based ferrofluid. *Journal of Magnetism and Magnetic Materials, 324*(20), 3361-3365.

Wang, T. Q., Bian, X. F., Yang, C. C., Zhao, S. C., & Yu, M. C. (2017). Ferrofluids based on Co-Fe-Si-B amorphous nanoparticles. *Applied Surface Science, 399*, 663-669.

Wang, W., Zhuang, L., Zhang, Y., & Shen, H. (2015). Synthesis of monodisperse MFe_2O_4 (M=Fe and Zn) nanoparticles for polydiethylsiloxane-based ferrofluid with a solvothermal method. *Materials Research Bulletin, 69*, 61-64.

Weston, M. C., Gerner, M. D., & Fritsch, I. (2010). Magnetic fields for fluid motion. *Analytical Chemistry, 82*(9), 3411-3418.

Whitesides, G. M. (2006). The origins and the future of microfluidics. *Nature, 442*(7101), 368-373.

Yamahata, C., & Gijs, M. A. M. (2004). Plastic micropumps using ferrofluid and magnetic membrane actuation. Paper presented at the *17th IEEE International Conference on Micro Electro Mechanical Systems, Maastricht, Netherlands,* 458-461.

Yamahata, C., Lotto, C., Al-Assaf, E., & Gijs, M. A. M. (2005). A PMMA valveless micropump using electromagnetic actuation. *Microfluidics and Nanofluidics, 1*(3), 197-207.

Yang, C. C., Bian, X. F., Guo, T. X., Zhang, K., & Liu, Y. (2014). Investigation of Fe_3O_4 aqueous ferrofluids before and after freezing. *Soft Materials, 12*(3), 346-351.

Yu, L. Q., Zheng, L. J., & Yang, J. X. (2000). Study of preparation and properties on magnetization and stability for ferromagnetic fluids. *Materials Chemistry and Physics, 66*(1), 6-9.

Zeng, S. L., Chen, C. H., Mikkelsen, J. C., & Santiago, J. G. (2001). Fabrication and characterization of electroosmotic micropumps. *Sensors and Actuators B-Chemical*, *79*(2-3), 107-114.

Zeuner, A., Richter, R., & Rehberg, I. (1998). Experiments on negative and positive magnetoviscosity in an alternating magnetic field. *Physical Review E, 58*(5), 6287-6293.

Zhang, L. Y., Dou, Y. H., Zhang, L., & Gu, H. C. (2007). Magnetic behaviour and heating effect of Fe_3O_4 ferrofluids composed of monodisperse nanoparticles. *Chinese Physics Letters, 24*(2), 483-486.

Zhu, Y., & Petkovic-Duran, K. (2010). Capillary flow in microchannels. *Microfluidics and Nanofluidics*, *8*(2), 275-282.

APPENDICES

APPENDIX 1: List of Publications

- Doganay, S., Cetin, L., Ezan, M. A., & Turgut, A. Control of a Magnetic Actuator for Constant Flow Rate Microfluidic Flow. *In preparation*.

- Doganay, S., Cetin, L., Ezan, M. A., & Turgut, A. (2020). A Rotating Permanent Magnetic Actuator for Micropumping Devices with Magnetic Nanofluids. *Journal of Micromechanics and Microengineering*, *30*(7), 075012.

- Doganay, S., Alsangur, R., & Turgut, A. (2019). Effect of external magnetic field on thermal conductivity and viscosity of magnetic nanofluids: a review. *Materials Research Express*, *6*(11), 112003.

- Doganay, S., Turgut, A., & Cetin, L. (2019). Magnetic field dependent thermal conductivity measurements of magnetic nanofluids by 3ω method. *Journal of Magnetism and Magnetic Materials*, *474*, 199-206.

- Doganay, S., Turgut, A., & Cetin, L. (2017). Ferrofluid Plug Actuation for Micro Pumping Systems. *Key Engineering Materials*, *750*, 168-172.

APPENDIX 2: Nomenclature

$\mathbf{H}$	external magnetic field strength (G)
$\mathbf{M}$	magnetization (emu/g)
$\mathbf{m}$	magnetic moment (A.m^2)
$\mathbf{r}$	position vector (m)
k_B	Boltzmann constant (m^{2}kg/s^{2}K)
T	temperature (°C)
$\mathbf{F_m}$	magnetic force (N)
Q	magnetizable volume (m^3) or flow rate (µL/min)
$\mathbf{B}$	magnetic flux density (mT)
R	resistance (ohm)
e_m	the magnetic energy density (J/m^3)
r	microchannel radius (mm)
$\mathbf{B_r}$	remanent flux density (T)
V_m	magnetic scalar potential (A)
u, v	x- and y-components of velocity vector (m/s)
P	pressure (Pa)
$\mathbf{F_b}$	body force (N/m^3)
D	diameter (mm)
t	magnet thickness (mm) or time (s)
d	depth (mm)
$\mathbf{V}$	fluid velocity (µm/s)
x	position (mm)
A_c	cross-sectional area (m^2)
h	height (mm)
w	width (mm)
$w(x,y)$	window function
$I(x,y)$	intensity function
$E(x,y)$	the weighted sum of intensity difference multiplied by the window function
K	an empirical constant (─)

L	length (mm)
V	voltage (V)
K_p	proportional gain (—)
K_i	integral gain (—)
K_d	derivative gain (—)

Greek symbols

μ	the viscosity of magnetic nanofluid (Pa.s) or permeability (N/A^2)
χ	magnetic susceptibility (—)
ρ	density (kg/m^3)
φ	volumetric particle concentration (%)
η	non-uniformity factor (—)
λ	the dipolar coupling constant (—)
θ	an arbitrary angular position on microchannel (°)
$\Delta\theta$	the angular interval between magnets (°)
ω	angular velocity (rpm)
β	angular position (°)
ε	error signal (V)
τ	time delay (s)

Abbreviations

MEMS	micro-electro-mechanical systems
vol.	volumetric
wt.	weight
PMMA	poly(methyl methacrylate)
VSM	vibrating sample magnetometer
PMA	permanent magnetic actuator
FF	form factor
CF	crest factor

SMPS	switch-mode power supply
PC	personal computer
PWM	pulse width modulation
ADC	analog to digital converter
HCDA	Harris corner detection algorithm
PID	proportional-integral-derivative
I/O	input/output
ISE	integral square error

Subscripts

r	relative
mnf	magnetic nanofluid
bf	base fluid
p	particle
max	maximum
min	minimum
c	center
t	tangential
n	normal
rms	root mean square
avg	average
m	magnet
c	capillary
f	fluid

APPENDIX 3: Valveless Micropump Assembly

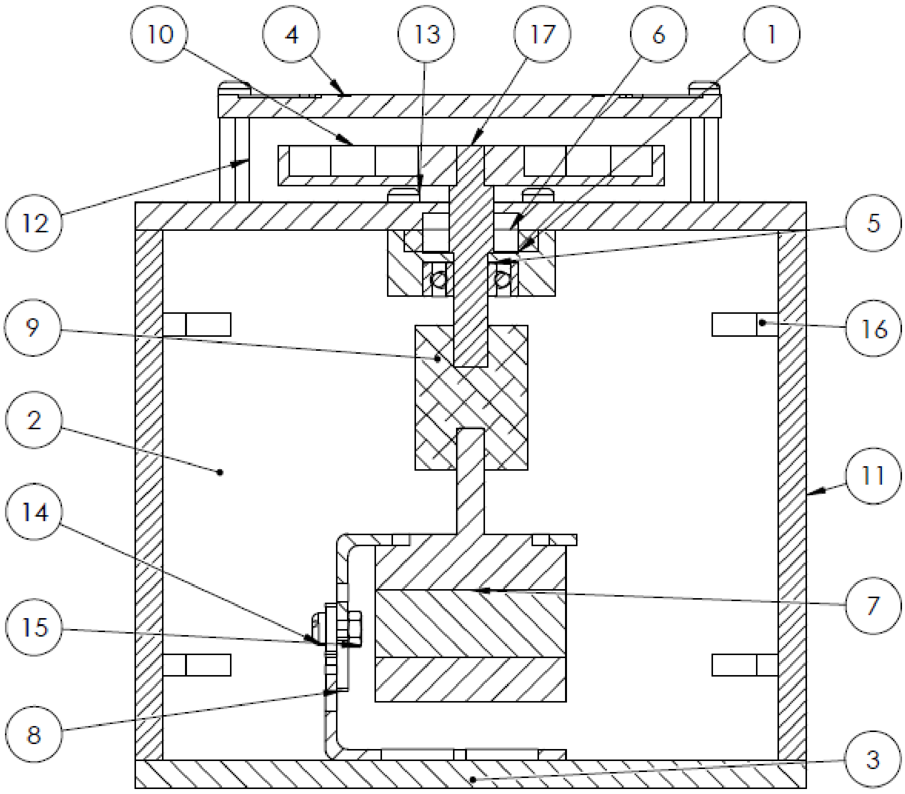

NO.	PART	QTY.
1	Top plate	1
2	Front/Back plate	2
3	Bottom plate	1
4	Microchannel unit	1
5	Ceramic bearing (B606)	2
6	Bearing holder	1
7	Step motor	1
8	Motor holder	2
9	Coupling	1
10	Rotor	1
11	Side plate	2
12	Plastic spacer	4
13	Plastic bolt (M3x10)	8
14	Plastic bolt (M3x6)	2
15	Plastic nut (M3)	2
16	Bracket	4
17	Shaft	1

Valveless Micropump

No. 1 | Scale 1:1

APPENDIX 4: Motor Holder

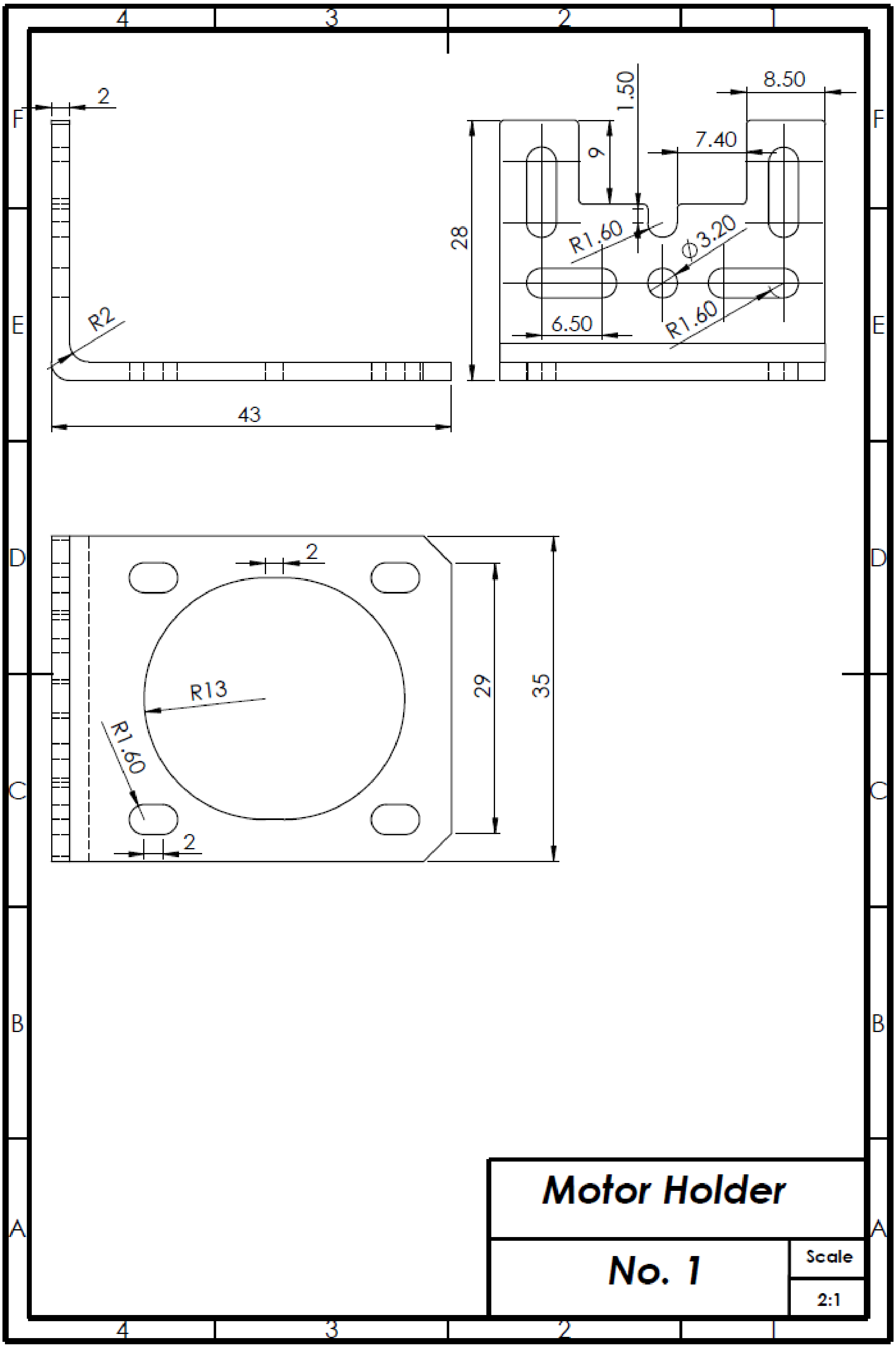

APPENDIX 5: Bearing Holder

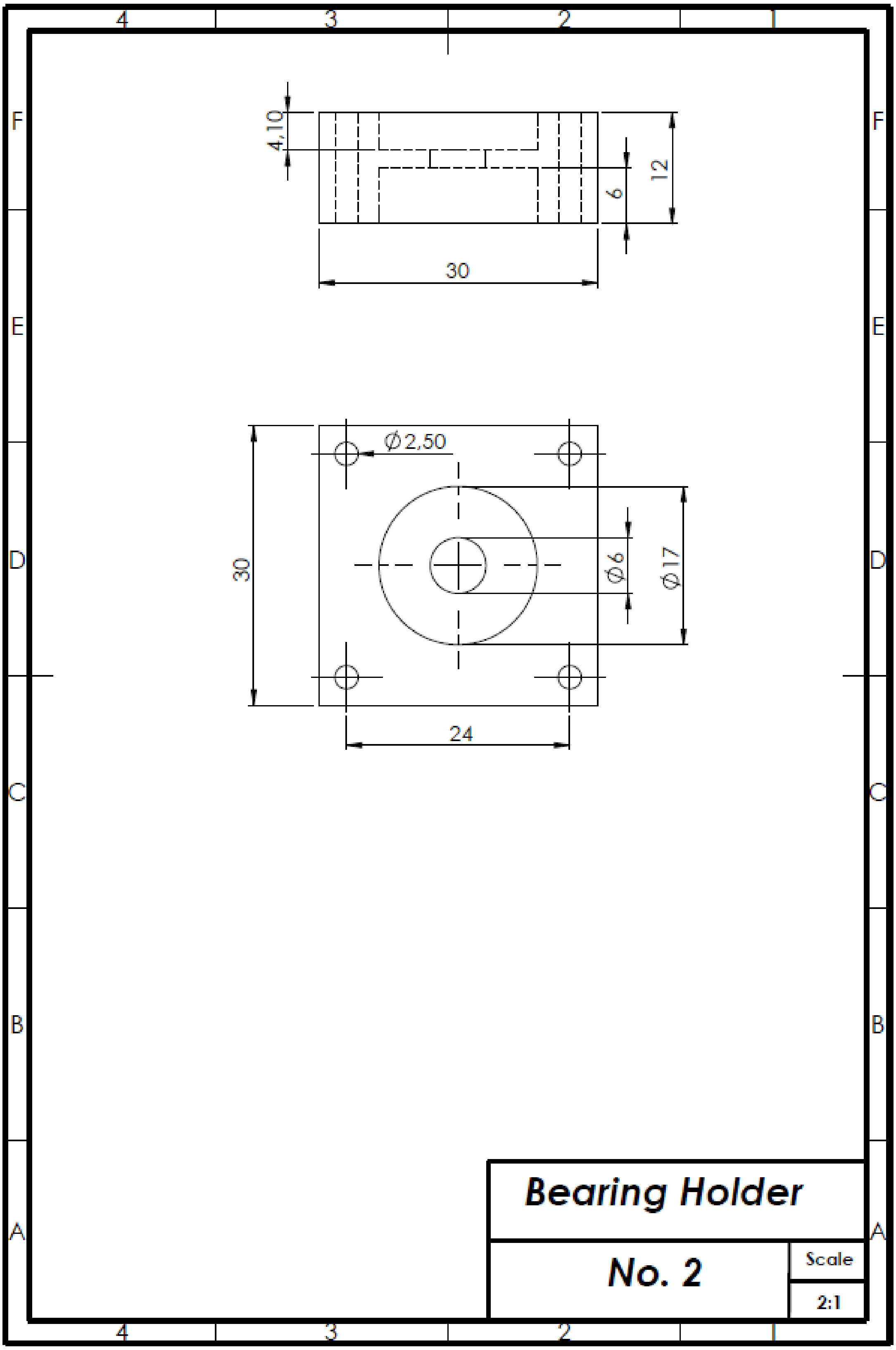

APPENDIX 6: Shaft

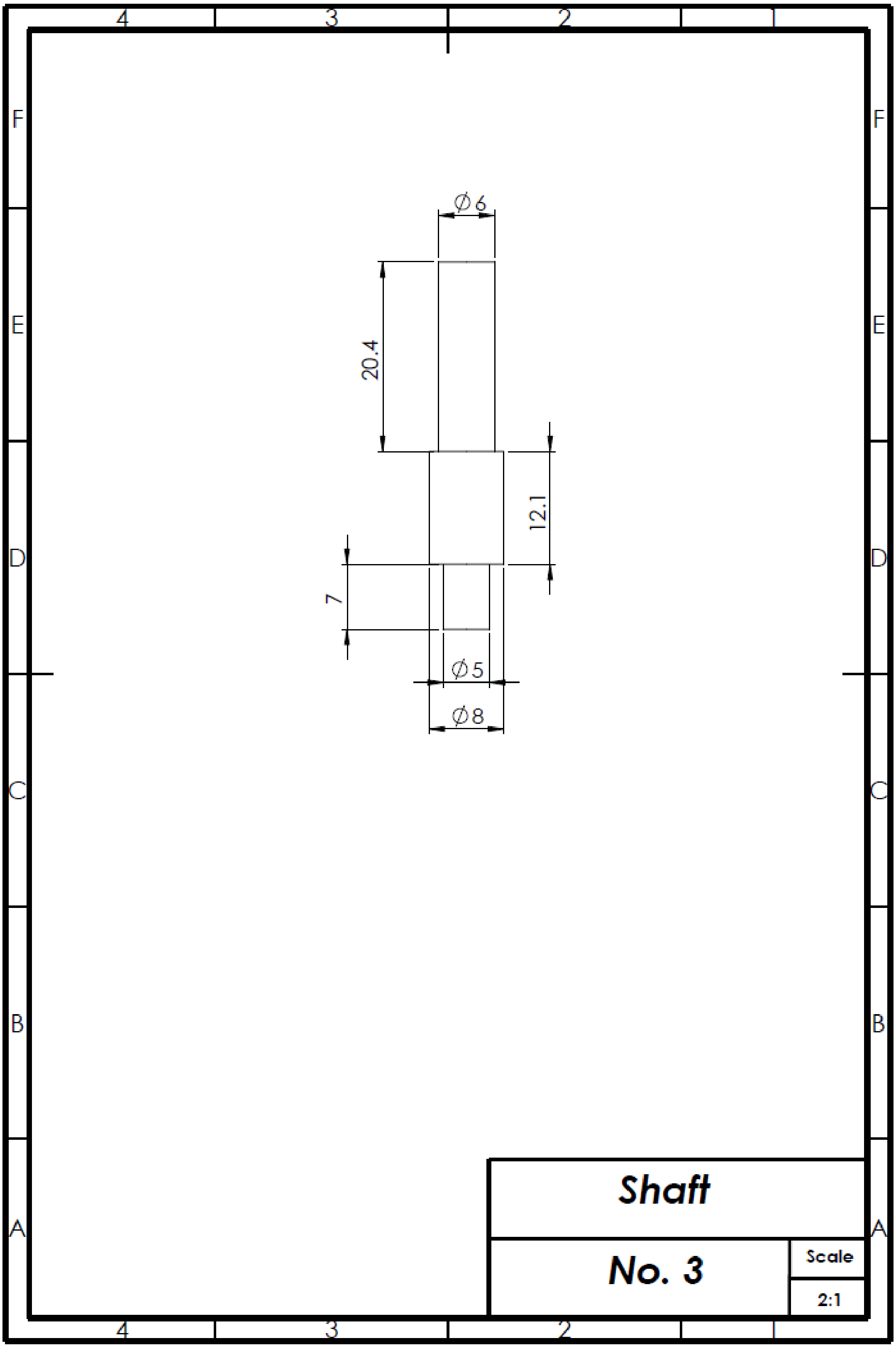

APPENDIX 7: Rotor

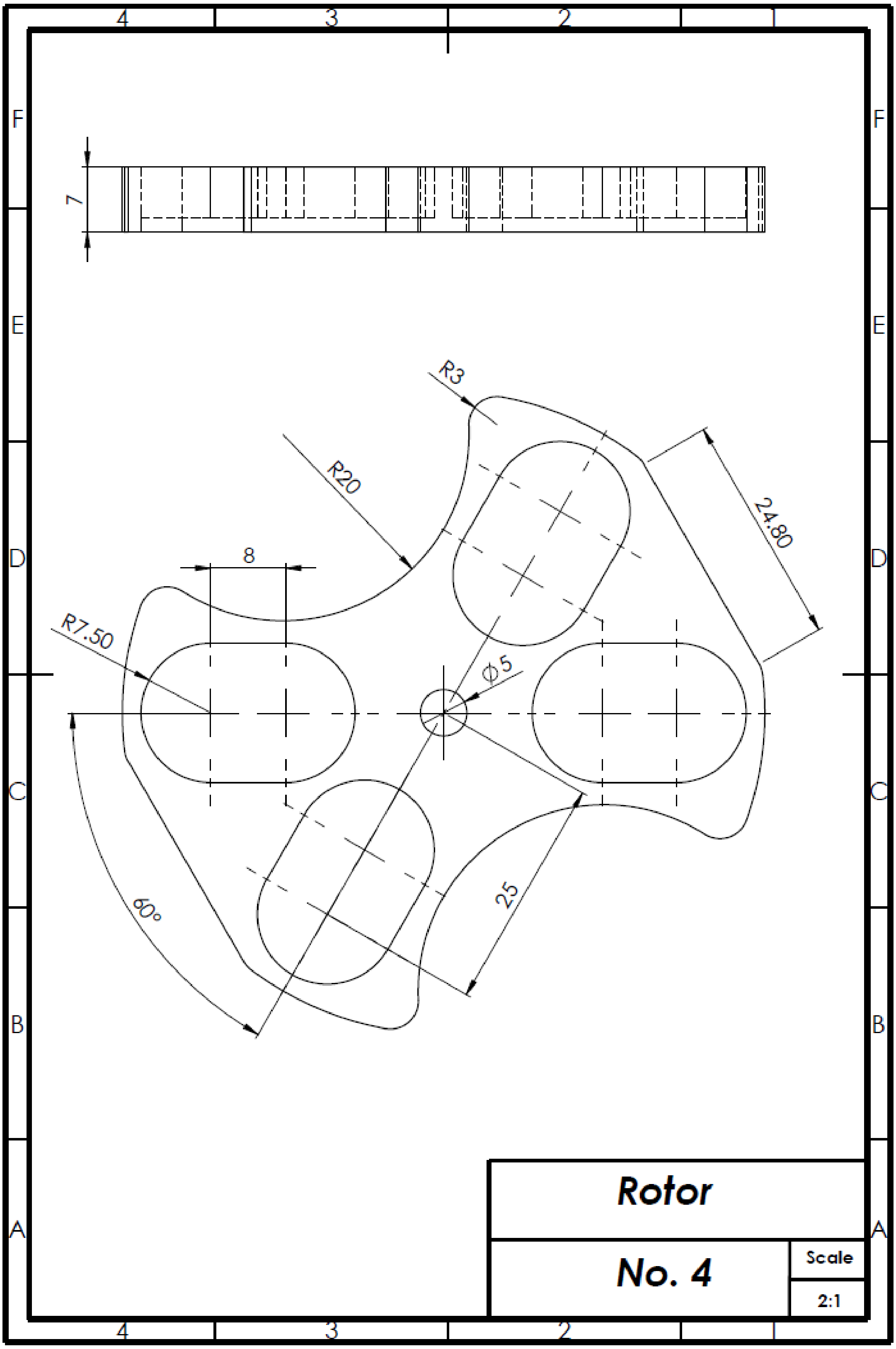

APPENDIX 8: Microchannel Unit